A Heliostat Field Control System

by
Karel Johan Malan

Dissertation presented for the degree of Master of Engineering
in the Faculty of Engineering at
Stellenbosch University

Supervisor: Mr Paul Gauché
Co-supervisor: Mr Johann Treurnicht

April 2014

Declaration

By submitting this thesis electronically, I declare that the entirety of the work contained therein is my own, original work, that I am the owner of the copyright thereof (unless to the extent explicitly otherwise stated) and that I have not previously in its entirety or in part submitted it for obtaining any qualification.

Date: ……………………………

Abstract

The ability of concentrating solar power (CSP) to efficiently store large amounts of energy sets it apart from other renewable energy technologies. However, cost reduction and improved efficiency is required for it to become more economically viable. Significant cost reduction opportunities exist, especially for central receiver system (CRS) technology where the heliostat field makes up 40 to 50 per cent of the total capital expenditure.

CRS plants use heliostats to reflect sunlight onto a central receiver. Heliostats with high tracking accuracy are required to realize high solar concentration ratios. This enables high working temperatures for efficient energy conversion. Tracking errors occur mainly due to heliostat manufacturing-, installation- and alignment tolerances, but high tolerance requirements generally increase cost. A way is therefore needed to improve tracking accuracy without increasing tolerance requirements.

The primary objective of this project is to develop a heliostat field control system within the context of a $5MW_e$ CRS pilot plant. The control system has to govern the tracking movement of all heliostats in the field and minimize errors over time. A geometric model was developed to characterize four deterministic sources of heliostat tracking errors.

A prototype system comprising 18 heliostats was constructed to function as a scaled down subsection of the pilot plant heliostat field and to validate the chosen control method and system architecture. Periodic measurements of individual heliostats' tracking offsets were obtained using a camera and optical calibration target combined with image processing techniques. Mathematical optimization was used to estimate model coefficients to best fit the measured error offsets. Real-time tracking error corrections were performed by each heliostat's local controller unit to compensate for a combination of error sources.

Experimental tracking measurements were performed using the prototype system. Daily open-loop RMS tracking errors below one milliradian were obtained, thereby satisfying the project's primary objective. The thesis concludes that high tracking accuracy can be achieved using the control method proposed here. This could potentially lead to a reduction in heliostat cost, thereby lowering the levelised cost of electricity for CRS plants.

Opsomming

Gekonsentreerde sonkrag se vermoë om groot hoeveelhede energie effektief te stoor onderskei dit van ander hernubare energie tegnologieë. Kostebesparing en hoër effektiwiteit word egter vereis om dit ekonomies meer lewensvatbaar te maak. Beduidende kostebesparingsgeleenthede bestaan wel, spesifiek vir tegnologieë vir sentraal-ontvangerstelsels (*central receiver system* (*CRS*)) waar die heliostaatveld 40 tot 50 persent van die totale kapitaalbestedings uitmaak.

CRS aanlegte gebruik heliostate om sonlig op 'n sentrale ontvanger te reflekteer. Heliostate met 'n hoë volgingsakkuraatheid word vereis om hoë sonkragkonsentrasie-verhoudings te laat realiseer. Dit maak hoë werkstemperature moontlik vir effektiewe energie-omsetting. Volgingsfoute kom hoofsaaklik voor a.g.v. die heliostaat se vervaardigings-, installasie- en instellingstoleransies, maar hoë toleransie-vereistes verhoog gewoonlik die koste. Daar is dus 'n manier nodig om volgingsakkuraatheid te verbeter sonder om die toleransie-vereistes te verhoog.

Die primêre doel van hierdie projek is om 'n heliostaat aanleg kontrole-stelsel te ontwikkel binne die konteks van 'n 5 $\mathrm{MW_e}$ CRS toetsaanleg. Die kontrole-stelsel moet die volgingsbeweging van al die heliostate in die aanleg bestuur en ook met verloop van tyd volgingsfoute verminder. 'n Geometriese model is ontwikkel om die vier bepalende bronne van heliostaat volgingsfoute te karakteriseer.

'n Prototipe stelsel met 18 heliostate is gebou om as 'n funksionele skaalmodel van die toetsaanleg heliostaatveld te dien en om die gekose kontrole-metode en stelsel-argitektuur geldig te verklaar. Periodieke metings van die individuele heliostate se volgingsafwykings is verkry deur 'n kamera en optiese kalibrasie teiken te kombineer met beeldprosesseringstegnieke. Wiskundige optimering is gebruik om die model se koëffisiënte te skat om die beste passing te bepaal vir die gemete foutafwykings. Intydse volgingsfoutregstellings is deur elke heliostaat se plaaslike beheereenheid gedoen om te vergoed vir 'n kombinasie van foutbronne.

Eksperimentele volgingsmetings is uitgevoer met die prototipestelsel. Daaglikse oop-lus RMS volgingsfoute onder een milliradiaan is verkry, en sodoende is die projek se primêre doel behaal. Die tesis maak die gevolgtrekking dat hoë volgingsakkuraatheid behaal kan word deur die gebruik van die beheer-metode soos hier voorgestel. Dit kan potensieel bydra tot kostebesparing in die heliostaatveld van CRS aanlegte om sodoende die geykte koste van elektrisiteit te verminder.

Acknowledgements

I would like to thank the following people and organizations:

Mr Paul Gauché, my supervisor and director of STERG, for his mentorship and academic guidance throughout the course of this project.

Mr Johann Treurnicht, my co-supervisor, for his valuable inputs particularly on communications and control theory.

The Solar Thermal Energy Research Group for an academic base and for funding this work through the following organizations:

- The Stellenbosch University Hope Project
- The South African Department of Science and Technology Solar Spoke Fund
- Sasol Technology

The team at the solar roof laboratory, for their help during the many phases of experimental work.

The majority of diagrams and illustrations in this document were made using *Inkscape*.

Contents

List of Figures

List of Tables

Nomenclature

Constants

Ω_s	Subtending angle of the sun	(9.3 mrad)

Variables

A_{int}	area of interception	[m^2]
A_{a}	collector aperture area	[m^2]
C	image centroid coordinate	[-]
E_{RMS}	root mean square error	[-]
L_{slant}	heliostat slant range	[m]
P	power	[W]
P	intersection point	[-]
P	pixel brightness	[-]
R	image radius	[m]
R_{AP}	ratio of aperture to system nominal power	[-]
R_{I}	intercept ratio	[-]
T	image brightness threshold	[-]
T_{hot} , T_{cold}	temperatures of hot and cold energy reservoirs	[K]
d	image offset distance	[m]
n	noise level scalar	[-]
t_c	control interval	[s]
Δ	heliostat location translation	[m]
Δ_H	heliostat tracking error angle	[rad]
α	elevation angle	[rad]
γ	azimuth angle	[rad]
δ	declination angle	[rad]
ε_{NO}	non-orthogonality angle	[rad]
η	efficiency	[-]
θ_{i}	incident angle	[rad]

θ	relative heliostat to target azimuth angle	[rad]
$\theta_{H,delay}$	heliostat tracking delay angle	[rad]
σ_{slope}	slope error	[rad]
ψ	relative heliostat to target azimuth angle	[rad]
ω	angular velocity	[rad / s]

Vectors and matrices

M	image offset vector
X_8	error parameter vector
$\hat{h}$	heliostat normal unit vector
$\overline{n}$	measurement noise vector
$\hat{s}$	solar unit vector
$\hat{r}$	heliostat-to-target unit vector
$\hat{\imath}$, $\hat{\jmath}$, $\hat{k}$	unit vectors in the zenith-, east-, north directions respectively.

Subscripts

BW	black and white
E	eastward
N	northward
Z	upward
NO	non-orthogonality
e	electric
e	estimated
i	ideal
int	intersection
s	solar

Symbols

%	modulo operator
X	cross product
¢	American cent
§	section

Abbreviations

ASCII	American standard code for information interchange
CAD	computer aided design
CAPEX	capital expenditure
CCD	charge coupled device
CCU	cluster controller unit
CRC	cyclic redundancy code
CRS	central receiver system
CSC	central system controller
CSP	concentrating solar power
DNI	direct normal irradiation
DoE	Department of Energy
EEPROM	electrically erasable programmable read-only memory
EMF	electro-motive force
FFT	fast Fourier transform
GPS	global positioning satellite
GUI	graphical user interface
I/O	input / output
LCOE	levelised cost of electricity
LCU	local controller unit
MEMS	micro-electromechanical system
PC	personal computer
PV	photovoltaic
REIPPP	Renewable Energy Independent Power Producer Procurement
RMS	root mean square
STERG	Solar Thermal Energy Research Group
SUNSPOT	Stellenbosch University Solar Power Thermodynamic Cycle
TDMA	time division multiple access
USART	universal synchronous / asynchronous receiver transmitter
USB	Universal Serial Bus
Bps	bytes per second

bps	bits per second
px	pixels

CHAPTER 1

Introduction

“Renewable energy is the world’s fastest growing form of energy.” (EIA, 2011:11). A global transition from fossil fuels toward renewable energy is underway, driven by a growing awareness of environmental degradation, risk of climate change and the economics of finite fossil resources.

While oil, coal and gas resources are still far from depleted, the costs associated with their use are continually rising. At the same time, global energy demand will likely continue to increase along with growing populations and infrastructure development, especially in the developing world (EIA, 2011). One of the greatest challenges of our time is to find efficient and cost effective ways to harness alternative forms of energy.

Nuclear power could play a significant role in the medium term during the transition to renewable energy. However, cost uncertainty and challenges associated with waste management and arms proliferation may count heavily against it. Photovoltaics (PV) and wind power are already cost competitive with coal and gas in some instances and can help to reduce the use of conventional fuels. Unfortunately, the intermittent nature of PV and wind coupled with our inability to store electrical energy at a significant scale make these technologies unsuitable for baseload- or peaking power applications.

Concentrating solar power (CSP) converts sunlight into thermal energy which can be used in industrial processes or for generating electricity. Unlike electricity, thermal energy can be stored cheaply and efficiently even at utility scale. This sets CSP apart from other renewable energy technologies, enabling it to provide dispatchable power in sunny parts of the world (IEA, 2010:7). CSP has been identified as a potential long term solution for South Africa due to the country’s excellent solar resource and the technology’s potential for dispatchability and job creation (Gauche *et al.,* 2012; Brand *et al.*, 2012).

This chapter starts off giving a background for solar energy and shows how CSP fits into this category. The project’s objectives, methodology and scope are then discussed before ending with an overview of the rest of the document.

1.1. Solar Energy

This section classifies solar energy harvesting methods and discusses general CSP concepts before moving the focus to central receiver systems (CRS).

1.1.1. The Sun as Energy Source

Over 99.9 per cent of Earth's energy comes from the sun (De Rosa, 2005). In addition to sunlight reaching the earth's surface, the sun is the source of all wind-, hydro-, and wave energy as well as biomass and fossil fuels - which originated from organic matter and represents stored solar energy collected by photosynthesis over many millions of years.

Enough direct sunlight reaches the earth to supply all of humankind's energy needs many times over. For example, the yearly direct normal irradiation (DNI) component of solar energy from just the Northern Cape Province of South Africa is equivalent to more than six times the worldwide annual energy consumption.[1] However, the dilute nature of sunlight reaching the earth makes it relatively difficult to capture and convert into usable power.

1.1.2. Harvesting Solar Energy

There are two methods commonly used to harvest solar energy for electricity. PV cells use semiconductors to directly convert light into electricity whereas solar thermal systems convert sunlight into thermal energy to generate electricity by means of a heat engine in much the same way as conventional power plants do.

CSP makes use of focusing optics and solar tracking mechanisms to concentrate sunlight for producing high temperature thermal energy. The following terms will be used throughout this document to refer to the various parts of a CSP system (Duffie & Beckman, 1980:331):

- The **concentrator** is a system of optical elements (usually mirrors) that produces concentrated solar energy by directing incident sunlight from a large area onto a smaller receiver area.
- The **aperture** of the concentrator is the cross sectional area through which sunlight enters the system.
- The **receiver** absorbs and converts the concentrated sunlight into thermal energy.
- The **collector** refers to the entire energy collection system and includes the receiver and the concentrator.

Figure 1.1 shows a classification diagram of solar power in which a distinction is made between PV and solar thermal systems and then again between concentrating and non-concentrating systems.

---

[1] Northern Cape land area is 372 889 km^2 and average annual DNI >2500 kWh/m^2 (Cebecauer *et al.*, 2011), so annual DNI of the province is >3356 EJ. Global annual energy consumption in 2012 was 535 EJ (EIA, 2011).

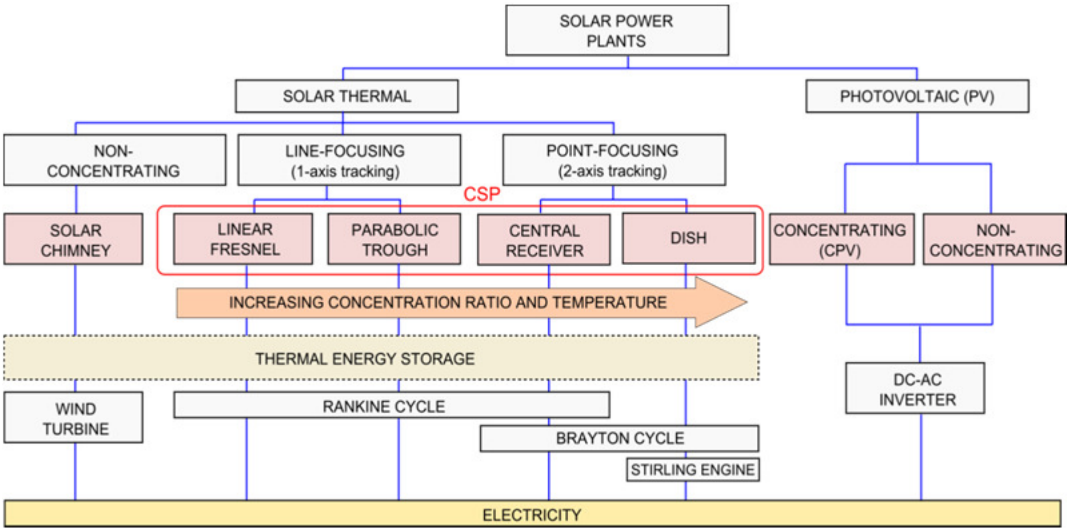

Figure 1.1: Classification of solar power and types of CSP. (Adapted from Konstantin & Kretschmann, 2010).

CSP falls under solar thermal systems and can be classified by concentrator type. In order of increasing concentration ratios, Linear Fresnel- and Parabolic Troughs focus energy in a line (Figure 1.2) whereas CRS and Parabolic Dish concentrators focus energy to a point (Figure 1.3). Line-focus systems need to track the sun in one axis while point-focus systems need dual-axis tracking.

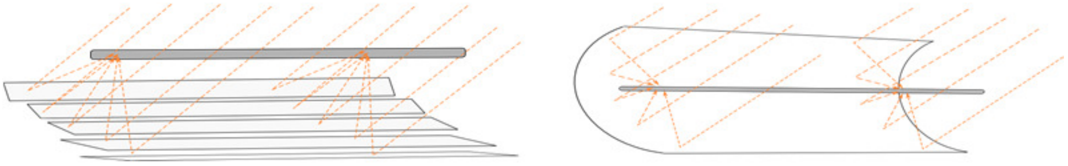

Figure 1.2: Line-focus concentrators: Linear Fresnel (left) and Parabolic Trough (right).

Figure 1.3: Point-focus concentrators: Central Receiver (left) and Parabolic Dish (right).

The efficiency with which thermal energy can be converted to work (and ultimately electricity) has a theoretical upper limit (η_{lim}), expressed by Carnot's theorem:

$$\eta_{\text{lim}} = 1 - \frac{T_{cold}}{T_{hot}} \qquad (1.1)$$

This theoretical efficiency limit clearly depends on the temperature difference between the hot source (T_{hot}) and the cold reservoir (T_{cold}) of the conversion system. It is therefore desirable to employ high solar concentration ratios to obtain the high operating temperatures needed for efficient energy conversion. As a general rule, the required tracking accuracy is proportional to the system's concentration ratio and so it becomes critical in CRS- and parabolic dish applications.

1.1.3. Challenges and Opportunities for CSP

One of the biggest barriers to large scale CSP deployment is its high initial cost compared to that of conventional power plants. However, CRS technology is still relatively immature, so it is widely considered to present the best opportunity for cost reduction (in utility scale deployment) of all CSP types (Kolb *et al.*, 2011).

The SunShot Initiative, launched in 2011, is a funding program by the United States Department of Energy (US DoE) which aims to reduce the levelised cost of electricity[2] (IRENA, 2012) of CSP from its 2011 level of 15¢/kWh to under 6¢/kWh by 2020 (US DoE, 2011a). Specific technology improvement opportunities (TIO) were identified to reduce the cost of the heliostat field, which typically makes up 40-50 per cent of a CRS plant's total cost (Ortega *et al.*, 2008; Kolb *et al.*, 2007). These TIO's range from optimization of heliostat structures and drivetrains to improvements in tracking accuracy and communication networks, including:

- "Reliable wireless methods for heliostat power and communication.
- Advanced, self-aligning control systems." (Kolb *et al.,* 2011:33).

Looking closer to home, significant job opportunities exist in South Africa with the development of a local CSP industry to build future domestic plants and eventually to export to the international market. At the time of writing, 200 MW_e of CSP projects have already been awarded to major international players Abengoa and ACWA Power International under the Renewable Energy Independent Power Producer Procurement (REIPPP) program (CSP World, [S.a.]). Significant opportunities exist for CSP developers in the domestic market due to steadily rising local content requirements in future REIPPP bidding rounds (DTI, 2012).

1.1.4. Central Receiver Concept of Operation

The Central Receiver configuration's concentrator consists of a large array of heliostats (tracking mirrors), as per figure 1.4. Each heliostat periodically adjusts its orientation in two axes to compensate for the earth's movement relative to the sun, thereby continuously directing incident sunlight onto a centrally located tower-mounted receiver. The receiver absorbs the concentrated sunlight and converts it to thermal energy which is carried away by a heat transfer medium (typically steam or molten salt) to drive a turbine or to be stored for later use.

---

[2] The average cost per unit of electricity produced over the entire lifetime of a power plant.

Figure 1.4: The heliostat field of a Central Receiver CSP plant. (Source: Wimberley, 2011).

1.1.5. The SUNSPOT Cycle

This project forms part of ongoing research by the Solar Thermal Energy Research Group (STERG) at Stellenbosch University towards a locally developed commercially feasible solar thermal power plant. The SUNSPOT concept (Stellenbosch University Solar Power Thermodynamic Cycle) was proposed by Kröger (2012) as a suitable thermodynamic cycle for generating electricity from solar energy in South Africa (Figure 1.5).

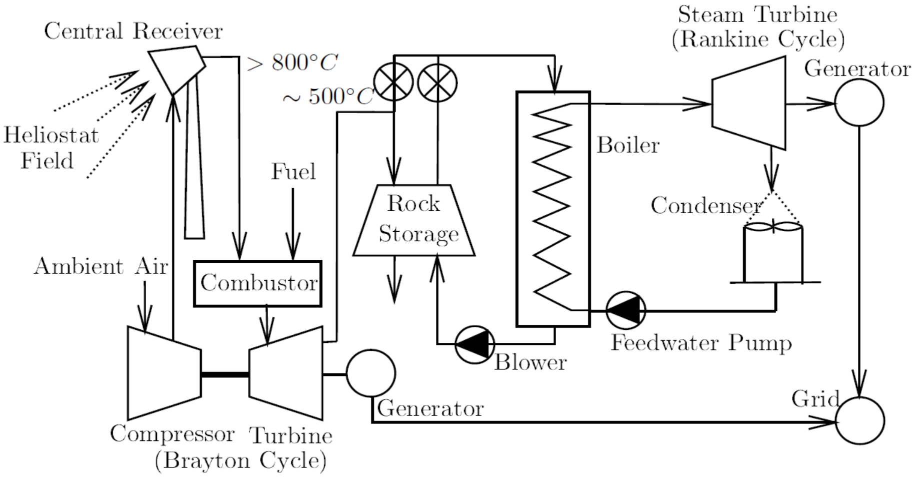

Figure 1.5: The SUNSPOT cycle concept. (Source: Landman, 2013)

The SUNSPOT concept uses a central receiver configuration to collect and convert sunlight into high quality thermal energy. The high temperature (>800 °C) primary cycle heats up compressed air to drive a gas turbine (Brayton cycle). The concept also allows for hybridization with another fuel source and storage of excess energy as sensible heat in a rock bed storage system. A lower temperature (~500 °C) secondary loop could use the stored energy to drive a Rankine cycle.

1.2. Objectives

This project's primary objective is to develop the method and high level architecture for a heliostat array control system within the context of a 5 MW_e SUNSPOT pilot plant. The control system has to govern the real-time tracking of the entire array, each heliostat compensating for the relative Earth-Sun movement to maximize the reflection of sunlight onto a stationary receiver. The control system should:

a. Propose a solar tracking method combined with a strategy for correcting heliostat tracking errors.
b. Have an operator interface for manual override control and status monitoring.
c. Be able to respond to emergency situations by defocusing solar flux from the receiver and/or move all heliostats to their stow positions within a specified time.

Additionally, a prototype heliostat array should be constructed to function as a scaled-down subsection of the proposed 5 MW_e pilot plant array. The prototype system should:

a. Validate the chosen tracking- and error correction methods experimentally, showing 'learning' ability by minimizing tracking errors over time. Since this was the first attempt at heliostat control in STERG, the tracking accuracy goal for this system was set at one milliradian root mean square (RMS) (Freedman *et al.*, 2007:66) tracking error calculated over one full day.
b. Validate the high level system architecture and demonstrate system scalability in terms of communication- and processing functionality.
c. Demonstrate an initial target approach and emergency stow strategy.

1.3. Methodology

Following from the objective, the overall research methodology is summarized as:

a. Investigate relevant literature to understand previous work done in the field.
b. Set appropriate requirements and derive high level specifications.
c. Design and model a suitable control method for the proposed 5 MW_e pilot.
d. Construct a prototype system to act as a scaled-down subsection of the proposed pilot plant.
e. Plan and perform tests to measure tracking accuracy and evaluate system functionality.

1.4. Scope and Limitations

This project represents a first study in heliostat field control in STERG. Since no heliostat hardware or software existed previously, a range of disciplines had to be covered. These included:

- High level control system design
- Network architecture and protocol development
- Mechanical design of heliostats and mounting structures
- Geometric modelling and mathematical optimization
- Image processing
- Programming of embedded processors
- Software development across multiple platforms.

The project's focus is limited to heliostat field control and excludes all work associated with the receiver or power block. While considerable effort was made to design appropriate heliostat mechanisms for the prototype system, mechanical and structural optimization was consciously limited.

1.5. Document Outline

Chapter 2 contains a literature study of existing research in the fields of solar tracking, heliostat tracking, control methods, error correction and central receiver development trends before concluding with an overview of the current state of the art in heliostat array control.

Chapter 3 develops the heliostat field control architecture for a proposed 5 MW_e CRS pilot plant, starting with system requirements. High level specifications are derived in a top down manner to meet the objectives of high tracking accuracy as well as system scalability and modularity.

Chapter 4 derives the heliostat error propagation model which is used to predict future tracking errors from past measurements, allowing for real-time error correction as part of the control strategy developed in Chapter 3.

Chapter 5 describes the detailed prototype implementation, including heliostat mechanisms, mounting structures, electronic hardware, software procedures and data processing flow diagrams.

Chapter 6 presents and discusses experimental results before Chapter 7 concludes on the thesis outcome and makes recommendations for future work.

CHAPTER 2

Literature Review

This chapter reviews work from literature relevant to the control of heliostats in central receiver systems (CRS). The fundamentals of earth-sun geometry are discussed and solar angles are defined. The focus then shifts to: solar tracking; heliostat tracking and error correction; CRS development trends and the current state of the art in heliostat field control systems.

2.1. The Solar Vector

The ability to accurately track the sun is a fundamental requirement of CSP systems. Solar tracking is also applicable to the photovoltaic (PV) industry, since two-axis tracking can increase power production by up to 30 per cent over stationary panels (Truchero, Andreu & Garcia, 2010). A large number of solar tracking methods exist today.

2.1.1. Earth-Sun Geometry

The earth travels around the sun in an off-centre elliptical orbit contained in the ecliptic plane (Figure 2.1). The mean earth–sun distance is roughly 150 million km and is conventionally referred to as one astronomical unit (au) (IAU, [S.a.]). The earth rotates approximately 365 ¼ times around its polar axis in the time it takes to complete one orbit around the sun. Earth's polar axis has a mean tilt angle of 23.45° relative to the ecliptic plane and maintains a constant alignment relative to the stars, except for the slow effects of axial procession and nutation[3] (Nutation, [S.a.]).

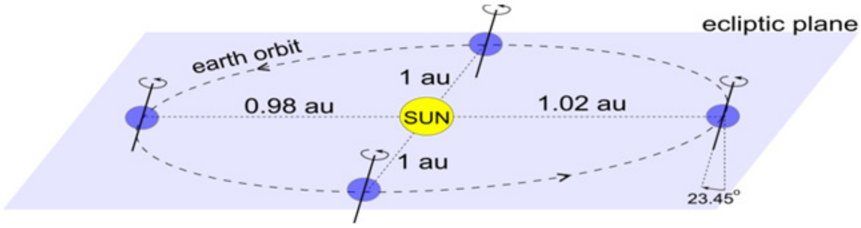

Figure 2.1: The earth's orbit around the sun (adapted from Stine & Geyer, 2001).

---

[3] Axial procession is the clockwise rotation of the polar axis orientation (when viewed from above the ecliptic plane), with a period of approximately 26 000 years. Nutation is a sinusoidal perturbation in the polar axis orientation. Nutation has an amplitude of 9.2 arc seconds and a period of 18.6 years.

The declination angle (δ) is the angle between the equatorial plane (which is perpendicular to the polar axis) and an imaginary line drawn between the centre of the earth and the centre of the sun. The earth's orbit around the sun, combined with its near constant polar axis tilt causes an annual 23.45° sinusoidal oscillation of δ. This causes the seasonal variation in daylight period and apparent sun path at any fixed location on earth. Seasonal variation becomes more pronounced as the observer moves away from the equator toward the poles. A stereographic plot of the annual sun path for Cape Town is shown in Figure 2.2. The radial and angular axes represent the daily and yearly variation in solar zenith- and azimuth angles respectively, as seen by an earthly observer.

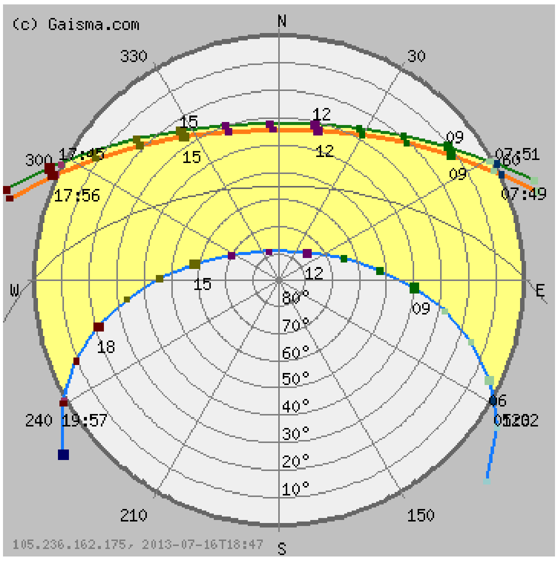

Figure 2.2: A stereographic plot of Cape Town's annual sun path (Tukiainen, 2013).

A more detailed discussion of earth-sun geometry, including a step by step derivation of the solar vector can be found in Stine and Geyer (2001:§3). Grena (2007) introduces multiple correction factors for improved accuracy. Meeus (1998) provides in depth coverage of several astronomical algorithms and is the basis for the highly accurate Solar Position Algorithm (SPA) used by the United States National Renewable Energy Laboratory (NREL) (Reda & Andreas, 2008).

2.1.2. Solar Tracking

Clifford and Eastwood (2004) discuss a range of commercial solar trackers and distinguishes between actively powered- and passively powered actuation. The former category includes trackers with electric motors and hydraulics which require an external power source. The latter includes devices that work with kinetic potential energy (springs or weights) or by thermal expansion of materials being heated by the sun (*How Trackers Work.* [S.a.]). Tracking mechanisms can also be classified according to open- versus closed-loop control, as per Lee *et al.* (2009). Table 2.1 shows examples of tracking mechanisms according to actuation- and feedback type.

Table 2.1: Classification and examples of solar tracking mechanisms

	Passively powered mechanisms	Actively powered mechanisms
Open-loop tracking	Clockwork mechanisms	Microprocessor-based solar algorithms
Closed-loop tracking	Trackers using thermal expansion actuators	Electro-optical feedback sensors

Rubio *et al.* (2007) categorizes solar tracking methods by their respective control mechanisms as follows:

- Passive tracking (using self-powered actuators)
- Active tracking with electro-optical sensor feedback
- Microprocessors running solar algorithms.

Passive solar trackers

Open-loop passive trackers typically make use of clockwork mechanisms and do not need sunlight to work (Abdulrahim *et al.*, 2011) whereas closed-loop passive systems use sunlight to provide the required feedback energy. For the latter a pair of opposing solar powered actuators are typically positioned to receive equal solar radiation only when the tracking device points directly at the sun. Misalignment with the solar vector causes a negative feedback force which serves to continuously track the sun (Clifford & Eastwood, 2004).

Electro-optical sensor feedback tracking

These systems rely on sunlight falling on light sensors to provide alignment error feedback signals to a closed-loop electronic control system (Mousazadeh *et al.,* 2009). The control system regulates power supplied to motors or hydraulics that act to re-align the system toward the solar vector. Figure 2.3 shows three types of electro-optical feedback devices.

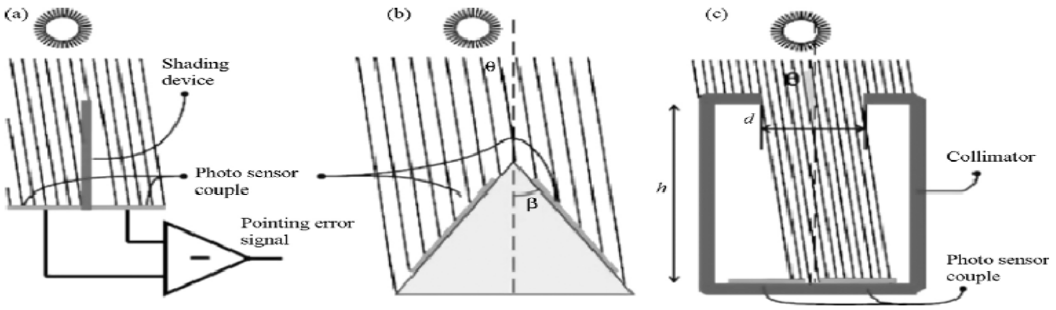

Figure 2.3 a,b,c: Three examples of electro-optical feedback sensors (Mousazadeh *et al.*, 2009)

With reference to Figure 2.3: (a) shows a simple shading device with light sensors (typically photodiodes) on either side to provide input signals to a differential amplifier; (b) shows solar panels mounted in such a way as to receive differential solar radiation based on their alignment to the sun. In (c), a collimator structure is used to allow only a narrow beam of sunlight to fall onto a more sophisticated light sensor. Typically, a charge-coupled device, similar in function to a digital camera's image sensor, can be used to provide an accurate solar position feedback signal.

Solar Position Algorithms

Blanco-Muriel *et al.* (2000) reviews a number of early solar algorithms by Cooper (1969), Spencer (1971), Swift (1976) and Lamm (1981). These algorithms estimate the sun's declination angle and various equations for solar time for a full day at a time. These early algorithms yield solar angle uncertainties in the range of several tenths of degrees. More sophisticated algorithms by Pitman & Vant-Hull (1979), Walraven (1979) and Michalsky (1988) use observer position and time to produce solar angle uncertainties in the range of hundredths of degrees.

The Plataforma Solar de Almería (PSA) algorithm later added higher order polynomial coefficient terms and parallax correction to the earlier Nautical Almanac equations used by Michalsky (1998). Angular uncertainty was reduced to under a hundredth of a degree (Blanco-Muriel *et al.,* 2000).

More recently, Grena (2007) developed an algorithm based on that of Michalsky (1988) and added several correction factors, notably atmospheric refraction correction for the solar elevation angle. This algorithm has a maximum uncertainty of 0.0027 degrees and was designed for computational efficiency. The Solar Position Algorithm (SPA) by Reda and Andreas (2008) is by far the most accurate to date. It has a maximum tracking uncertainty of 0.0003 degrees from 2000 BC to 6000 AD and is based on algorithms published by Meeus (1998). Table 2.2 lists five solar position algorithms by author(s), year of publication and maximum tracking uncertainty in ascending order of accuracy (Lee *et al.*, 2009; Blanc & Wald, 2011).

Table 2.2: Five solar position algorithms by author, year and accuracy.

Author(s)	Year	Tracking Uncertainty [degree / mrad]
McFee	1975	0.5 / 8.73
Michalsky	1988	0.01 / 0.175
Blanco-Muriel *et al.* (PSA)	2001	0.008 / 0.14
Grena	2008	0.0027 / 0.047
Reda & Andreas (SPA)	2008	0.0003 / 0.005

2.2. Heliostat Tracking and Error Correction

This section reviews heliostat control methods described in the literature. A number of these methods are combined to form state of the art control strategies of modern commercial CRS plants, as will be discussed in §2.4.

2.2.1. Closed Loop Tracking with Real-Time Error Feedback

Local Feedback

Roos *et al.* (2007) describes controlling a 25 m^2 target aligned heliostat with local feedback obtained from an electro-optical sun tracking sensor similar to that shown in Figure 2.3a. Since the heliostat normal angle needs to always bisect the sun-to-heliostat-to-receiver angle, the sensor was connected to the heliostat's primary axes via a 2:1 mechanical reduction. Experimental results yielded a daily mean normal vector tracking accuracy of 3.3 mrad.

Quero *et al.* (2007) proposes a method for providing local error feedback to each heliostat by measuring its reflected beam angle. Electro-optical sensors, each having a collimator structure of the type described in §2.1.2 is placed between each heliostat and the receiver. Misalignment of the error reflected image results in a corresponding beam angle deviation measured by the sensor. This scheme requires very accurate alignment during installation, but can also be periodically calibrated using an electronic offset procedure.

In a patent application by Pfahl, Buck & Rehschuh (2009), a local feedback tracking method is proposed which measures the relative angles between the heliostat normal, the receiver and the sun by using an imaging device mounted on the heliostat. A small hole in the mirror surface allows an image to form on a plane behind the hole, similar to how a camera works. An image sensor measures the centre-offsets of the images made by the receiver and the sun. This provides simultaneous angle feedback of the sun and the receiver relative to the heliostat normal vector. The feedback allows for continuous adjustment of the heliostat until its normal vector bisects the angle between the sun and the receiver.

Receiver Feedback

A patent application by Yogev & Krupin (1999) describes a scheme for directly measuring individual heliostat aiming errors by 'looking back' from the receiver to the field. A set of four cameras is positioned at opposite ends of the receiver aperture (above, below, left and right). The operating principle is that misaligned heliostats appear unequally bright to cameras located at opposing ends of the receiver. For example, if a heliostat aims at the top-left corner of the receiver, it will appear brighter to the camera located above the receiver than to the camera below. The same goes for left vs. right. During each control period, a set of cameras are commanded to simultaneously take a picture of the same field section. Control signals for multiple heliostats can then be calculated by comparing the relative brightness values of image sections that correspond to specific heliostats in the field.

(Kribus *et al.*, 2004) builds on abovementioned principle and presents a detailed correction methodology with test results showing individual heliostat tracking errors reduced to 0.1 - 0.3 mrad. A company called Thermata further developed a closed-loop optical tracking system which uses this concept (US DoE, 2012b). However, the fact that this method has so far not seen widespread use is an indication of the image processing challenges and practical difficulties associated with operating cameras close to a high flux receiver.

Convery (2010, 2011) describes a novel method for identifying individual heliostat reflections from among many others in a field. Piezoelectric actuators are attached directly to heliostat mirror surfaces to induce specific vibration signatures. These mechanical vibrations, typically in the audio frequency range of 1 – 30 kHz, modulate the reflected sunbeam at the same frequency. Photodiodes located around the receiver aperture transduce the modulated beams and digital signal processing is used to distinguish between spatially superimposed heliostat images by means of Fast Fourier Transform (FFT) methods.

2.2.2. Model Based Open Loop Tracking with Delayed Error Feedback

By definition, open loop tracking uses no real-time error feedback. The required heliostat normal vector is calculated at regular intervals along with actuator control signals to keep realigning the heliostat.

Baheti & Scott (1980) derived a basic movement model to account for a heliostat's pedestal tilt, azimuth- and elevation axes bias and drive wheel radius tolerance. It was argued that fabrication tolerances (for orthogonal axes alignment) and rotary encoder alignment could be easily controlled, so these sources were not included in the model. A closed-loop solar tracking sensor was used to periodically point the heliostat normal vector directly at the sun. Heliostat pointing errors were then obtained at each measurement interval by comparing the commanded heliostat position with the 'real' solar position as calculated by a solar algorithm. This data was used to estimate coefficients for the error model and resulted in final RMS error reductions of 10 : 1 and 5 : 1 for azimuth- and elevation tracking respectively. This and other model-based methods were not widely implemented at the time due to the high cost and practical constraints (size, weight, non-portability) of computers at the time.

A more refined heliostat movement model was patented in 1986 by McDonnell Douglas[4] as part of what the inventor called "An automatic heliostat track alignment method" (Stone, 1986). This model included error sources previously described by Baheti & Scott and added a rotation element caused by non-orthogonality of a heliostat's principle axes. The effect of gravity sag was later added when a generalized model was published which could also be applied to dish Stirling engines (Stone & Kiefer, 1998). This method has since been widely cited in academic work and can be

---

[4] McDonnell Douglas merged with Boeing to form The Boeing Company in 1997.

considered the basis for model based open-loop heliostat error correction since (Camacho *et al.*, 2012; Berenguel *et al.,* 2004).

Stone & Jones (1999) reports that during operation of Solar One[5], correction of misaligned heliostat azimuth axes were attempted by manually adjusting their pedestal mounting bolts with the aid of "a very accurate electronic inclinometer". This was expensive and proved to be ineffective in reducing long term tracking errors. Later, a heliostat beam characterization system (BCS), analogous to a modern digital camera, was used to capture reflected solar images on a calibration target located on the tower below the receiver (Blackmon *et al.*, 1986; Strachan, 1993). Elevation- and azimuth-axis offsets (bias adjustments) were calculated based on three reflected beam measurements per day. This replaced the need for structural adjustments, but was still time consuming and in some cases actually exacerbated long term tracking errors because such offsets introduce time-varying beam errors of their own (Stone & Lopez, 1995).

Solar Two[6] continued using the bias adjustment strategy, but used a BCS to obtain more measurement points per day and implemented the required offset corrections in software (Stone & Sutherland, 1997). Various strategies using different measurement schedules are analysed in Jones & Stone (1999). It was concluded that future CRS plants would perform better if a model-based method, like what is described in Stone (1986) and Stone & Kiefer (1998), was used instead.

A machine vision system for automatically determining heliostat beam error offsets is described by Berenguel *et al.* (2004) and Camacho *et al.* (2012:261). The strategy is based on the BCS system used at Solar One/Two as described by Blackmon *et al.* (1986). A modern digital camera is used for image acquisition and digital image processing techniques for calculating the reflected beam centroid relative to the intended aim point are presented. The procedure is automated to save time and to avoid the need for a human operator.

2.3. Central Receiver Development: History and Trends

The Arab Oil Embargo of 1973-74 highlighted US dependence on oil imports and led to various funding programs for renewable energy technologies from the late 1970s to the early '80s (Gallego *et al.,* 2012). Solar One, a 10 MW_e CRS plant, was constructed in California in 1981 to prove the technology's viability at utility scale (Kolb, 1985). It was later converted to Solar Two which operated from 1998 to 1999 and demonstrated thermal storage using molten salt (Jones *et al.,* 1999). By this time,

---

[5] A 10 MW_e CRS plant which used 1818 heliostats and operated from 1980 to 1988 in California.

[6] Solar One was converted to Solar Two in 1995 to demonstrate thermal storage.

steadily falling oil prices and policy shifts away from renewable energy led to a long period of stagnation for CSP development in the US (Gallego *et al.,* 2012).

Spain introduced attractive feed-in tariffs for CSP in 2004 which led to the first ever commercial CRS plants, PS10 and PS20, to be completed in 2007 and 2009 respectively (Lovegrove & Stein, 2012:255). Gemasolar followed in 2011 and became the world's first CRS plant with the ability to deliver full power output for 24 hours a day due to its high solar multiple[7] and 15 hour thermal storage capacity (Lata *et al.,* 2011). The recent economic downturn in Europe led to cuts in feed-in tariffs which caused the Spanish CSP industry to put all new projects on hold (Alcauza, 2013).

Meanwhile, recent favourable solar energy policies in the US have led to the construction of several new CRS plants: eSolar's Sierra SunTower in 2009 (Sherif, 2010); Brightsource's Coalinga in 2011 (Coalinga [S.a.]) and Ivanpah in 2013 (NREL [S.a.]b); SolarReserve's Crescent Dunes due to be commissioned in early 2014 (Crescent Dunes, [S.a.]).

CSP development roadmaps and cost reduction studies published in the last decade show that the heliostat field remains by far the most expensive part of a CRS plant. Three sources estimate its share of a typical large plant's total capital expenditure (CAPEX) at 40 %, 45 % and 50 % respectively (Ortega *et al.*, 2008; Sargent & Lundy, 2003; Kolb *et al.,* 2011). The optimal size for heliostats remains uncertain, with current commercially deployed units ranging all the way from 1.16 to 120 m^2 (NREL, 2012). A recent study by Sandia Laboratories involving members from industry gives a comparative breakdown of heliostat component costs for small and large heliostats (Kolb *et al.,* 2011).

When expressed as a percentage of the total cost-per-m^2, smaller heliostats suffer from markedly more expensive control- and wiring components since more control units are needed and the unit costs are largely unaffected by heliostat size. Small heliostats also have higher relative drivetrain costs, but since larger heliostats do require more expensive drivetrains, this effect is less pronounced. Conversely, the relative cost-per-m^2 of structural components (foundations, pedestals and mirror support structures) is higher for larger heliostats since wind loads increase exponentially relative to mirror area (Kolb *et al.,* 2011:4; Peterka & Derickson, 1992).

A transition toward heliostats with more autonomous local control, wireless communication and PV powered drives is already underway, driven by decreasing costs of electronic control components (Kolb, 2011:58) and increasing capabilities of wireless technologies (Camacho *et al.,* 2012:248; Bobinecz, 2012; Kubisch *et al.,* 2011). The cost reduction afforded by these improvements benefit smaller heliostats more than it does large heliostats. Also, since the cost of steel and concrete is

---

[7] A plant's solar multiple is defined as the ratio of the actual concentrator aperture to the aperture required to power the turbine at its full capacity under ideal irradiation conditions.

significantly impacted by that of primary energy (Rademaekers *et al.*, 2011) rising energy prices penalize larger heliostats more severely. It therefore seems plausible that heliostats will evolve toward the smaller end of the spectrum in future. Brightsource's 380 MW_e Ivanpah[8] plant which uses relatively small 15 m^2 heliostats may be an early indicator of such a trend.

2.4. State of the Art Tracking and Calibration Methods

Since these methods form an integral part of commercial central receiver developers' proprietary knowledge, limited information is publicly available on the tracking and calibration methods of major industry players. According to Camacho *et al.* (2012), open loop heliostat tracking by means solar position algorithms is the current industry norm. This may change in future if the SunShot Initiative (US DoE, 2012a) goals to develop reliable, low cost closed-loop tracking can be achieved.

Photographs of various CRS towers (as per Figure 2.4) clearly show that the five largest commercial developers of this technology all use optical targets mounted below the receiver as part of their calibration strategies. Most likely, digital cameras and image processing techniques similar to that of Berenguel *et al.,* (2004) are used to obtain offset information from individual heliostat images reflected onto these targets.

Figure 2.4: Calibration targets (from left to right): Abengoa - PS10; Torresol Energy - Gemasolar; Brightsource Energy - Coalinga; SolarReserve - Crescent Dunes; eSolar - Sierra SunTower.

---

[8] Upon completion in 2013, Ivanpah will be the world's largest solar power plant, its collector field consisting of roughly 175 000 twin garage door-sized heliostats.

Brightsource may be an exception to this since a recent patent application describes a calibration method using a macro array of light sensors embedded in a target surface (Schwarzbach & Kroyzer, 2010). Multiple heliostats are commanded to sweep their beams over the sensor array starting from different directions. Dynamic analysis of brightness values occurring over the entire array is used to deduce tracking offsets for generating improved movement model parameters. Individual image shapes are characterized to update aim points for controlling the total flux distribution of many superimposed images on the receiver. The tiled surfaces of both Coalinga and Ivanpah CRS plants' calibration targets have gaps at the corners of the tiles which may house light sensors to implement this method.

eSolar's calibration strategy is described in a recent patent application (Reznik *et al.,* 2012) which combines several previously discussed concepts (Baheti & Scott, 1980; Stone, 1986; Kribus *et al.*, 2004). Heliostats are arranged in rectangular arrays with camera towers located at the corners of each array. Individual heliostats are periodically commanded to adjust their orientation so that their reflected solar images point toward a specific camera location. A spiraling search method is used if the initial approach fails. A centre of reflection seek method follows to ensure that the solar image is centered on the camera. Once this alignment is achieved, a record containing the heliostat's commanded position, the camera position and the current solar angle is stored. A collection of stored records from across a heliostat's movement range is used to estimate its movement model coefficients which are then used for open loop tracking error correction. The advantage of multiple surrounding cameras is that it allows a wide range of heliostat angle measurements to be taken somewhat independent of the time of day. Sherif (2010) claims that multitasking afforded by this scheme makes it possible to calibrate the entire field of 12 000 heliostats in under 20 sunny days.

Lata *et al.* (2011) reviews the functionality of Torresol Energy's Gemasolar plant a year after commissioning. Four cameras, equally spaced around the tower, monitor a cylindrical calibration target to obtain individual heliostat image offsets for characterizing each heliostat in the field. An interesting additional method noted is the local measurement of each heliostat's pedestal tilt and gravitational deflection (presumably using inclinometers located on the mechanism itself). This allows for a much more accurate initial target approach, thus speeding up the calibration process.

2.5. Conclusion

The concepts reviewed in this chapter form a basis for understanding the strengths and limitations of various control strategies in the context of a CRS heliostat field. The next step is to derive appropriate requirements and high level specifications for a proposed 5 MW_e CRS pilot plant, as will be described in Chapter 3.

CHAPTER 3

Method for a 5 MW_e Heliostat Field Control Architecture

This chapter describes the development of high level sizing-, control-, processing- and networking specifications for the proposed CRS pilot plant's heliostat field control system. These specifications were developed with modularity and scalability in mind. They formed the basis for the prototype heliostat array used to validate the thesis by demonstrating the system's tracking accuracy and overall functionality. The prototype system's detailed implementation will be described in Chapter 5.

3.1. Method Overview

The primary objective of this study, as stated in Chapter 1, is to develop the heliostat field control system architecture for a proposed 5 MW_e CRS pilot plant. The initial requirements call for real-time heliostat tracking combined with an error correction method with the ability to minimize tracking errors over time. Plant size requirements were set for 5 MW_e nominal power output with seven hours of thermal storage capacity. The system should also be able to respond quickly to emergency conditions by defocusing the field or moving all heliostats to their 'stow' position.

A top-down approach was followed for deriving the control system's high level specifications, starting at the initial requirements. Each step had to take into account the outcomes of steps preceding it. A diagram of this process is shown in Figure 3.1, followed by a brief discussion of each step. The rest of the chapter is structured according to these steps.

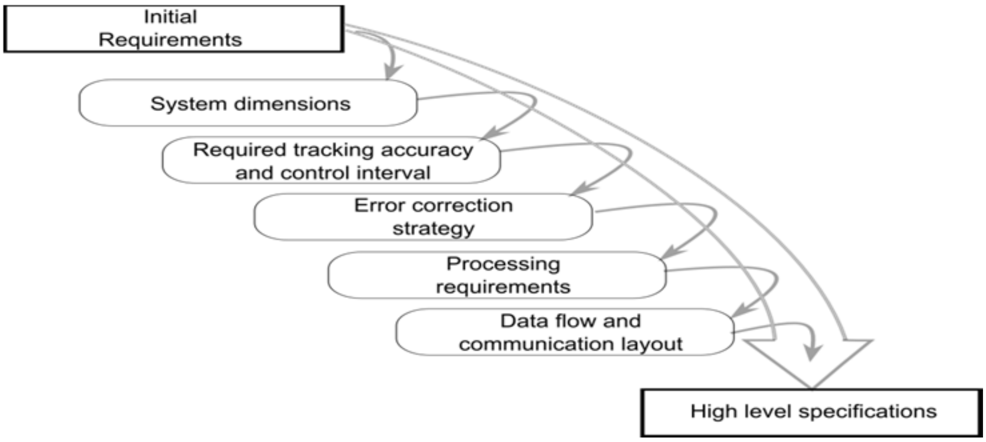

Figure 3.1: Derivation of high level system specifications

1. **System dimensions**

   The required collector aperture for a 5 MW_e CRS pilot plant with seven hours of storage will be determined. This will lead to choices of individual heliostat size, required number of heliostats as well as field configuration and dimensions.

2. **Tracking accuracy and control interval**

   Required angular tracking accuracy is related to the size of the receiver, allowable spillage loss and nominal control interval. The control- and data processing strategies will be affected accordingly.

3. **Heliostat tracking- and error correction strategy**

   The tracking- and error correction strategy is chosen with the required number of heliostats, tracking accuracy and control interval in mind.

4. **Processing requirements**

   The system's processing needs are calculated based on the chosen error correction strategy and the number of heliostats in the system.

5. **Communication network layout and dataflow strategy**

   The communication network architecture is designed according to processing- and dataflow requirements. A dataflow strategy is developed based on processing requirements and tracking- and error correction strategies. This leads to dataflow- and communication network requirements.

3.2. System Dimensions and Tracking Accuracy

This section aims to derive realistic high level specifications without going into details of the prototype implementation. It is intended to be a starting point for planning heliostat tracking functionality with the specific aim of evaluating the proposed open-loop error correction method in the context of a 5 MW_e CRS heliostat field.

3.2.1. Heliostat Field Dimensions

Concentrator aperture area

The required concentrator aperture area depends largely on the following three parameters:

1. Required nominal electric power output (P_e). This was set at 5 MW_e.
2. Required storage capacity. This was set at seven hours under full load operation.
3. Available solar resource, specifically direct normal irradiation (DNI).

To determine a realistic collector size, the parameters of two real world systems are used to define upper and lower boundary values for the proposed pilot plant. Table 3.1 illustrates the impact of thermal capacity on the concentrator aperture-to-power ratio[9] (R_{AP}) of these two systems (NREL, 2012). eSolar's Sierra SunTower system has no storage, so its R_{AP} value forms the lower boundary. Torresol Energy's Gemasolar plant has 15 hours of full load storage and so forms the upper boundary.

Table 3.1: Collector sizes, storage capacities and size-to-power ratios of three CR systems.

	Full Load Storage Capacity [h]	Collector Aperture to Power Output Ratio (R_{AP}) [m^2 / MW]	Nominal Power Output (P_e) [MW_e]	Collector Aperture Area (A_a) [m^2]
Sierra SunTower	0	5 534 (lower boundary)	5	27 670
Gemasolar	15	15 314 (upper boundary)	19.9	304 750
The proposed pilot system	7	10 000 (rounded 7h value)	5	50 000

The lower boundary ($R_{AP,lower}$) was assumed to be the minimum ratio required to generate power without storing any excess energy. The difference between the upper- and lower ratio boundaries was used to estimate the extra R_{AP} required for every additional hour of storage. This value was multiplied by seven to calculate the storage ratio for seven hours of full load storage ($R_{AP,7h}$) as follows:

$$R_{AP,7h} = R_{AP,lower} + 7h\left(\frac{R_{AP,upper} - R_{AP,lower}}{15h}\right) \tag{3.1}$$

$$= 10\ 098\ m^2 / MW_e \text{ which was rounded to } 10\ 000\ m^2.$$

A collector aperture of roughly 50 000 m^2 is therefore required to produce 5 MW_e.

Number of Heliostats

The optimal size of heliostats for utility scale CRS plants has not yet been established (Kolb *et al.*, 2011), with current commercial designs ranging from 1.14 m^2 (eSolar) to 120 m^2 (Sener, Abengoa, Solar Reserve). However, recent trends indicate a shift towards smaller, smarter heliostats (§2.3). For this reason, eSolar's heliostat size was chosen as the lower boundary at 1.14 m^2 and Brightsource's heliostat size of 15 m^2 (NREL, 2012a) as the upper boundary.

Individual heliostat aperture was chosen to be 5 m^2. Two factors influenced this choice toward the smaller end of the range initially identified. Firstly, small heliostats

---

[9] We calculate this ratio by dividing the collector aperture (A_a) by the nominal power output (P_e).

generally have better optical performance than larger ones (Landman, 2013). This coincides with the SUNSPOT cycle's requirement for high solar flux concentration (Kröger, 2012). Secondly, a purely pragmatic consideration was for convenience and reduction of risk to personnel during installation and operation, especially in the context of a university pilot project. Since the total system aperture is the product of individual heliostat aperture and the number of heliostats in the field, it follows that for a total aperture area of 50 000 m^2, the system would require 10 000 heliostats.

Heliostat field dimensions

A field layout similar to that of a single twin-field eSolar tower module was assumed. A packing ratio of 0.5 was used, thus requiring a total field area of 100 000 m^2, excluding spacing for the tower and access roads. Figure 3.2 shows a comparison between an actual eSolar twin field module (left) and the proposed system's 100 000 m^2 field area (right).

Figure 3.2: An eSolar twin-field tower module (left) and a proposed layout for the 100 000 m^2 system (right). (Source: Palmer, 2011).

3.2.2. Tracking accuracy and control interval

To an earthly observer, the sun appears as a disk having a near constant radiation distribution over its surface. Any heliostat's ability to concentrate sunlight is limited by the subtending angle (Ω_S) of the solar disk (Figure 3.3).

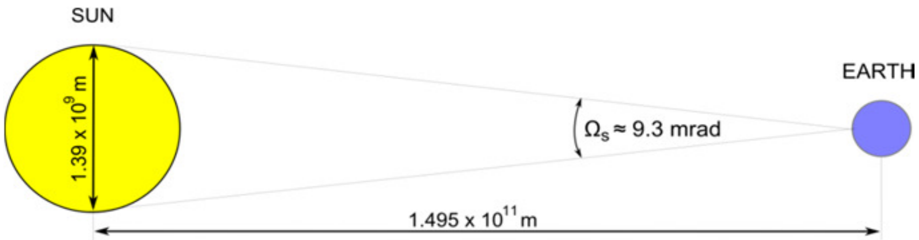

Figure 3.3: Subtended angle of the solar disk. (Adapted from Duffie & Beckman, 1980:5)

The smallest image diameter that an ideal heliostat can project onto a receiver plane is the product of the sun's subtending angle (approximately 9.3 mrad) and the heliostat-to-receiver distance or slant range (L_{slant}). The smallest theoretical image size of a plant's furthest heliostat is typically used as a close approximation for specifying the receiver aperture size (Stine & Geyer, 2001: §10.1.2). It therefore makes sense to relate the required tracking accuracy of a heliostat to the fraction of its flux that is required to fall within this optimal reflected image area.

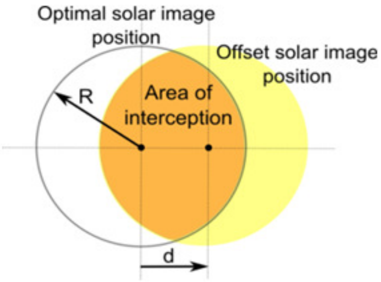

Figure 3.4: Area of intersection between an offset heliostat solar image and its ideal image.

Referring to Figure 3.4, the area of interception can be expressed as a function of the optimal image radius (R) and the offset distance (d) between it and the actual solar image as a result of tracking error (Weisstein, 2013):

$$A_{intercept} = 2R^2 \cos^{-1}\left(\frac{d}{2R}\right) - \frac{d}{2}\sqrt{4R^2 - d^2} \tag{3.2}$$

where

$$R = 2L_{slant}\left(\frac{\Omega_s}{2} + \sigma_{slope}\right) \text{ and } d = 2L_{slant}\,\Delta_H$$

and where Ω_s is the sun's subtended angle, σ_{slope} is the heliostat's mean slope error and Δ_H is the angular tracking error of the heliostat normal vector. Equation (3.2) is simplified to yield an intercept ratio (R_I) normalized for slant range:

$$R_I = \frac{4(k)^2 \cos^{-1}\left(\frac{\Delta_H}{2k}\right) - \Delta_H\sqrt{4k^2 - {\Delta_H}^2}}{2\pi k^2} \quad \text{with} \quad k = \frac{\Omega_s}{2} + \sigma_{slope} \tag{3.3}$$

Figure 3.5 shows a plot of equation 3.3, with $\Omega_s = 9.3$ mrad and $\sigma_{slope} = 1.5$ mrad, which is representative of the slope error typically found in industry standard heliostats (Kolb *et al.,* 2011:68; Mancini *et al.,* 2000). Note that a tracking error of one milliradian results in around ten per cent reduction in the heliostat image intercept ratio.

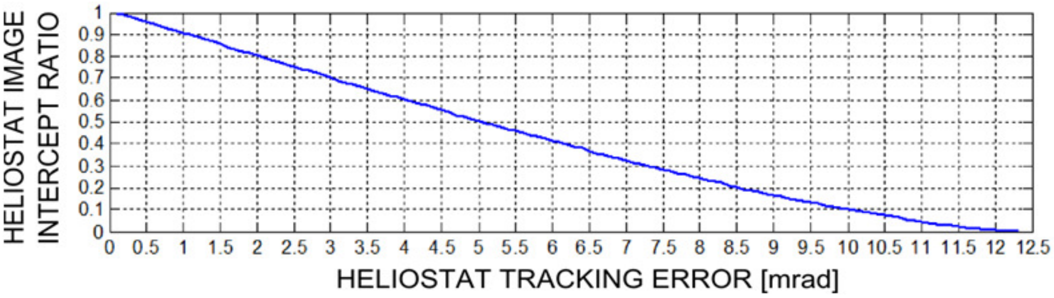

Figure 3.5: A typical heliostat image's flux intercept ratio versus tracking error angle.

The average industry standard tracking error (Δ_H) is 0.75 mrad as per specifications of nine commercial heliostats evaluated in a prominent cost reduction study by SANDIA Labs (Kolb *et al.,* 2007:78). This value yields a 92.2 per cent ratio of intercept area (R_I) using Equation 3.3 with $\Omega_S = 9.3$ mrad and $\sigma_{slope} = 1.5$ mrad. Compared to this figure for commercial heliostats, the one milliradian accuracy objective for the prototype system seems ambitious but also appropriate to a real world system.

The control interval (t_c) is the time period between consecutive heliostat adjustments and causes an approximate heliostat tracking delay angle ($\theta_{h,delay}$) of $\omega_{earth} t_c$, where ω_{earth} is the average angular velocity of the earth[10]. We can now calculate the maximum allowable control interval based on the required tracking accuracy. It was assumed that each heliostat's orientation would be adjusted at discreet time intervals instead of using a continuous drive strategy like what is proposed by Kribus *et al.* (2003).

It follows that each heliostat's orientation should be updated at least once every 13 seconds to restrict the drift of its reflected solar image to below one milliradian on the receiver[11]. If network bandwidth or processing resources are limited, this period could be extended by extrapolating extra adjustment steps in the local controller between actual control commands.

3.3. Control Strategy

Heliostat tracking errors reduce the annual energy yield of a CRS plant and may allow potentially damaging temperature gradients to occur on the receiver surface (Camacho *et al.,* 2010). It was shown in §3.2 that the proposed 5 MW$_e$ system needs to control up to 10 000 heliostats in real time while keeping the average normal vector error of each heliostat below one milliradian. An accurate and highly scalable tracking- and error correction strategy is needed to realize these requirements. A

---

[10] One rotation in 24 hours = 2π / (24*3600) = 7.27E-5 rad/s

[11] 1 [mrad] / 0.07272 [mrad/s] ≈ 13.75s.

range of heliostat field control methods from literature were reviewed in §2.2. Knowledge about these concepts is now consolidated to arrive at a suitable method for the proposed pilot plant system.

3.3.1. Conventional Open- and Closed Loop Control

Figure 3.6 shows a generic control system diagram with a reference input (I) for open loop control and three realistic feedback signal pathways (A, B, C) for closed loop control of a heliostat.

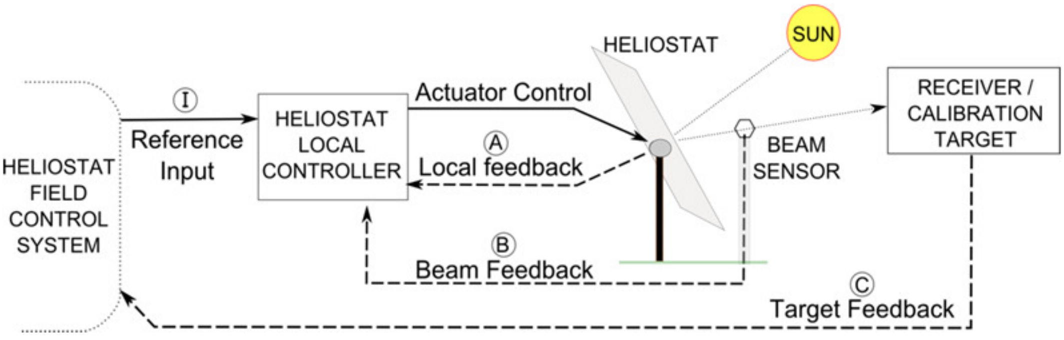

Figure 3.6: Control signal pathways for heliostat tracking control

Closed Loop Tracking

Real-time feedback signals are interpreted by a local control unit to generate actuator drive signals for continuously adjusting the heliostat orientation.

A) Local feedback originates from sensors located on the heliostat mechanism itself:

   i. Low resolution quadrature encoders[12] can provide position feedback of each drivetrain's motor shaft, but since this signal pathway originates at the start of the drivetrain, it cannot account for errors introduced later on - like mechanism reference frame offsets, non-linearity, backlash and gravity sag.

   ii. High resolution rotary encoders installed on the heliostat's output axes can account for non-linearity and backlash, but cannot measure reference frame offsets or gravity bending.

   iii. Feedback of the heliostat normal vector orientation (relative to gravity) may be provided by sensors installed directly on the mirror surface – typically multi-axis accelerometer- or inclinometer micro-electromechanical systems (MEMS). This type of sensor still only

---

[12] A quadrature encoder is a simple electromechanical device that represents magnitude and direction of angular rotation as two square wave signals, 90° out of phase relative to each other.

provides part of the picture as it cannot measure azimuthal orientation and are subject to installation tolerances.

B) The concept of beam feedback relies on incident light angle sensors located between each heliostat and the receiver (Quero *et al.,* 2007). This scheme is still in a development phase and requires extremely accurate sensor installation and needs periodic recalibration in case of long term deformation of either the heliostat or sensor support structures.

C) Target feedback measures a heliostat's reflected image position at the system output, thus taking all error sources into account. Several methods have been proposed (Convery, 2010, 2011; Kribus *et al*., 2004). In real world CRS plants, the fact that hundreds or even thousands of heliostat images overlap on the same area of the receiver makes it difficult to distinguish between individual heliostat beams for real-time closed loop control. Instead, feedback from individual heliostats is typically obtained on calibration targets separate from the actual receiver.

Open Loop Tracking

To avoid the high tolerance requirements of feedback sensors installed at every heliostat, all known commercial CR systems make use of solar position algorithms as part of their heliostat tracking strategies (Camacho *et al*., 2012). Advances in microprocessor technology and the availability of highly accurate solar position algorithms provide accuracy, flexibility and repeatability at relatively low cost.

However, systemic error sources occur in open loop solar tracking systems due to misalignment between the local- (heliostat) and global reference frames. This misalignment is due to heliostat manufacturing-, installation- and alignment tolerances as well as control system errors associated with the solar position algorithm, control interval, processor floating point accuracy and timing uncertainty (Stone & Kiefer, 1998; Berenguel, 2004; Camacho, 2012).

Typical heliostat tracking errors vary over the course of days and seasons due to the error geometry introduced by the various sources mentioned above, combined with the relative earth-sun movement (§2.1). If left uncorrected, all of these sources contribute their own error component to the heliostat's ideal tracking movement. Typical heliostat tracking errors cannot be corrected by once-off (static) offset adjustments and therefore require a sophisticated error correction method which takes into account the time variability of errors.

3.3.2. Model based error correction

The method described combines elements of open- and closed loop control to get the benefits of both while avoiding problems associated with exclusive use of either. The method generally comprises three steps (Jones & Stone, 1999):

1. A hardware-specific error model is developed which describes the misalignment of a heliostat's actual normal vector compared to an ideal

commanded position. The transformation from the reference axes to the real axes consists of a series of translation- and rotation steps, each corresponding to a specific error source.

2. A series of time-separated measurements are made to obtain operational tracking error data of individual heliostats over a predetermined period. This data is used to estimate parameters for the error model developed in step 1.
3. The estimated parameters are applied to the model, which is used to predict and correct the heliostat's tracking errors in real time.

Concept of operation

The proposed signal acquisition method is similar to that of Berenguel *et al.* (2003). Figure 3.7 illustrates the concept.

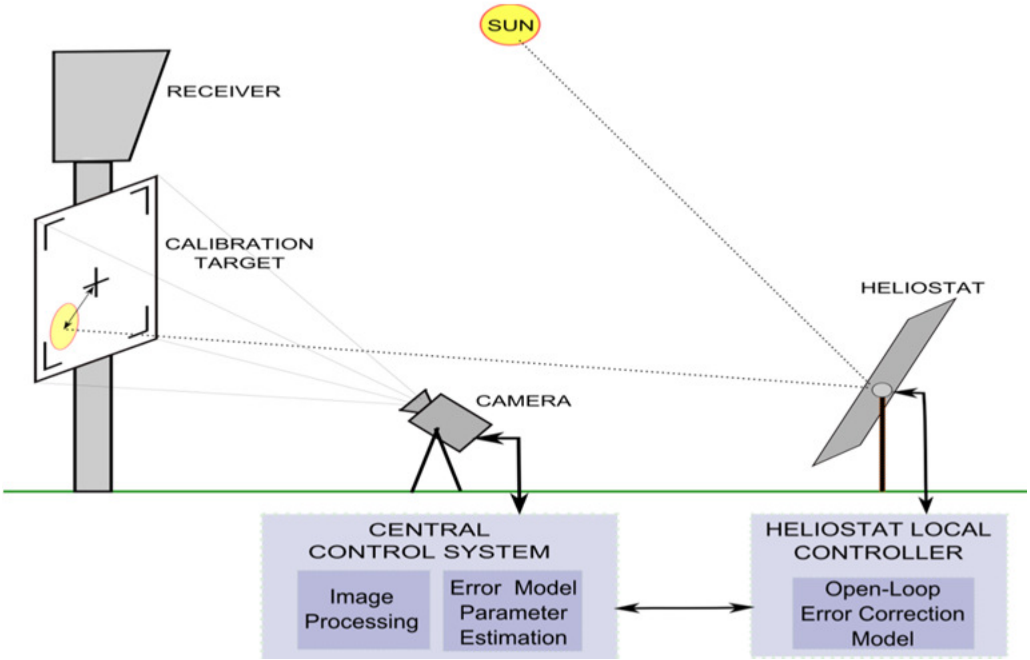

Figure 3.7: Concept of operation of the heliostat field control system

Every heliostat in the system is periodically commanded to aim its reflected solar image at a calibration target separate from receiver. A camera located in the field photographs the solar image projected by an individual heliostat onto the target and transfers the digital image to a central computer. Image processing techniques are used to calculate a time-stamped set of aim point error offsets for each heliostat. Due to the large number of heliostats it typically takes several weeks to obtain calibration measurements of the entire array. This means that any corrections applied to a heliostat should be valid at least until the next set of measurements can be taken.

Successive datasets are used to calculate and refine error model parameters for each heliostat in the field. The parameters are stored in each heliostat's local control unit (LCU) from where it is used to predict and correct tracking errors in real time. The geometric error model and the mathematical optimization process used to characterize each heliostat are discussed in Chapter 4.

3.4. Processing strategy

A number of system tasks need to be processed with varying degrees of expediency. Some have hard real-time deadlines while others can be post-processed at night. It follows that tasks need to be categorised and allocated to an appropriate subsystem for processing.

3.4.1. Requirements

At this stage in the high level design process, the primary requirements for the processing strategy can be summarized as follows:

- The system should be able to adjust 10 000 heliostats at least once during every control interval.
- Each heliostat needs to adjust its alignment at least once every 13 seconds. This translates to a maximum allowable adjustment resolution of one milliradian, as discussed in (§3.2.2).
- All heliostats should employ open loop tracking.
- At least one digital camera should be used to periodically record and store images in a database. Image processing and error parameter estimation should be performed on sets of reflected solar images from individual heliostats.
- Real-time model-based tracking error correction should be applied using an individual error parameter set for each heliostat in the system.
- The system should be able to interact with the user by accepting input and displaying information as required. The user should be able to store, retrieve and update any heliostat's field location, aim point or individual error parameters.
- The system should be able to respond quickly to alarm conditions. Specifically, the entire heliostat field should be able to defocus to below ten per cent of nominal flux on the receiver within 30 seconds from when an alarm condition is raised by the central controller. In high wind conditions, heliostats should be able to reach their safe stowed positions within five minutes.

Many diverse strategies could satisfy the primary requirements, so preference should be given to those which can contribute to:

- Cost reduction
- Simplicity
- Increased final tracking accuracy
- Modularity and/or scalability
- Increased reliability and/or redundancy

3.4.2. Overview of specific tasks

Heliostat actuator control

Each heliostat needs to continuously adjust its orientation in two axes. This requires at least one independent actuator per axis, each with its associated driver unit containing power electronics and logic. To reduce cabling costs and power losses, high current path lengths should be minimized by locating power electronics close to the actuators. Each heliostat should therefore have its own set of actuator driver units. Control signals ('move', 'direction' and 'enable' at least) for the drive units need to be generated in real time during each control period.

Heliostat vector calculation resolution

The required normal vector of each heliostat in the field needs to be calculated in real time. The calculation method is described in Chapter 4 as part of the error model derivation. Each heliostat in the prototype system should maintain a tracking error below one milliradian. Therefore, if no other error sources are considered, the minimum resolution for adjustment of each heliostat axis should be 2π / 0.001 ≈ 6283 steps per rotation. However, since provision needs to be made for other error sources and the vector calculations will be done in a microcontroller environment, the obvious choice is to use a 16-bit integer for each axis angle variable. With a range of 0 to 65535, this results in a logical step resolution of 0.096 milliradian over a 2π range, thus exceeding the resolution requirement by more than a full order of magnitude.

Solar position calculation

Open loop heliostat tracking requires accurate solar angle information to be available at each control interval. An algorithm is used to calculate the solar angle based on stored (static) local longitude and latitude and the current (dynamic) date and time.

Any solar algorithm's processing- and memory requirements are highly dependent on its use of numerical methods (polynomial lookup tables) versus analytical formulas and the period over which the algorithm remains accurate. Of the solar algorithms discussed in §2.1.2, SPA by Reda & Andreas (2008) is clearly the most accurate, but also by far the most computationally expensive. It is useful for theoretical- or benchmarking applications, but may be considered overkill in many engineering applications where the measurement noise floor and minimum actuator resolution is typically much higher than the accuracy this algorithm provides.

The ENEA algorithm (Grena, 2007) was chosen for the system proposed here. Although it is less accurate than SPA by almost a full order, it is about 20 times computationally cheaper (Blanc & Wald, 2011). This allows for implementation in low cost embedded microcontrollers while still yielding results that are accurate enough even for central receiver systems with high concentration ratios.

Image processing

Large numbers of digital images need to be processed to calculate the position offsets of the heliostats' projected solar images on a calibration target. This task requires large amounts of memory, secondary data storage and processing power and is therefore typically performed by a central computer.

Error model parameter estimation

A mathematical optimization technique is used to calculate sets of parameters that produce a good fit of model-predicted data points compared to a set of measured data. This typically requires many thousands of iterations to be performed for each calculated set of error parameters and is therefore performed by a central computer with large processing power and memory resources.

Operator interface (GUI) and calibration control

The system needs an interface whereby the user can readily monitor and adjust system status and individual heliostat parameters, do fault finding, etc. It should also allow overriding of any part of the control system. These tasks are typically handled by a central computer at the 'top' of the control system hierarchy.

3.4.3. Distributed Processing

Each processing task had to be allocated to an appropriate part of the control system. Tasks could either be centralized or divided between a large number of distributed processors. At the centralized end of the spectrum, all tasks would be allocated to a central controller. This approach would require a powerful computer to calculate all actuator control signals in real time. A complex communication network would then have to distribute these signals to each of (at least) 20 000 heliostat actuators[13] and relay back their position feedback signals, all in real time. At the decentralized end of the spectrum, each heliostat could be made completely autonomous by having its own source of time and a powerful local processor to perform all tasks locally. It is clear that neither of these approaches would have been optimal.

Recent trends in CSP control systems show decentralization of low level control tasks, largely due to the affordability and flexibility of modern microcontrollers (Camacho *et al.,* 2012:247). A distributed processing strategy was chosen whereby some tasks would be centralized and others localized. Figure 3.8 shows how the main processing tasks were ranked according to required processing resources and frequency of execution. There clearly exists a strong inverse proportionality between these two parameters across the spectrum of processing tasks.

---

[13] At least two actuators for each of the 10 000 heliostat (one per movement axis).

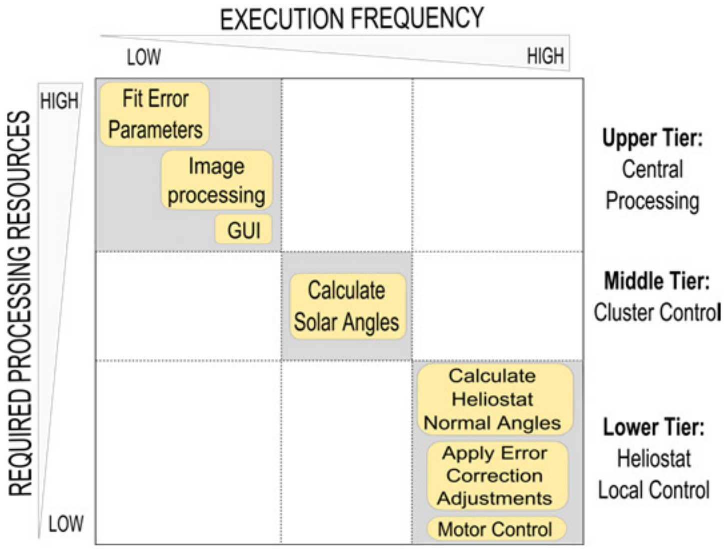

Figure 3.8: Processing resource requirements and execution frequency of main tasks

Based on their respective rankings, tasks were grouped into three tiers as indicated by the shaded blocks. Note that tasks from both the middle- and lower tiers need to be executed once every control period. However, tasks in the lower tier need to be performed for each heliostat with unique parameter values (thus effectively multiplying the execution frequency by the number of heliostats), while the same solar angle values are valid for the entire field.

The three processing tiers and high level dataflow are shown in Figure 3.9. Arrows indicate the flow of information up and down the processing hierarchy.

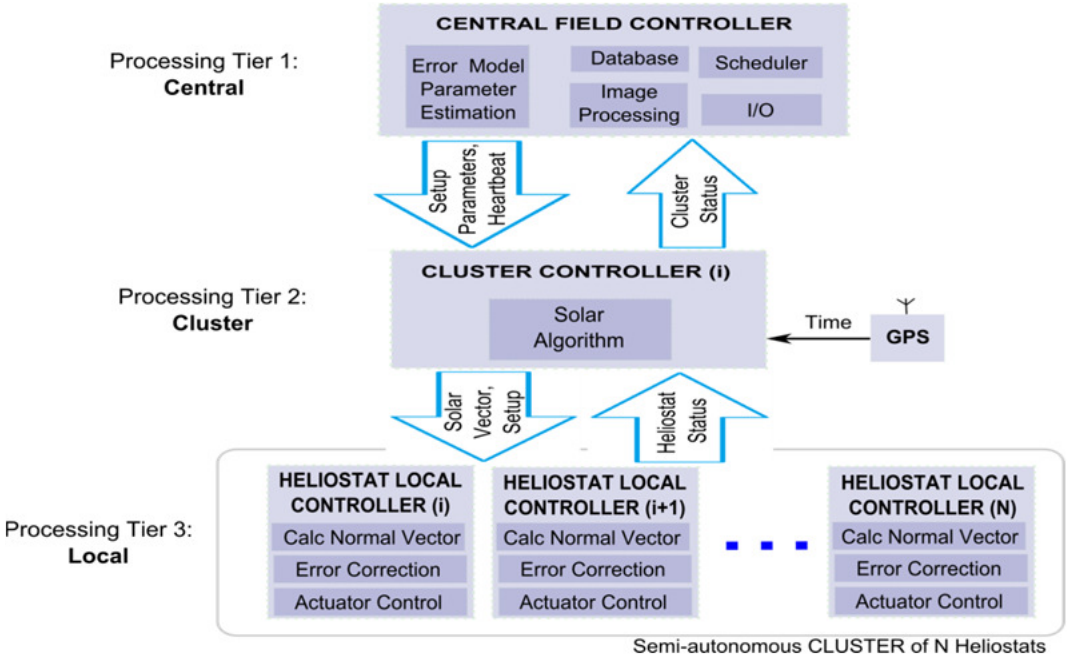

Figure 3.9: Distribution processing of tasks into three tiers (dataflow is indicated by arrows).

Lower Tier: Heliostat Local Control

For each control period, the required heliostat normal vector has to be calculated and error corrections applied based on calibration parameters stored in local memory. Control signals must then be supplied to the actuators for aligning the heliostat mechanism.

The heliostat local controllers need to be low cost devices because every one of 10 000 heliostats needs one. Various relatively simple 8-bit microcontrollers could be used for this purpose. These devices typically do not have specialized communication peripherals (like Ethernet or Universal Serial Bus (USB), for instance), so a serial communication protocol was chosen to link it with the rest of the system.

Middle Tier: Cluster Control

Heliostats are grouped together in clusters, each falling under the control of a cluster controller unit (CCU). These CCUs together make up the middle processing tier. GPS receivers are used to provide accurate time and date information to each cluster controller. Real-time solar angles are calculated using a solar algorithm and passed down to the local processing tier. This means that each cluster handles all its own real-time processing needs and can therefore function independently from the rest of the system if necessary. This results in self-sufficient heliostat clusters, which meets the system's secondary requirements for modularity, scalability and reliability.

Each CCU is linked to the upper processing tier to accept setup parameters and to relay configuration- and status data between the central controller and the heliostat local controllers.

Upper Tier: Central System Controller (CSC)

The CSC needs to perform a number of predominantly non real-time tasks, including processing of tracking measurements, estimation of coefficients for the error model (Chapter 4) and a number of system overview- and operator interface tasks. A detailed description of its implementation in the prototype system is provided in Chapter 5.

3.5. Communication strategy

For thousands of heliostats to function as an integrated solar concentrator, a communication network is required to send and receive information between devices. This section summarizes the development of a high level strategy for transmitting data between the three processing tiers. This strategy will later shape the detailed hardware and software implementation of the prototype system (Chapter 5).

The scope of this document allows us to touch only briefly on digital networking concepts. The reader is referred to Kuphaldt (2007: 433-454) for an excellent overview of the subject, including the seven layer Open Systems Interconnection network model, various network topologies and protocols, channel arbitration, data flow, etc.

3.5.1. Addressing, data protocol and bandwidth

Minimum addressing- and bandwidth requirements were first determined. This influenced the choice of network topology. Once the topology was decided, a suitable channel access method had to be chosen based on the required bandwidth per communication channel.

Addressing

Each node in the network should be assigned a unique address. Any message sent over the network should contain the address of the destination node and that of the originating node. This ensures that only the addressed node unpacks and processes any particular message. It also allows the receiving node to treat the message according to where it came from.

Error Detection

It is desirable to know whether a message arrives intact or whether it got corrupted along the way. Corrupt messages can be ignored or a request can be sent for the message to be retransmitted, thereby greatly increasing network reliability. Error detection in digital networks is typically achieved by adding a cyclic redundancy code (CRC) to the end of all messages. This code is determined by a CRC algorithm and is a function of all the individual bytes in a message. The receiving node uses the same algorithm to calculate the received message's CRC and compares it to that which the originating node calculated and added to the message. Complex algorithms exist which minimizes probability of corrupted messages being internally consistent with the generated CRC (Williams, 1993).

Data Protocol

A data protocol was defined to standardise the way that data is transmitted and received by all nodes in the network. To keep message lengths short, a proprietary packet structure was proposed, based loosely on the MODBUS protocol (modbus.org, 2012). At a minimum each packet should contain:

- Receiver address (two bytes allows up to $2^{16} = 65536$ unique addresses)
- Destination address (two bytes)
- Message type (one byte allows up to 256 message types)
- Data payload (six bytes[14])
- CRC (one byte).

---

[14] §3.4.2 showed that two bytes are needed per axis to describe each heliostat's normal angle at sufficient resolution. For future drivetrain flexibility, we use three bytes per axis, so six bytes in total.

Required Bandwidth

This adds up to a minimum of 13 bytes which has to be transmitted by a heliostat's local controller to periodically report its axis position counts. If during normal tracking, each heliostat reports its position once during every control interval, the minimum required system bandwidth is 10 000 x 13 = 130 000 kBps or 1.3 Mbps[15]. In practical applications, this figure would be multiplied by a factor of 5 – 10 to compensate for latency and to allow some 'dead time' in between packets. 'Dead time' denotes a period when all nodes refrain from transmitting. Its purpose is to limit the probability of transmission conflicts due to imperfect synchronization between network nodes (Treurnicht, 2013).

3.5.2. Network Topology

The grouping of heliostats into clusters (§3.4.3) and the hierarchical nature of the distributed processing strategy suggests the use of a three-level branched star- and/or bus topology. Figure 3.10 shows simple star- and bus topologies.

Figure 3.10: Star network topology (left) and bus topology (right).

The star topology connects each node to a network switch or hub via a dedicated communication channel (typically a length of cable or a dedicated radio channel). This implies full channel bandwidth for every node, but at relatively high cost due to the need for many channels and a network switch. In a bus topology, all nodes share the same channel, implying low cost at the expense of dividing channel bandwidth between nodes.

For the proposed pilot plant control system, the large number of low bandwidth LCU nodes point toward using a bus topology for each heliostat cluster. Conversely, a star topology should be used for the relatively low number of higher bandwidth connections linking CCUs to the central control system, as per Figure 3.11.

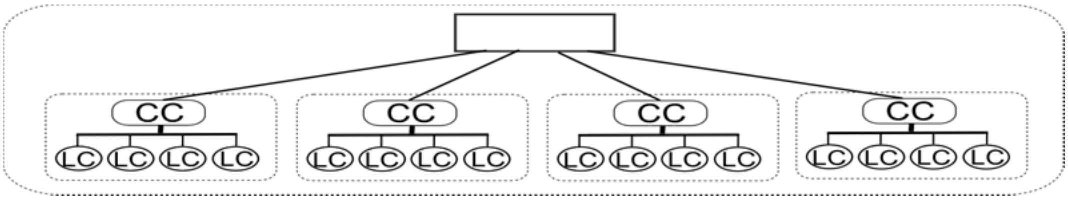

Figure 3.11: Combined star- and bus network topology.

---

[15] 'Bps' and 'bps' denotes bytes per second and bits per second, respectively. The conventional 8N1 byte has 8 data bits, no parity bit, one start bit and one stop bit. Therefore, 1 Bps equals 10 bps.

Channel Access

When multiple network nodes share the same physical medium, a channel access method should be used to avoid data loss and/or corruption from multiple nodes transmitting simultaneously. Our chosen network topology dictates that a customised channel access method is needed only for the serial bus connections between heliostats and their CCUs

Horak (2007: 557-562) describes various methods for arbitrating multiple access on a channel. Time division multiple access (TDMA) relies on the principle of dividing the channel into time slots. TDMA was chosen as the channel access method for the proposed system due to its simplicity and low cost of implementation, since system-wide synchronization is already provided to each CCU via GPS. Chapter 5 describes the detailed implementation as part of the prototype system details.

3.5.3. Heliostat Cluster Size and Network Layout

It was decided to restrict the number of heliostats per cluster to below 50 for the following reasons:

1. To manage the risk of hardware failure. Each cluster controller is responsible for providing solar angle information to all heliostats below it. If one should fail, all heliostats below it would stop operating. The impact on the system is therefore directly proportional to cluster size.
2. To reduce the communication load and complexity (particularly the timing accuracy requirement for TDMA) on each cluster- to local controller bus.

A cluster size of 32 corresponds to the maximum allowable number of nodes on a single RS485 bus. This means that a heliostat array of 10 000 would need 313 cluster controllers, each communicating fairly infrequently with the central controller. System complexity can be reduced by using off the shelf Ethernet-to-serial switches. Multiple switches can be linked on a single Ethernet backbone to address up to 1024 serial ports on a single network (Cyclades Corporation, 2004:133).

Figure 3.12 shows one possible wired layout which could allow up to 48 heliostat clusters, each containing 32 heliostats to form a sector of 1536 nodes. Such a layout could clearly be scaled up to include a large number of heliostats by simply adding more sectors to the Ethernet backbone.

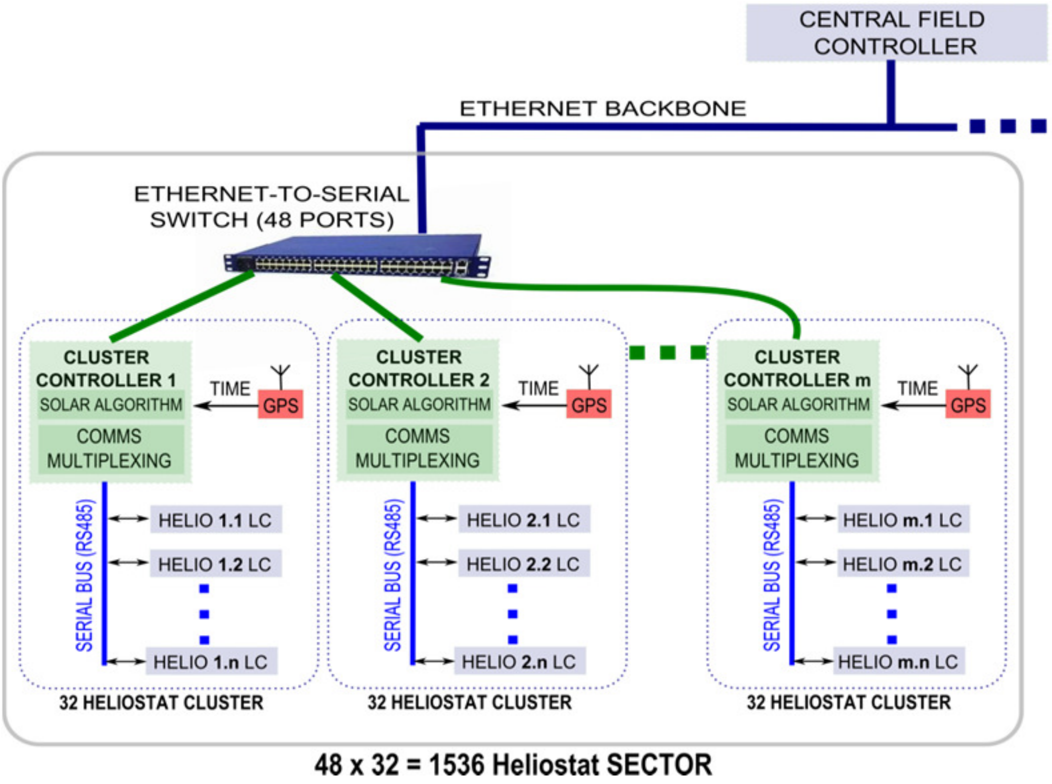

Figure 3.12: One possible wired network layout with good scaling potential.

A network topology similar to that of Figure 3.12 could be implemented with low cost wireless communication modules to reduce cabling and network installation costs. This concept is referred to by Camacho (2012:248) as well as in a recent paper by Kubisch *et al.,* (2011) about using ZigBee wireless mesh networks for controlling thousands of self-powered heliostats.

3.6. Conclusion

This chapter derived all elements needed to proceed with developing the heliostat error model (Chapter 4) and with implementing the various high level specifications into a modular, scaled down prototype system (Chapter 5).

CHAPTER 4

Heliostat Error Model

The error correction method described in Chapter 3 relies on characterizing individual heliostats' movement to predict and correct tracking errors in real time based on previous measurements. This chapter derives an error model to describe the kinematics of a generic azimuth-elevation heliostat. The model calculates the heliostat's reflected image offsets on a calibration target plane for a range of input parameters including heliostat location, solar angle and eight error parameters. Mathematical background to the model is provided, after which individual error parameters are explained and modelled. A step by step derivation of the error model follows before describing the optimization process by which model coefficients are estimated to best fit a set of measured tracking errors from a specific heliostat.

4.1. Mathematical Background

A number of vectors and angles are defined which describe the geometry of a generic heliostat. This is followed by an overview of 3D transformations used in the model.

4.1.1. Heliostat Geometry

The geometry described here generally follows the section on concentrator optics in *Power From the Sun* (Stine & Geyer, 2001: §8.5). A Cartesian coordinate system is used to describe the position of a heliostat relative to the receiver in three dimensions. A zenith, east, north coordinate system is convenient for describing the heliostat field and will be used throughout the rest of this document. Figure 4.1 shows the spatial relationship between a heliostat, its aim point and the sun.

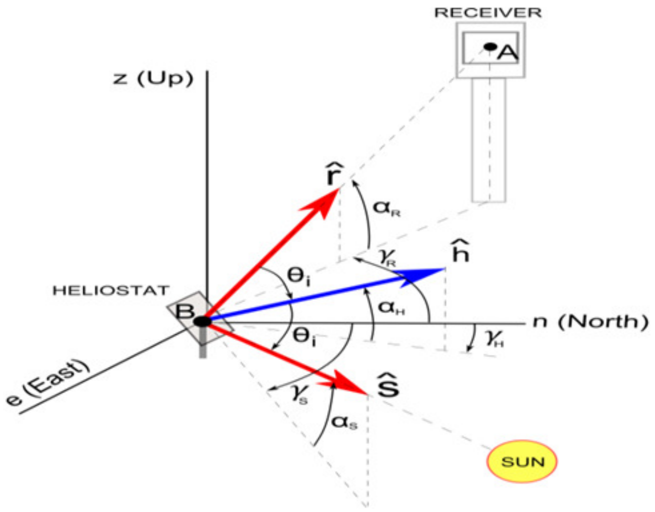

Figure 4.1: Vectors and angles in heliostat geometry (adapted from Stine & Geyer, 2001:8.5).

- The heliostat is located at B (z_1, e_1, n_1). Its surface normal vector ($\hat{h}$) can be described by azimuth- (γ_h) and elevation (α_h) angles.
- The heliostat's aim point *A* (z_0, 0, 0) is normally at the centre of a receiver located at the top of a tower. The base of the tower is located at the origin (0, 0, 0).
- The solar unit vector ($\hat{s}_i$) is described by its solar azimuth- (γ_S) and elevation (α_S) angles.

Three vectors are defined, each with its origin at the intersection of the heliostat's elevation- and azimuth axes:

1. The heliostat-to-target unit vector ($\hat{r}$) from the heliostat to the receiver:

$$\hat{r} = \frac{(z_0 - z_1)\hat{\imath} - e_1\hat{\jmath} \; - n_1\hat{\mathrm{k}}}{\sqrt{(z_0 - z_1)^2 + e_1{}^2 + n_1{}^2}} \tag{4.1}$$

   where $\hat{\imath}$, $\hat{\jmath}$ and $\hat{\mathrm{k}}$ are unit vectors in the zenith-, east- and north directions, respectively.

2. The solar position unit vector ($\hat{s}$) is essentially the same for all heliostats in the field, expressed in terms of the solar azimuth- (γ_S) and elevation angle (α_S):

$$\hat{s} = s_z\hat{\imath} + s_e\hat{\jmath} + s_n\hat{\mathrm{k}} \tag{4.2}$$

   where $s_z = \sin(\alpha_s)$, $s_e = \cos(\alpha_s)\sin(\theta_s)$, $\hat{s}_n = \cos(\alpha_s)\cos(\theta_s)$

3. The heliostat unit normal vector ($\hat{h}$) is expressed as

$$\hat{h} = h_z\hat{\imath} + h_e\hat{\jmath} + h_n\hat{\mathrm{k}} \tag{4.3}$$

4.1.2. Ideal Heliostat Normal Vector

To find the ideal heliostat normal vector ($\hat{h}_i$), the required angle of incidence (θ_{i}) of the solar vector relative to the heliostat first needs to be calculated. For specular reflection, the angle of incidence θ_{i} is be equal to the angle of reflection (θ_{r}) so that

$$\cos(2\theta_{\mathrm{i}}) \; = \; \hat{s} \cdot \hat{r} \tag{4.4}$$

and therefore

$$\theta_{\mathrm{i},i} = \frac{\cos^{-1}(\hat{s}\cdot\hat{r})}{2} \tag{4.5}$$

The required heliostat normal vector is found by adding the solar unit vector to the heliostat-to-target unit vector and dividing by twice the cosine of the incident angle:

$$\hat{h} = \frac{\hat{r} + \hat{s}}{2\cos(\theta_i)} \tag{4.6}$$

4.1.3. Translation and Rotation

Rotation relative to the principle axes

Using the Cartesian coordinate system for three dimensional space, any body (or set of points) may be rotated around the X-, Y- or Z-axis using the right-hand rule as shown in Figure 4.2.

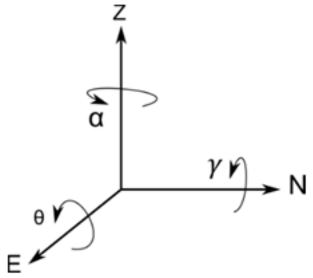

Figure 4.2: Rotation relative to the Cartesian axes.

The matrices for rotation around the x-, y- and z-axes are as follows (Murray *et al.*, 1994: 31):

$$R_Z(\alpha) = \begin{bmatrix} 1 & 0 & 0 \\ 0 & \cos\alpha & \sin\alpha \\ 0 & -\sin\alpha & \cos\alpha \end{bmatrix} \tag{4.7}$$

$$R_E(\theta) = \begin{bmatrix} \cos\theta & 0 & -\sin\theta \\ 0 & 1 & 0 \\ \sin\theta & 0 & \cos\theta \end{bmatrix} \tag{4.8}$$

$$R_N(\gamma) = \begin{bmatrix} \cos\gamma & \sin\gamma & 0 \\ -\sin\gamma & \cos\gamma & 0 \\ 0 & 0 & 1 \end{bmatrix} \tag{4.9}$$

Rotation around an arbitrary axis

The rotation of a body about any fixed axis can be described using the Euler vector ($\hat{e}$) and a rotation angle (θ), as shown in Figure 4.3.

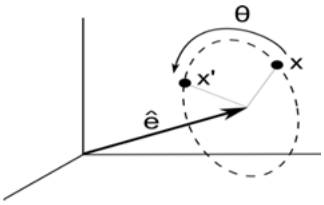

Figure 4.3: Rotation described by an Euler vector and angle.

The Rodrigues Rotation Formula (Murray *et al.,* 1994:28) is used to calculate the corresponding rotation matrix (*R*) as follows:

$$R = I_3 \cos(\theta) + (1 - \cos(\theta))[\hat{e}]_X[\hat{e}]_X^T + [\hat{e}]_X \sin(\theta) \tag{4.10}$$

$$\text{where } [\hat{e}]_X = \begin{bmatrix} 0 & e_3 & -e_2 \\ -e_3 & 0 & e_1 \\ e_2 & -e_1 & 0 \end{bmatrix} \quad \text{and } I_3 = \begin{bmatrix} 1 & 0 & 0 \\ 0 & 1 & 0 \\ 0 & 0 & 1 \end{bmatrix}$$

Homogenous Transformation Matrix

A 4 x 4 matrix can be defined to represent a rotation and translation operation (first rotation, then translation) as follows:

$$\begin{bmatrix} x' \\ y' \\ z' \\ 1 \end{bmatrix} = \begin{bmatrix} R_{11} & R_{12} & R_{13} & t_z \\ R_{21} & R_{22} & R_{23} & t_e \\ R_{31} & R_{32} & R_{33} & t_n \\ 0 & 0 & 0 & 1 \end{bmatrix} \begin{bmatrix} x \\ y \\ z \\ 1 \end{bmatrix} \tag{4.11}$$

where the 3 x 3 $[R]$ matrix represents rotation and the 3 x 1 $[t]$ vector represents translation.

4.2. Error Model Derivation

This section shows the step by step derivation of the error model. An ideal heliostat's required normal vector is first calculated based on its position relative to the receiver and the sun, as per §4.1.2. Next, a series of 3D translations and rotations are used to simulate mechanism-specific error parameters. The result is a one-to-one transformation between the global reference frame and the heliostat's local reference frame, misaligned due to manufacturing and installation tolerances.

4.2.1. Model Input Parameters

The model has the following three mechanism-independent input parameters:

1. Solar angle ($\hat{s}$)
2. Heliostat location relative to the tower (A)
3. Aim point (B)

The model's eight mechanism-specific error parameters (E1-8) are briefly discussed below:

E1-2: Pedestal tilt angles (ε_{ptN}) and (ε_{ptE}) describe the heliostat pylon's misalignment relative to the true vertical axis as per Figure 4.4a.

E3-4: Bias angles (γ_{bias}) and (α_{bias}) describe the azimuth- and elevation axes' reference offsets relative to true north and true horizontal, respectively.

E5: Non-orthogonality angle (ε_{NO}) describes the secondary axis' orientation relative to its ideal orientation orthogonal to the primary axis as per Figure 4.4b.

E6-8: Translations (Δ_Z), (Δ_E) and (Δ_N) describe the heliostat's location offset away from its nominal coordinates in the upward-, eastward-, and northward directions, respectively.

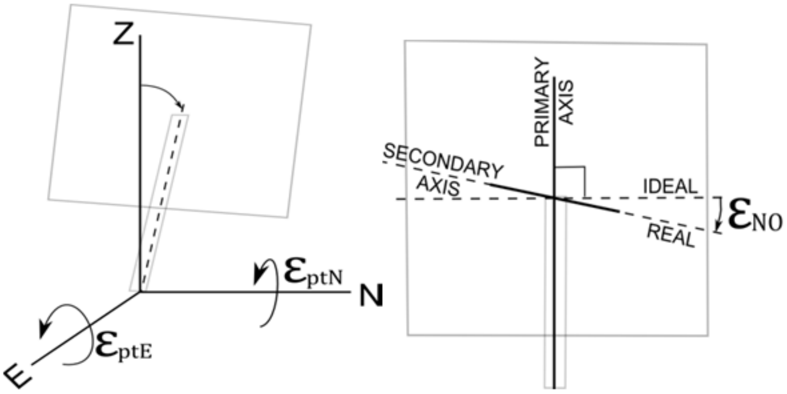

Figure 4.4: a) Pedestal tilt (left) and b) non-orthogonal drive axes (right).

4.2.2. Model derivation

To simplify notation, the derivation is done for only a single heliostat and a single solar unit vector ($\hat{s}$), thus yielding a single two dimensional coordinate of the reflected image relative to the calibration target plane's centre. In practice, the model would be run for every heliostat in the array and during each run, all steps are computed for n input solar vectors ($\hat{s}_{1..n}$). Figure 4.5 shows a diagrammatic representation of the model derivation steps.

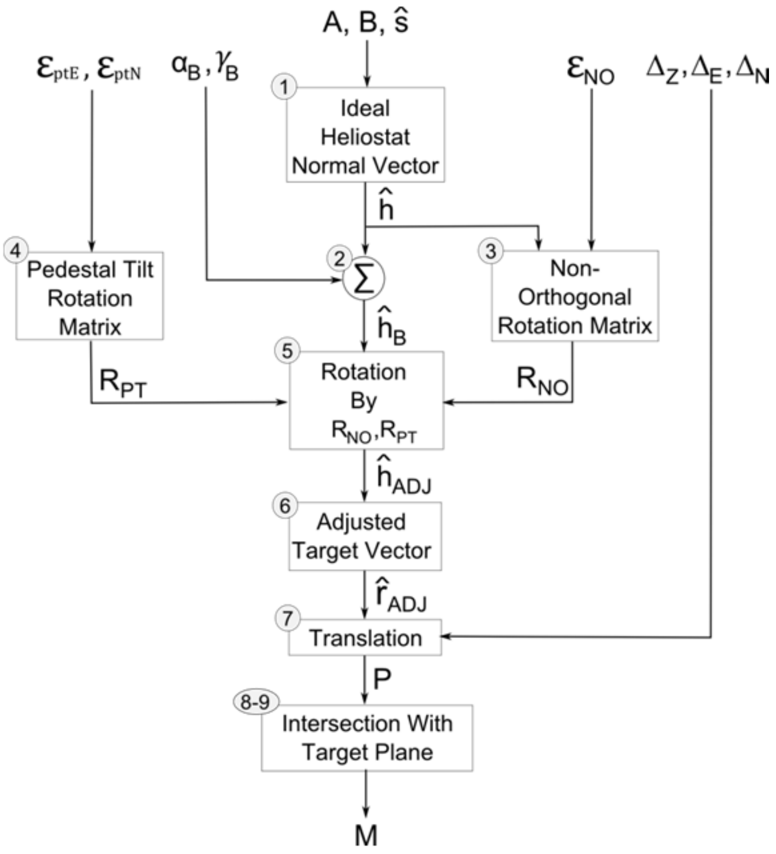

Figure 4.5: Error model derivation steps.

The model is described below in nine steps. Appendix G contains the complete MATLAB® error model code.

1. The ideal heliostat normal vector ($\hat{h}_i$) is calculated as a function of its aim point (*A*), location (*B*) and the solar unit vector ($\hat{s}$). The input solar vector is calculated using Grena's algorithm (§2.1.2) with the timestamp of the specific error measurement. The ideal heliostat normal vector derivation was shown in (4.1 – 4.6) and yielded

$$\hat{h}_i = \frac{\hat{r}_i + \hat{s}_i}{2\cos(\theta_i)}$$

2. The azimuth- and elevation angle offsets are added to the angle components of $\hat{h}_i$:

$$\alpha_{\mathrm{hb}} = \alpha_{\mathrm{h}} + \alpha_{\mathrm{b}} \tag{4.12}$$

$$\gamma_{\mathrm{hb}} = \gamma_{\mathrm{h}} + \gamma_{\mathrm{b}} \tag{4.13}$$

The bias-adjusted heliostat normal vector ($\hat{h}_B$) is found by

$$\hat{h}_B = \left[\sin(\alpha_{\mathrm{hb}}) \quad \cos(\alpha_{\mathrm{hb}})\sin(\gamma_{\mathrm{hb}}) \quad \cos(\alpha_{\mathrm{hb}})\cos(\gamma_{\mathrm{hb}})\right] \tag{4.14}$$

3. Drive axes non-orthogonality is accounted for by rotating the heliostat normal vector around an Euler vector, found by projecting the current heliostat normal vector onto the horizontal plane. The equivalent rotation matrix is found using the Rodrigues rotation formula as follows:

$$R_{NO} = \mathrm{I}_3 \cos(\varepsilon_{\mathrm{NO}}) + (1 - \cos(\varepsilon_{\mathrm{NO}}))[\hat{e}]_{\mathrm{X}} [\hat{e}]_{\mathrm{X}}^{T} + [\hat{e}]_{\mathrm{X}} \sin(\varepsilon_{\mathrm{NO}}) \tag{4.15}$$

with

$$\hat{e} = \left[0 \quad \sin(\gamma_{\mathrm{hb}}) \quad \cos(\gamma_{\mathrm{hb}})\right]$$

4. Pedestal tilt is represented by a compound rotation:

$$R_{PT} = \varepsilon_{ptN}\, \varepsilon_{ptE}$$

$$= \begin{bmatrix} \cos(\varepsilon_{ptN}) & \sin(\varepsilon_{ptN}) & 0 \\ -\sin(\varepsilon_{ptN}) & \cos(\varepsilon_{ptN}) & 0 \\ 0 & 0 & 1 \end{bmatrix} \begin{bmatrix} \cos(\varepsilon_{ptE}) & 0 & -\sin(\varepsilon_{ptE}) \\ 0 & 1 & 0 \\ \sin(\varepsilon_{ptE}) & 0 & \cos(\varepsilon_{ptE}) \end{bmatrix} \tag{4.17}$$

5. The bias adjusted heliostat normal vector ($\hat{h}_{BA}$) found in step 2 is rotated (minding the order of rotations) to account for non-orthogonal axes and pedestal tilt, as follows:

$$\hat{h}_{ADJ} = \mathrm{R}_{\mathrm{PT}}\, \mathrm{R}_{\mathrm{NO}}\, \hat{h}_B \tag{4.18}$$

6. The ideal heliostat normal vector of step 1 is replaced by the adjusted heliostat normal vector ($\hat{h}_{ADJ}$) to yield the corresponding incident angle set

$$\theta_{ADJ} = \cos^{-1}(\hat{s} \cdot \hat{h}_{ADJ}) \tag{4.19}$$

from which the adjusted heliostat-to-target vector ($\hat{r}_{ADJ}$) is calculated:

$$\hat{r}_{ADJ} = \hat{h}_{ADJ} \,.\, 2\cos(\theta_{ADJ}) - \hat{s} \tag{4.20}$$

7. The nominal heliostat location (B) is translated by T{Δ_z, Δ_e, Δ_n} to yield B_{real}.

 This allows for the reflected image position (P) to be found by:

$$P = \begin{bmatrix} B_z & & \Delta_z \\ B_e & + & \Delta_e \\ B_n & & \Delta_n \end{bmatrix} + \hat{r}_{B,NO,PT} \tag{4.21}$$

8. To find the intersection point (P_{int}) between the reflected beam and target plane, a plane is constructed perpendicular to the heliostat-to-target vector and which passes through the target centre, described by

$$(\widehat{N} = A - B) \tag{4.22}$$

$$d = -\widehat{N} \cdot A \tag{4.23}$$

$$u = \frac{(N \cdot B_{real}) + d}{N \cdot (B_{real} - P)} \tag{4.24}$$

$$P_{int,1..n} = +u.(P - B_{real}) \tag{4.25}$$

9. The intersection point (P_{int}) is translated to lie around the origin by

$$P'_{int} = P_{int} - A$$

 and rotated to lie on the vertical East-West plane by

$$P'_{VertEW} = \begin{bmatrix} \cos\theta & 0 & -\sin\theta \\ 0 & 1 & 0 \\ \sin\theta & 0 & \cos\theta \end{bmatrix} \begin{bmatrix} 1 & 0 & 0 \\ 0 & \cos\phi & \sin\phi \\ 0 & -\sin\phi & \cos\phi \end{bmatrix} P'_{int,1..n} \tag{4.26}$$

 with

$$\theta = \tan^{-1}\left(\frac{-N_Z}{\sqrt{{N_E}^2 + {N_N}^2}}\right) \text{ and } \phi = \tan^{-1}\left(\frac{N_E}{N_N}\right)$$

The translated and rotated intersection point (P'_{VertEW}) yields the modelled horizontal- and vertical image offset components:

$$[M_x \quad M_y] = [P'_{VertEW,E} \quad P'_{VertEW,Z}] \tag{4.27}$$

When a set of solar angles are run through the model, a set of corresponding image offsets are produced which indicate a heliostat's tracking error progression as would typically be measured over the course of a day. The next section plots a collection of daily and inter-seasonal error progression sets.

4.3. Modelled Tracking Errors

The effects of various error parameters on heliostat tracking performance were modelled and are shown here. Pedestal tilt, axes biasing, non-orthogonal axes and location uncertainty are shown individually and the effect of inter-seasonal solar angle progression is shown for a fixed combination of error sources.

Since heliostat location (relative to the tower) affects tracking offsets, each error parameter's effects are modelled for a South-field heliostat with *Z,E,N* coordinates (1, 0, -50) as well as for the location of the prototype heliostat for which tracking results are presented in Chapter 6 with coordinates (1, 30.8, -19.2) [m]. The calibration target height is 13 metres in all cases.

Pedestal tilt

Tracking errors for four directions of pedestal tilt are shown for a heliostat located south of the tower (Fig 4.6 left) and southeast of the tower, similar to the prototype system orientation (Fig 4.6 right).

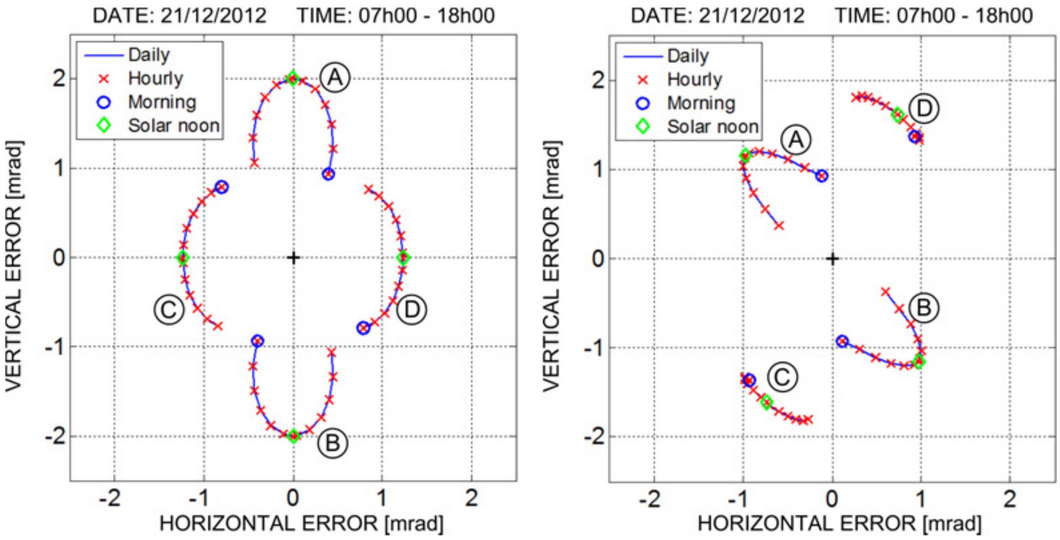

Figure 4.6: Tracking errors for 1mrad pedestal tilt toward North(A), South(B), West(C), East(D) for south-field heliostat (left) and southeast-field heliostat (right).

Bias angle offsets

Tracking errors for four different constant bias angle offsets are shown for a heliostat located south of the tower (Fig 4.7 left) and southeast of the tower, similar to the prototype system orientation (Fig 4.7 right).

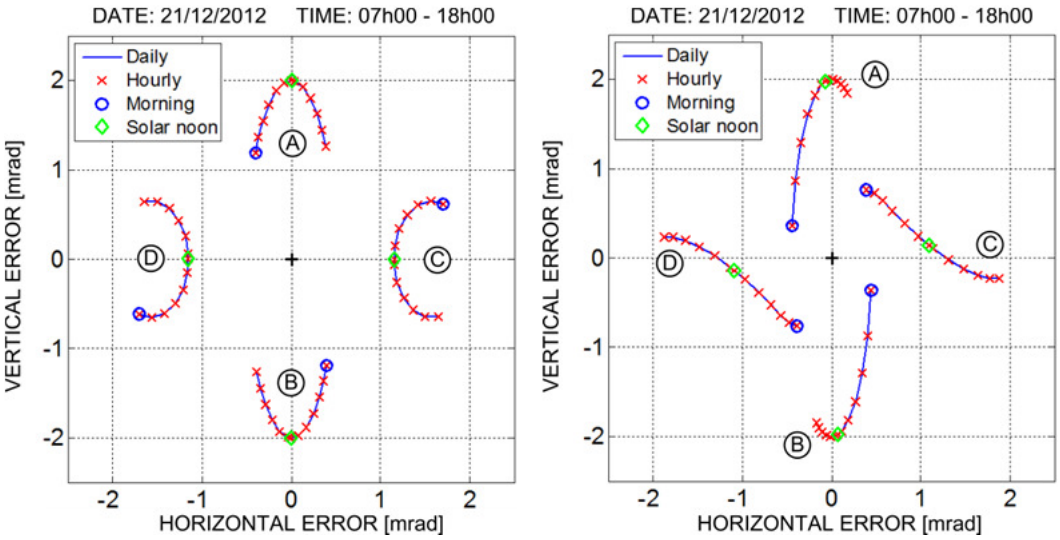

Figure 4.7: Tracking errors for bias offset angles. South heliostat (left); South east heliostat (right). (A): α_{bias} = 1 mrad, (B): α_{bias} = -1 mrad, (C): γ_{bias} = 1 mrad, (D): γ_{bias} = -1 mrad.

Non-orthogonal drive axes

Figure 4.8 shows the effects of non-orthogonal axes for a heliostat located South of the tower (left) and for the prototype heliostat located Southeast of the tower (right).

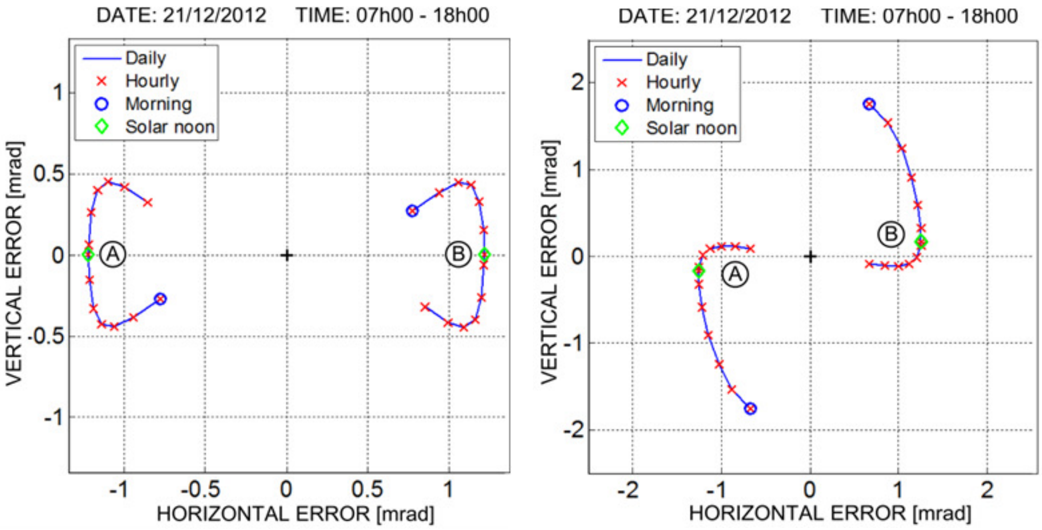

Figure 4.8: Tracking errors for Non-orthogonal axes [mrad]. (A): ε_{NO} = -1, (B): ε_{NO} = 1.

Inter-seasonal variation in tracking error offsets

Finally, figure 4.9 shows the inter-seasonal variation in tracking error offsets of a heliostat located southeast of the tower for a fixed set of error parameters.

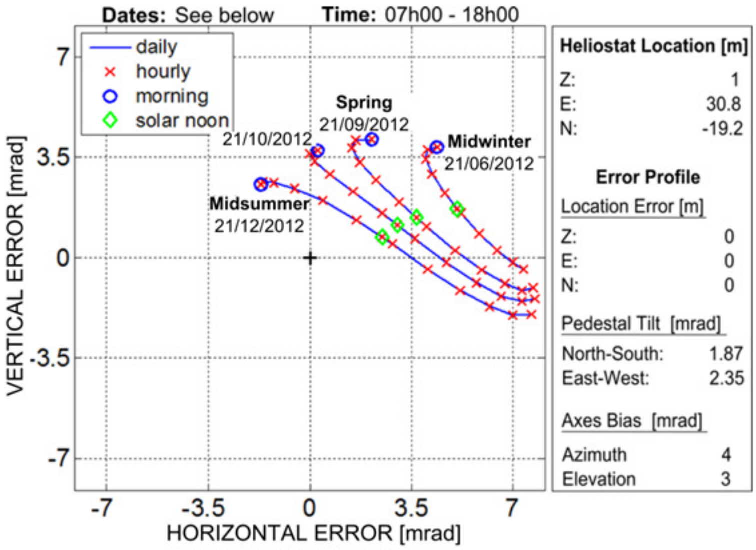

Figure 4.9: Inter-seasonal variation in tracking errors for a fixed set of error parameters.

4.4. Model Validation

During development of the error model, its various steps were each tested individually. This section discusses the preliminary validation of the complete model. First, a qualitative validation was performed by modelling four of the error scenarios described in Stone & Jones (1999). For each scenario, the tracking offsets ($\overline{M}$) generated by the model derived here closely matched the published results in shape as well as in the calculated daily RMS error value. Appendix A contains these results.

A second validation was performed by investigating the effect of random measurement noise on the model's stability. The method used can be divided into four steps (as illustrated by Figure 4.10) as follows:

1. Various sets of known error parameters ($X_{8,known}$) were chosen as test cases. In each case, the model derived in §4.2 was used to calculate a set of error offsets ($\overline{M}$). For each case, increasing levels of random offsets ($\overline{n}$) were added to $\overline{M}$ to simulate measurement noise occurring in a real-world system. For fair comparison between different test cases, ($\overline{n}$) was normalized as follows:

$$\overline{n} = n_{norm} \, M_{RMS} \, \overline{r} \tag{4.28}$$

with n_{norm} a scalar constant for each noise level, M_{RMS} the RMS value of $\overline{M}$ and $\overline{r}$ a set of random values having a uniform distribution between -1 and 1.

2. A mathematical optimization procedure (as per §5.6.4) was used to estimate model parameters $(X_{8,e})$ from the noise affected modelled tracking offsets $(\overline{M_n})$.
3. Discrepancies between the ideal modelled offsets $(\overline{M})$ produced by the known error parameters $(X_{8,known})$ and the noise-affected parameter estimated offsets $(\overline{M_e})$ were quantified by calculating the normalized RMS error value (E_{RMS}) of the difference between $(\overline{M})$ and $(\overline{M_e})$ for each test case.
4. For each test case, a second input solar angle set $(\overline{s_2})$ was used to show the effect of seasonal variation on the model's ability to estimate error offsets. Specifically, $\overline{s_1}$ represents summer solstice and $\overline{s_2}$ represents winter solstice.

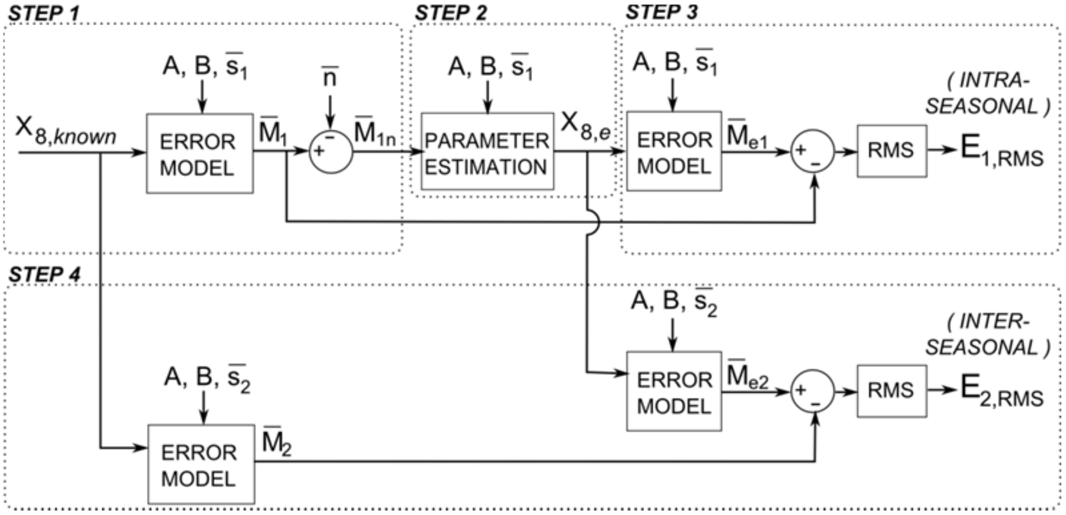

Figure 4.10: Diagram of second validation method.

Figure 4.11 shows the effect of noise on the normalized RMS error in a typical test case for 100 simulations (each with newly generated $\overline{n}$ sets) of $E_{1,RMS}$ and $E_{2,RMS}$. The mean values and 1σ confidence intervals (Freedman *et al.* 2007:67) are shown for normalized noise coefficients (n_{norm}) between 0 and 1.

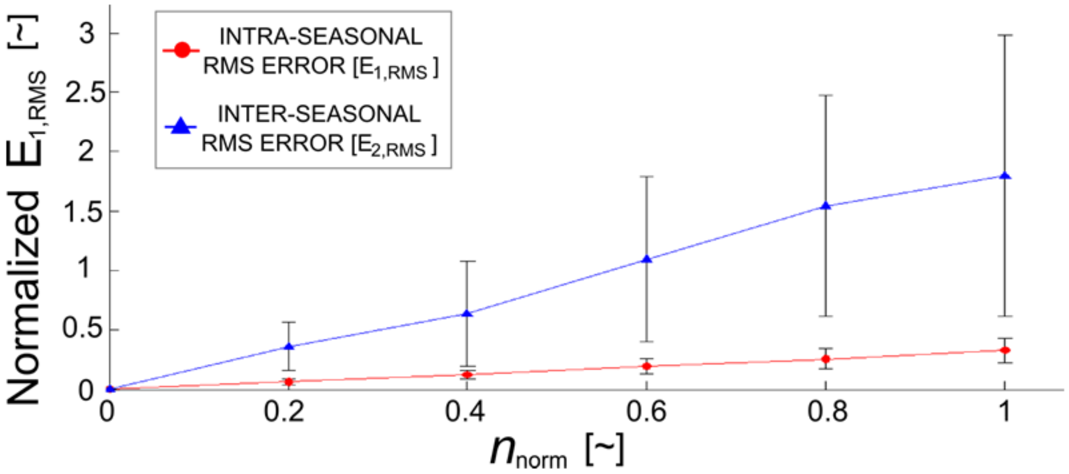

Figure 4.11: The effect of noise on the model's parameter estimation error.

The model performed well with no noise added to the modelled error offsets. The introduction of measurement noise sees both the mean values and the 1σ confidence intervals of RMS errors increase for 100 simulations of fresh noise sets. On average, the effect of noise on E_{RMS} for this set of simulations was approximately four times worse for inter-seasonal error prediction than for intra-seasonal prediction. This general trend corresponds with the findings of Zhang *et al.* (2012) in which the error parameter estimation uncertainty of the heliostat model of Khalsa *et al.* (2011) was investigated.

4.5. Conclusion

The heliostat error model derived in §4.2 uses eight error parameters to account for four deterministic sources of tracking errors. Many more sources of tracking errors may exist, some of which are deterministic (like drivetrain errors, as per §6.4) while others are non-deterministic (like measurement noise, wind loads and backlash). It is therefore likely that some tracking errors will remain after implementing error correction based on the model derived here. The final performance will be gauged when the prototype system's tracking results are presented and discussed in Chapter 6. The prototype system itself is discussed next in Chapter 5.

CHAPTER 5

Prototype System

This chapter describes the heliostat field prototype system that was built to validate the control method and high level architecture of Chapter 3. The intention from the outset was for the prototype to function as a scaled down subsection of the heliostat field for a proposed 5 MW_e central receiver system (CRS) pilot plant.

PART A: MECHANICAL DESIGN

This first part of the chapter describes the heliostat mechanisms and mounting frames. Since the project focused on control systems an in depth analysis of mechanical stresses and structural stiffness fell outside the scope. Instead, a non optimal 'overkill' approach was used to limit structural bending. A part research, part heuristic approach was used to limit heliostat drivetrain backlash as far as possible.

5.1. Heliostat Mechanism

During the course of this project, two very different heliostat mechanisms were designed, built and tested. The second mechanism underwent a substantial design iteration before a total of 18 heliostats were eventually built and integrated into a centrally controlled heliostat array.

5.1.1. First Generation: Triangular Stretched Membrane

The requirements for this first heliostat was an azimuth-elevation mechanism to support an existing triangular stretched membrane reflector (Gauché *et al.*, 2011). Sufficient angular resolution was needed to validate the basic open-loop tracking method. Each axis' mechanism was driven by a 200-steps-per-rotation stepper motor via a 50 : 1 worm gear stage to yield a final output axis resolution of 10 000 : 1. The required motor torque ratings were calculated for a gearing efficiency factor of 0.6 with wind loads obtained using Peterka and Derickson (1992). The operating wind speed threshold was chosen as 30km/h and the triangular surface was simplified to a square with the same surface area.

This heliostat successfully demonstrated simple open loop tracking. It validated the chosen method of calculating the required normal vector (as per §4.1.2) and the use of a solar algorithm (Grena, 2004) to calculate solar angles. However, it exhibited considerable wind deflection even at low wind speeds. The lack of stiffness and heavy mirror frame also caused significant gravity sag. A better design was clearly required for the deployment of multiple heliostats to function as a scaled down subsection of the large field array, as per the project objectives. Figure 5.1 shows a front- and rear view of the first generation triangular stretched membrane heliostat.

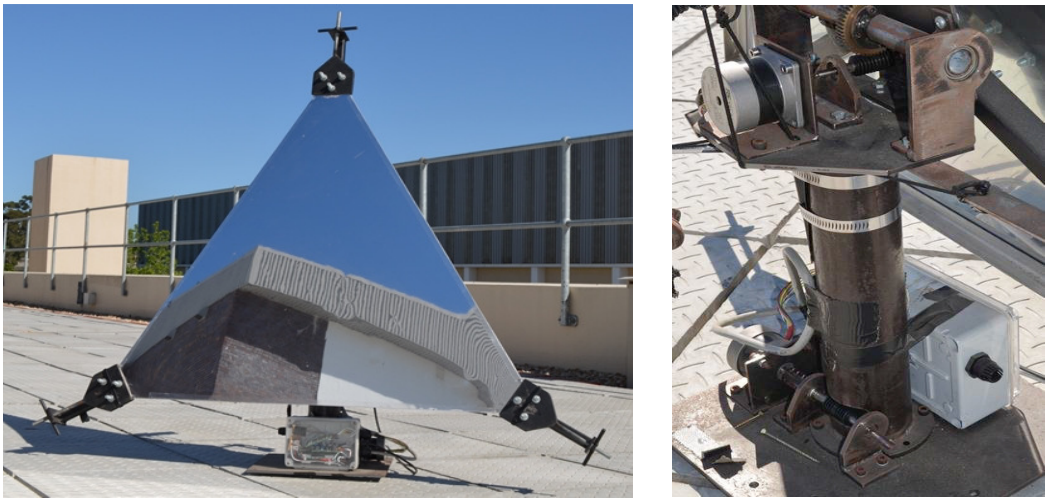

Figure 5.1: Triangular heliostat front view (left) and rear view of the mechanism (right).

5.1.2. Second Generation: 1 ft^2 Glass Mirror Facet

The goal for this mechanism was to experimentally test the real world tracking accuracy obtainable by combining open loop tracking with the model-based error correction strategy described in Chapter 3. The design retained the previous mechanism's azimuth-elevation axis configuration, but differed from the triangular heliostat in the following key areas:

- A small flat glass mirror (0.3 m x 0.3 m) was used as the reflector. This avoided the large mass and high wind loads associated with larger heliostats, thereby drastically reducing structural complexity.
- Each drivetrain consisted of a 30 : 1 worm gear stage, coupled to a 200 steps-per-revolution stepper motor which was driven using 1/8th step microstepping (Eriksson, 1998) to achieve a combined output resolution of 1 : 48 000. This translates to approximately 0.13 milliradian per step, almost eight times the required tracking accuracy.
- The housing was made entirely of laser cut and bent sheet steel plates which provided both the support structure and weather proofing for the drivetrains.
- Unlike the triangular heliostat which used ball bearings, all drivetrain shafts were supported by low cost Teflon bushes. These were held in place by laser cut holes in sheet steel plates to eliminate the need for any machining.
- Bolts were used throughout the mechanism to allow for fine tuning of gear meshing distances and to avoid welding.

5.1.3. Revised Second Generation

After assembly and comprehensive testing of three 2nd generation prototype units, a number of changes were made to fix specific mechanical issues, improve ease of assembly and reduce cost:

- The elevation axis housing was widened to accommodate a larger motor frame size (NEMA 23 instead of the original NEMA 17)[16] to deliver more torque to eliminate step losses due to higher than expected drivetrain friction.
- An improved twin pulley-and-elastic mechanism was added to the inside of the azimuth drive housing to pre-load the azimuth axis to minimize backlash similar to the method used by Brightsource in their Solar Energy Development Centre test facility (SEDC) heliostats.
- Bolt holes drilled and tapped into the sides of housing plates were exchanged for internal attachment plates. This significantly reduced the manufacturing cost of the steel parts and simplified the assembly process.
- The positions and dimensions of various holes and bush plates were adjusted to allow for easier access during final assembly. Assembly instructions for this latest mechanism is included in Appendix G.

Figure 5.2 shows a computer aided design (CAD) rendering of the mechanism with the cover plates and support structures removed to expose the drivetrains of the two movement axes. The assembly drawings and Inventor 2012 CAD model of the final heliostat mechanism are included in Appendices B and G, respectively.

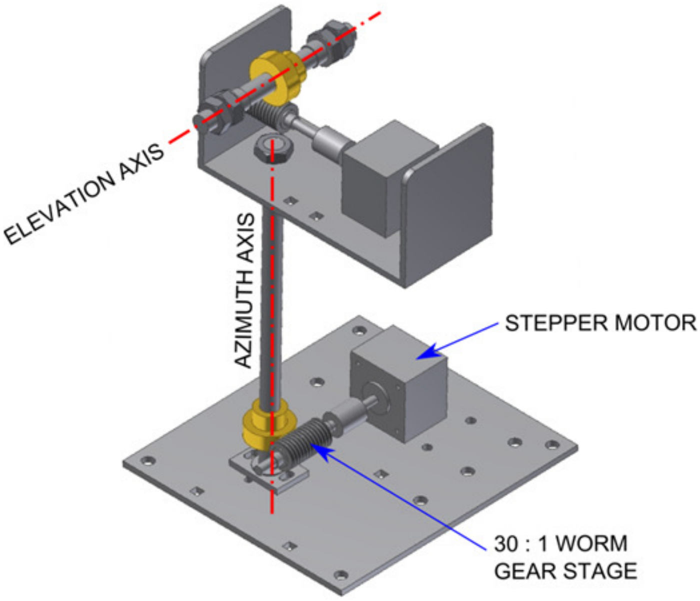

Figure 5.2: The latest heliostat mechanism with its two drivetrains exposed.

---

[16] The National Electrical Manufacturers Association specifies standard electric motor frame sizes.

5.1.4. Heliostat Stepper Motors

During normal operation, heliostats need to adjust their orientation slowly and accurately. Stepper motors are well suited to this type of application because they generate relatively high torque at low speeds and can be accurately controlled in small discreet steps. A comprehensive overview of stepper motor theory can be found in Acarnley (2002).

Each heliostat was driven by a pair of two-phase bipolar stepper motors, one for each tracking axis. Low cost hobby grade motors (Figure 5.3) were chosen for this application and proved to be a good compromise in terms of cost versus performance.

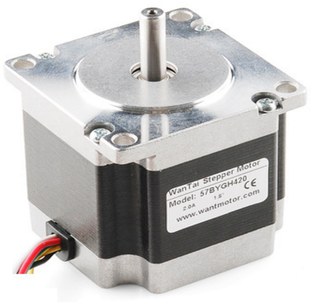

Figure 5.3: Wantai 42BYGHM809 bipolar stepper motor (NEMA 23 frame size).

The design approach was to use oversized motors, driven at well below the rated winding current to limit parasitic losses and to increase service life. Stepper motors are brushless, so their most common point of failure is the rotor bearings (Eriksson, 1998). For this particular application where low duty cycle and low speed is the norm, these motors should last for the entire operational life of a power plant unless environmental exposure or overheating damage occurs.

5.2. Heliostat Mounting Structure

A structure was required to mount heliostats on the solar roof laboratory (which has an uneven sloping flagstone surface) at Stellenbosch University. The main requirements for the mounting structure were stiffness, deployment flexibility, array scalability and ease of access to all heliostats. After considering typical heliostat array layouts, a concept emerged for a triangular mounting structure which could accommodate six heliostats. Figure 5.4 shows a CAD drawing of the prototype 'six pack' heliostat mounting structure.

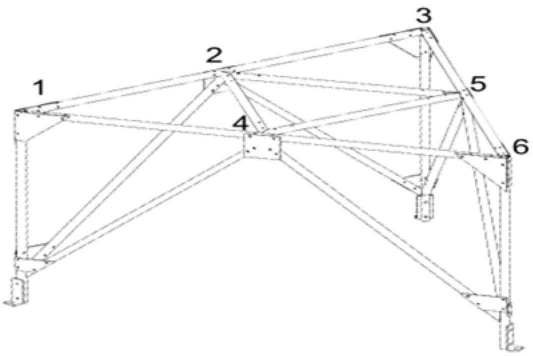

Figure 5.4: Triangular 'six pack' heliostat mounting structure.

The main advantages of this particular layout are:

- Easy levelling of the three-legged pedestal (similar to a camera tripod) allow for simple deployment on non-flat terrain.
- Easy access for maintenance and cleaning since all heliostats are edge-mounted.
- Sharing of ground contact points implies an overall reduction of foundations and anchors required for the field.
- The triangular structure allows for curvature around the receiver while maintaining near uniform spacing, as illustrated in Figure 5.5.

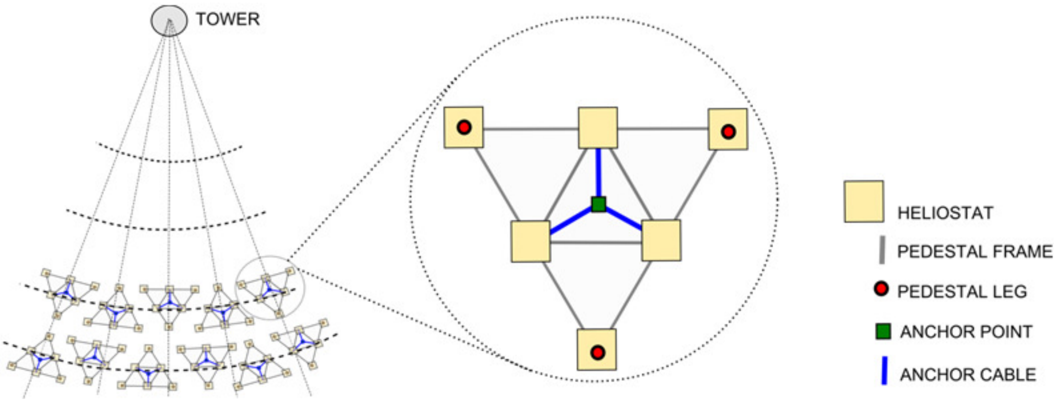

Figure 5.5: A curved heliostat array consisting of triangular mounting structures (plan view).

Further investigation showed this structure to be a novel concept. An international patent application has since been lodged by Stellenbosch University for a generic triangular support structure for six or more heliostats (Malan & Gauche, 2013a).

For the prototype system, three triangular mounting structures were built, each holding six small 'latest generation' heliostats. A photograph of heliostats attached to the triangular mounting structures is shown in Figure 5.6.

Figure 5.6: Heliostats deployed on triangular ‘six-pack’ pedestals.

PART B: CONTROL SYSTEM

This second part of the chapter describes the control system implementation of the prototype heliostat array. To avoid repetition, references will made throughout the remainder of this chapter to concepts described in Chapter 3. The sections that follow are grouped by subsystem components and include the communication network, local controller unit (LCU), cluster controller unit (CCU) and central system controller (CSC). Each subsystem consists of various hardware and software components. The part numbers and datasheets for all hardware components are included in Appendices E and F respectively so explicit references will not be included in each hardware section.

The various software components span three programming languages:

- The embedded processing code running in the local- and cluster controllers were written in the Wiring programming language which in turn is built on the C++ programming language (WiringProject, [S.a.]).
- The image processing routines and the mathematical optimization procedure which estimates coefficients for the error model (described in Chapter 4) were implemented in MATLAB®.
- The central controller’s graphical user interface (GUI) was created using Borland Delphi 7.

5.3. Communication Network

This section describes the network’s physical layer and communication protocol (Kuphaldt, 2007).

5.3.1. Physical Layer

The communication network has a wired star- and bus topology (derived in §3.5.2). Low cost RS485 transceivers were used to link clusters of heliostats to their respective CCU's in a full duplex serial bus topology, as per Figure 5.7.

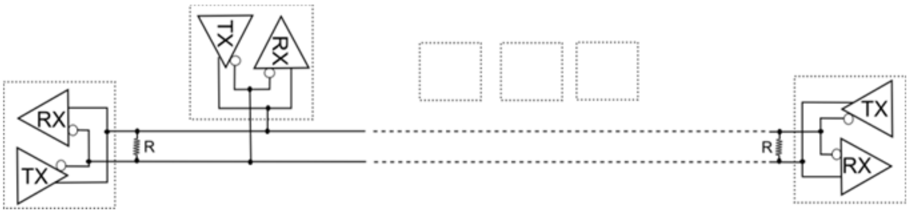

Figure 5.7: Serial bus with RS485 transceivers.

Each transceiver's direction is controlled by the LCU microcontroller. Figure 5.8 shows an RS485 driver board with integrated LCU power buffer and input voltage monitoring circuit (described in §5.4.2). Appendix C contains the electronic schematic of this circuit.

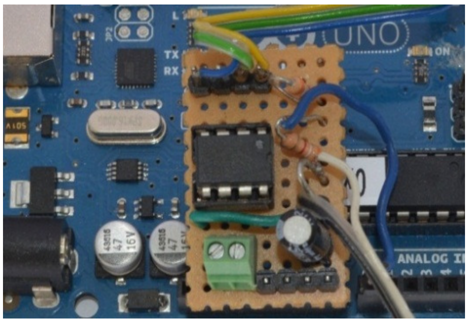

Figure 5.8: A prototype RS485 transceiver board connected to its host LCU microcontroller board.

The same drivers are used in unidirectional mode to effect a full-duplex star topology for connecting the cluster controllers to a serial hub located at the central control PC.

5.3.2 Communication Protocol

Each of the following protocol aspects were discussed in §3.5.

Channel Access Method

A polling strategy is used whereby the cluster controller acts as communication master and all LC nodes act as slaves. Only the master is allowed to initiate transmission onto the channel. When a response is required from a slave node, the master gives permission to that specific node to transmit. The switching of each node's RS485 driver data direction is handled by that node's microcontroller.

Data Packet Structure

All system messages are encapsulated in a custom packet structure based on what was described in §3.5.1 and customised for this system with regards to addressing. Figure 5.9 shows a diagram of the packet structure with single byte node addresses and a single byte cyclic redundancy code (CRC).

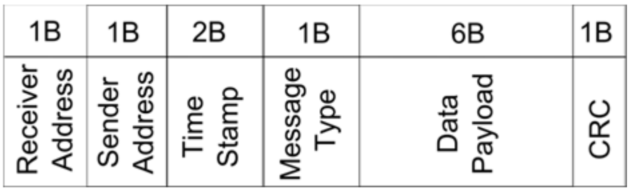

1B	1B	2B	1B	6B	1B
Receiver Address	Sender Address	Time Stamp	Message Type	Data Payload	CRC

Figure 5.9 Twelve byte data packet structure.

Table 5.1 shows the structure of message type 0x01: 'Query Step Counts'. The rest of the custom protocol's 34 message types are described in Appendix D.

Table 5.1: Message structure of 'Query_Step_Counts' message (message type 0x01).

Message Type	Data Payload
0x01: <Q_stepcounts>	Byte 1: Local Controller Address (index for address array stored in the cluster controller). Bytes 2-3: Heliostat azimuth step count [0..65535]. Bytes 4-5: Heliostat elevation step count [0..65535]. Byte 6: Null.

Cyclic redundancy code

The following simple one byte CRC formula was used for all data transmission:

$$b_{CRC} = \left(\sum_{i=1}^{N} b_i \right) \% \ 256 \tag{5.1}$$

where N is the packet length (without CRC), b_i is the packet's i^{th} byte and % is the modulo operator commonly used in computing to yield the integer remainder after division (Pardue, 2005:51).

5.4 Heliostat Local Controller Unit

Each heliostat has a local controller unit (LCU) which handles all its local processing- and motor control tasks. This unit links the heliostat to the rest of the system by interpreting instructions from and sending status information to the cluster controller unit assigned over it.

5.4.1 LCU Hardware

Each LCU contains a microcontroller, RS485 transceiver, power buffer circuitry and motor driver modules. A block diagram of LCU components are shown in Figure 5.10.

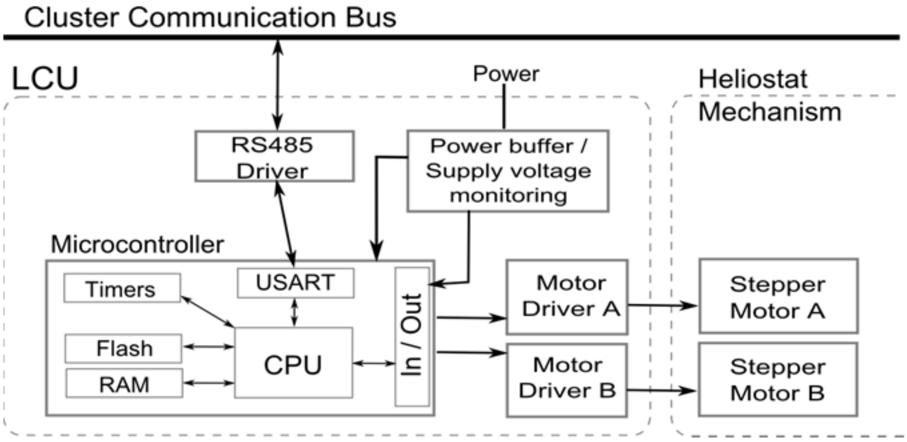

Figure 5.10: Local controller unit components.

Microcontroller

An Arduino Uno R3 microcontroller board (shown in Figure 5.11) forms the 'brain' of each LCU. The microcontroller interacts with the cluster communication bus and performs all of the heliostat's local processing tasks, as will be described in §5.4.2.

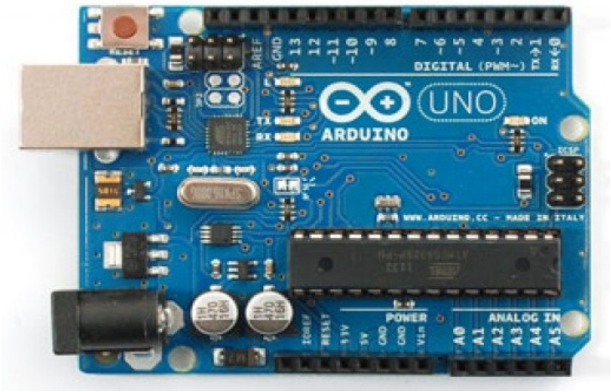

Figure 5.11: Arduino Uno R3 microcontroller board.

The Arduino board is built around the Atmel ATmega328 microcontroller. Its specifications (relevant to the LCU requirements) can be summarized as follows:

- Processor: 8-bit architecture, 16 MHz clock speed
- Memory: 32 KB Flash, 1KB SRAM, 512B EEPROM
- Peripherals: 1 × USART, 14 × digital I/O pins, 3 × Hardware timers

Motor Drivers

Every stepper motor needs a driver module to control the magnitude and direction of current flowing in each of its windings. Eriksson (1998) provides an excellent overview of stepper motor operation. In keeping with the principle of using low cost off the shelf hardware components, Big Easy Driver modules were used for this purpose (Figure 5.12).

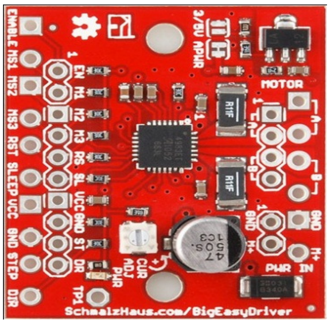

Figure 5.12: Big Easy Driver motor driver module.

Local shaft angle feedback sensors were avoided while accurate position control was maintained by continuously keeping count of the number and direction of movement steps taken. This strategy resulted in significant cost savings for the prototype system. An important point to consider is that step counting only works if the motor is never allowed to stall. Motor stall was avoided by over-sizing each motor relative to its required load and limiting the motor step rate. For commercial systems where cost optimization is essential, a more sophisticated control method may be needed. Specialized drivers exist which can automatically detect stalling by continuously monitoring the back-electromotive force (EMF) voltage waveforms on the motor windings (Gandolfo & Wendlandt, 2009; Kubisch *et al.,* 2011).

Section 5.1.2 explained the need for micro-stepping to increase the movement resolution of the mechanism's drivetrains. The downside of micro-stepping is that a 100 per cent duty cycle is required to prevent the rotor from reverting to the nearest full step position in between steps. The resulting constant power dissipation caused overheating of the driver modules on hot days. This problem is discussed in §6.2 along with other practical issues that were encountered during installation and testing of the prototype system.

5.4.2 Local Controller Software

Figure 5.13 shows the LCU microcontroller's high level program structure.

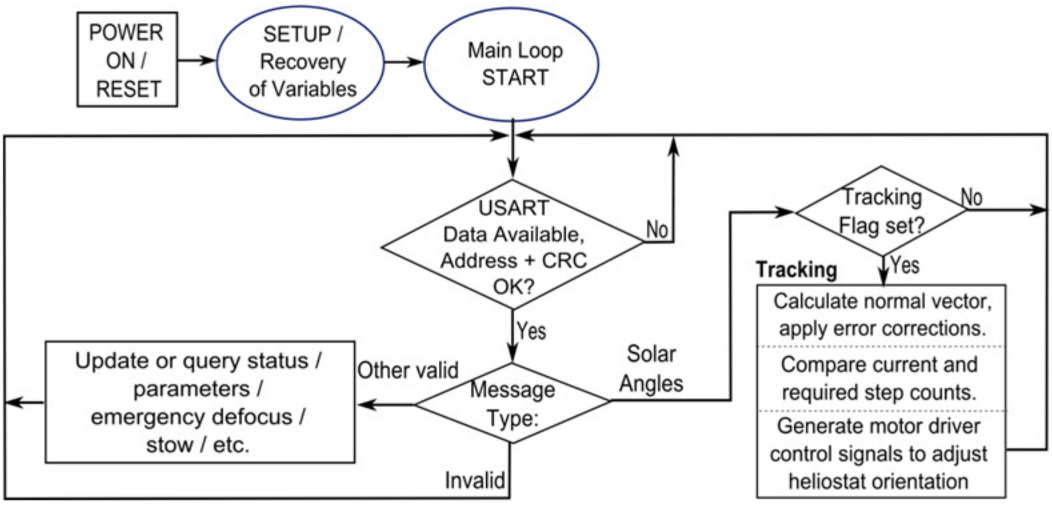

Figure 5.13: Local controller high level program structure.

Setup and Recovery of Variables

Directly after a power on or reset event, the setup procedure initializes the microcontroller's various timers, serial ports (USART), etc. It also loads a number of critical variables from non-volatile memory (EEPROM) to working memory. These variables include the heliostat's location, current aim point, current actuator positions, error model parameters and status flags. If no valid variables exist (an internal consistency check is used), the heliostat waits until valid parameters are received from its cluster controller.

During power down events, all local variables are stored in non-volatile memory for recovery when power is restored. The microcontroller continuously monitors its supply voltage line to detect unplanned power down events and a buffer capacitor keeps the microcontroller powered while critical variables are stored.

Tracking

In tracking mode, the serial port is continuously monitored. Each valid set of incoming solar angles triggers a sequence of events. First, the solar angles are used to calculate the ideal heliostat normal vector based on stored values of the heliostat's location and intended aim point. Then, a number of error corrections are done based on inverse kinematics using heliostat-specific stored error model coefficients. Finally, the required motor positions are calculated and compared with current positions to generate motor control signals for re-orienting the heliostat to its new position.

Watchdog- and Heartbeat Timers

Two timers operate in each LC to ensure safe operation. The first is a watchdog timer which ensures that in case the program code stalls or 'crashes', the timer will overflow, triggering a special interrupt procedure. This procedure stores all important variables in non-volatile memory before resetting the device. On restarting after such an event, the LC's status is reported to its cluster controller for appropriate handling. Secondly, a heartbeat timer gets reset every time a heartbeat message arrives from the cluster controller to confirm the system status. If a communication problem occurs and no heartbeat message is received for a predetermined number of control periods, the local controller enters an emergency state. This causes the heliostat to defocus from the target and eventually to move to a predefined stow position.

5.5 Cluster Controller Unit

This section describes the cluster controller unit's (CCU) hardware components and gives an overview of its embedded program code.

5.5.1 Cluster Controller Hardware

The heliostat field control system's distributed processing strategy (§3.4) requires at least one cluster control processor to be present in every heliostat cluster. Figure 5.14 shows a diagrammatic representation of the CCU layout.

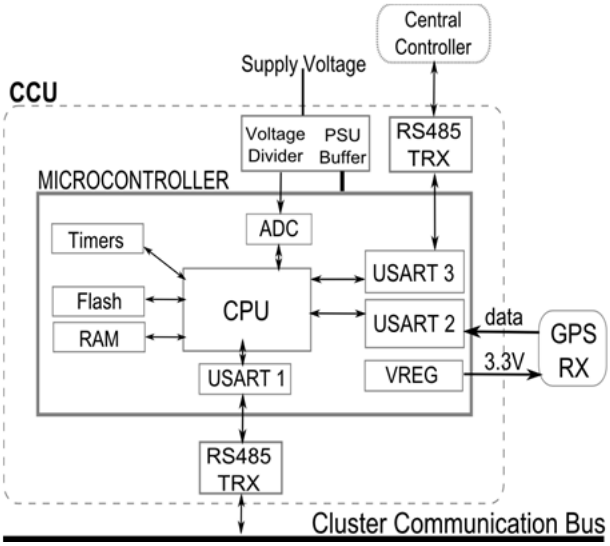

List of abbreviations:

ADC:	Analog to digital converter
CCU:	Cluster controller unit
CPU:	Central processing unit
GPS RX:	Global positioning satellite receiver
RAM:	Random access memory
TRX:	Transceiver
VREG:	Voltage regulator

Figure 5.14: Cluster controller unit (CCU) layout.

CCU Microcontroller

The solar algorithm requires processing of 64-bit floating point variables to minimize the accumulation of rounding errors (Grena, 2007). To work efficiently with these variables requires a microprocessor with least a 32-bit architecture. A wide variety of microprocessors could have been used for this task, but due to off the shelf availability and close code compatibility with the Arduino-based LCUs, the Leaflabs Maple board (Maple, The [S.a.]) was chosen – shown in Figure 5.15.

Figure 5.15: Leaflabs Maple microcontroller board.

The Leaflabs Maple is based on the STM32F103RB microprocessor. Its specifications (relevant to the CCU's requirements) can be summarized as follows (ST Microelectronics, 2011):

Processor:	32-bit ARM Cortex M3, 72MHz clock speed
Memory:	128 KB Flash, 20KB SRAM
Peripherals:	3× USART, 43× I/O pins, 3× 16-bit hardware timers

GPS Receiver

A low cost Ublox LEA-4P GPS receiver module (Figure 5.16) was used to provide time and date information to the cluster controller.

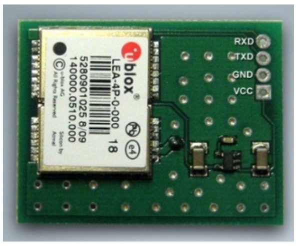

Figure 5.16: GPS receiver module.

GPS time is transmitted once per second as ASCII strings which conform to National Marine Electronics Association (NMEA) Protocol 0183 (Betke, 2001). The module is powered via the Maple board's on-board voltage regulator and is connected directly to the CCU's USART2.

5.5.3 Cluster Controller Software

Each CCU calculates the solar position vector from local time and acts as communications coordinator between the CCU and the heliostat cluster under its control. The cluster controller's high level program structure is shown in Figure 5.17. A comprehensive flow diagram and code listing are contained in Appendices E.1 and F respectively.

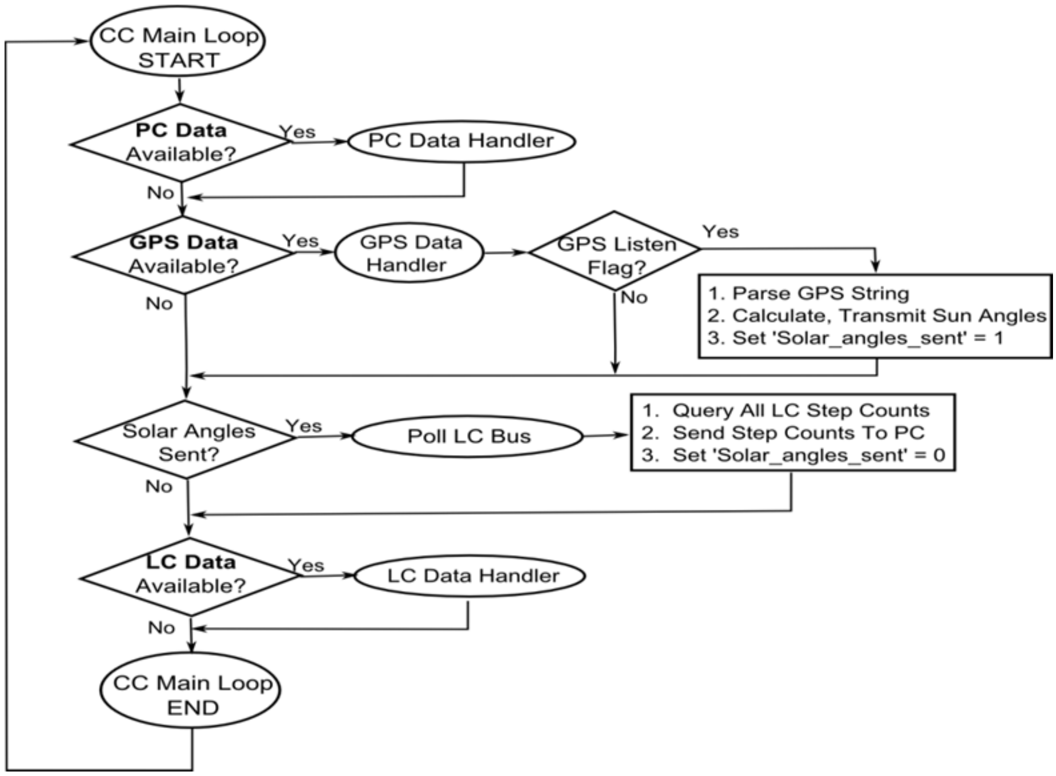

Figure 5.17: Cluster controller high level program structure.

The main program loop continuously monitors three communication channels:

<u>Channel 1: Central controller (PC Data)</u>

The central controller PC sends configuration updates and system queries to the cluster controller unit (CCU) to update or request the system state, individual heliostat parameters, etc. After each tracking control interval, the CCU sends back updates of all heliostats' status and step counts. A dedicated physical channel to each cluster controller allows for full duplex data transmission.

<u>Channel 2: GPS</u>

The GPS receiver transmits NMEA text strings at one second intervals. If the 'GPS_Listen' flag is set (depending on system state), these strings are parsed to extract the current time and date for calculating the sun's angle using a solar position algorithm (§2.1.2).

Channel 3: Local controller bus

The real-time calculated solar position is transmitted from the CCU to all heliostats in the cluster. The CCU then queries every heliostat in the cluster's status and current step counts over this channel.

5.6 Central System Controller

The central system controller (CSC) was implemented on a desktop computer at the top of the control hierarchy. It allows a human operator to monitor and manually override the entire system via a graphical user interface (GUI). It also handles all heliostat field calibration scheduling and processing tasks, most of which can be set up to run automatically.

5.6.1 Functional Overview and Dataflow

The CSC's functional layout is represented by Figure 5.18, with data flow indicated by arrows.

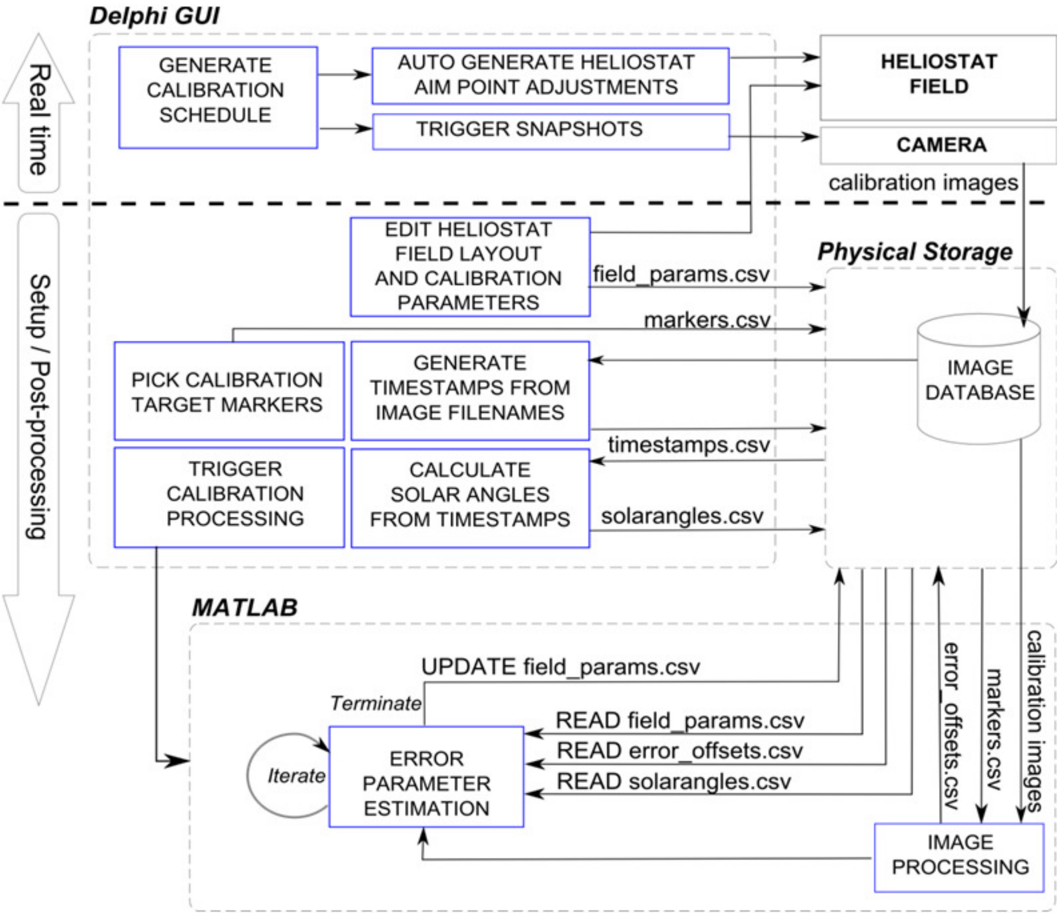

Figure 5.18: Central system controller (CSC) layout and dataflow.

With reference to Figure 5.18, data generated at each step is stored in comma separated value (.csv) text files. These files can be viewed or edited using any standard text editor or imported to spreadsheet software like Microsoft Excel. This format allows for convenient access to the data at various stages for debugging purposes.

The operator can set up a calibration schedule which automatically generates command sequences to periodically direct specific heliostats to aim at the calibration target for image capture by a digital camera. The captured images are labelled by date and timestamp before being stored in an image database on the CSC.

During post-processing of calibration data, typically at the end of a solar day, a file (`timestamps.csv`) is generated which contains the entire day's calibration image timestamps. These are input to a solar algorithm (Grena, 2008) which calculates and stores the corresponding solar angles in `solarangles.csv` – to be used later by the parameter estimation procedure described in §5.6.4.

5.6.2 Graphical User Interface

The graphical user interface (GUI) serves as a control dashboard for the operator. It was developed using Borland Delphi 7. A screenshot of the main window with its various sections outlined in red (grouped by functionality) is shown in Figure 5.19. With reference to the various labelled sections, the operator can:

- A/E: Monitor a range of real-time system information including heliostat motor step counts, GPS time, PC time and current solar angles.
- B: Access time-stamped logs of transmitted and received data packets for debugging purposes.
- C/D: Adjust system states and manually send orientation, tracking lock, motor counts reset and other override commands to any heliostat in the field.
- F: Adjust individual heliostat aim points, target plane orientation and offset vector between the target centre and receiver centre.
- G: Control and adjust the field calibration schedule whereby heliostats are commanded to move between the calibration- and receiver targets. Manually or automatically trigger the network camera to take pictures at appropriate times. Manually pick corner marker points of the first image of a day – for use when performing perspective correction of the captured target images.

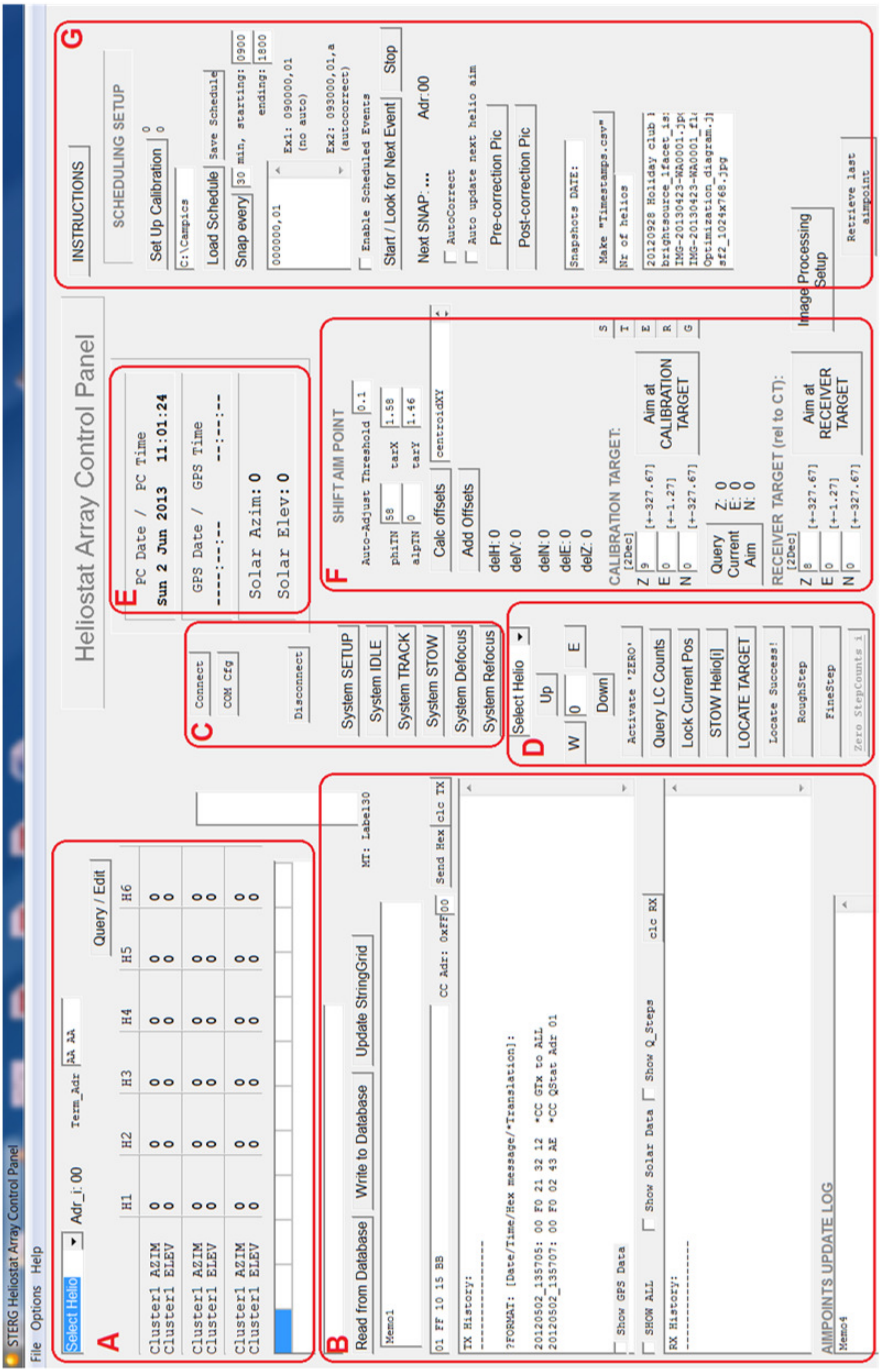

	H1	H2	H3	H4	H5	H6
Cluster1 AZIM	0	0	0	0	0	0
Cluster1 ELEV	0	0	0	0	0	0
Cluster1 AZIM	0	0	0	0	0	0
Cluster1 ELEV	0	0	0	0	0	0
Cluster1 AZIM	0	0	0	0	0	0
Cluster1 ELEV	0	0	0	0	0	0

```
01 FF 10 15 BB
```

```
TX History:
----------------

?FORMAT: [Date/Time/Hex message/*Translation]:

20120502_135705: 00 F0 21 32 12  *CC GTx to ALL
20120502_135707: 00 F0 02 43 AE  *CC QStat Adr 01
```

```
RX History:
----------------
```

```
PC Date /  PC Time
Sun 2 Jun 2013   11:01:24

GPS Date /  GPS Time
----:--:--     --:--:--

Solar Azim: 0
Solar Elev: 0
```

Auto-Adjust Threshold: 0.1

phiTN: 58
alpTN: 0
tarX: 1.58
tarY: 1.46

delH: 0
delV: 0
delN: 0
delE: 0
delZ: 0

CALIBRATION TARGET: [2Dec]
Z: 9 [+-327.67]
E: 0 [+-1.27]
N: 0 [+-327.67]

Z: 0
E: 0
N: 0

RECEIVER TARGET (rel to CT): [2Dec]
Z: 8 [+-327.67]
E: 0 [+-1.27]
N: 0 [+-327.67]

Set Up Calibration: 0 0

C:\Campics

Snap every 30 min, starting: 0900
ending: 1800

```
000000,01
```

Ex1: 090000,01 (no auto)
Ex2: 093000,01,a (autocorrect)

☐ Enable Scheduled Events

Next SNAP: ... Adr: 00

☐ AutoCorrect
☐ Auto update next helio aim

Snapshots DATE:

Nr of helios

```
20120928 Holiday club i
brightsource_1facet_is:
IMG-20130423-WA0001.jp
IMG-20130423-WA0001_fl
Optimization_diagram.j
sf2_1024x768.jpg
```

Figure 5.19: Central System Controller graphical user interface (GUI).

5.6.3 Image Processing

During the calibration process, a set of time-separated digital photographs are taken of each heliostat's solar image projected onto a calibration target located below the receiver. The optical target was simply a flat white rectangular surface with well defined black reference markers at known coordinates near the corners. Figure 5.20 represents image processing steps that were used to extract image centroid coordinates from the calibration target photographs.

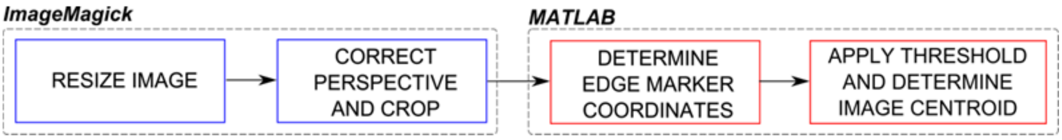

Figure 5.20: Image processing steps for extracting tracking error offset coordinates.

The first two steps were performed using ImageMagick®, an open source command line based image editing software package; the last two were implemented with an executable function written in MATLAB®.

Resizing, perspective correction and cropping

A simple ImageMagick® command was used to resize the original digital images to 375 by 300 pixels (px) to make it more manageable for processing in MATLAB®. The calibration target was 2 m high, so 300 translates to a minimum resolution of 6.67 mm / px. Next, perspective correction had to be performed since the camera was located away from the normal vector of the optical target plane. Figure 5.21 shows an example image before and after applying perspective correction, cropping and a small amount of contrast adjustment.

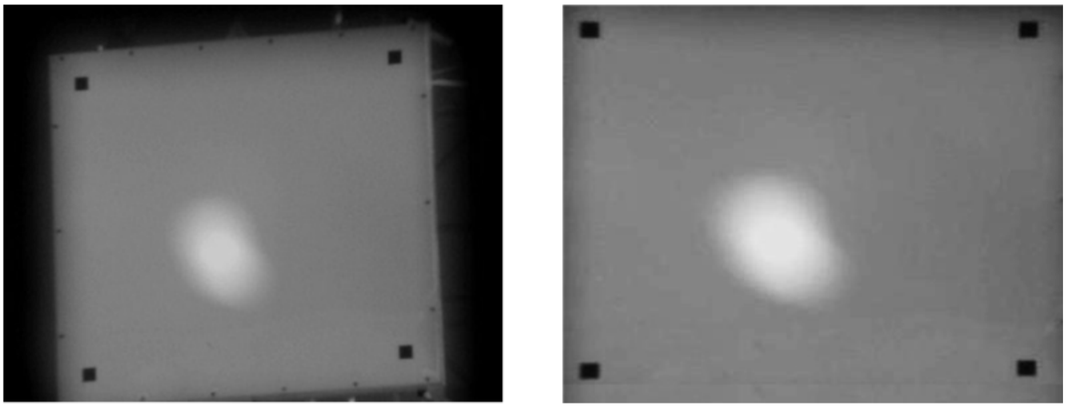

Figure 5.21: Example image of the calibration target before (left) and after (right) perspective correction, cropping and contrast adjustment.

Finding reference marker coordinates

Each image was converted to black and white, with threshold (T_{BW1}) determined by

$$T_{BW1} = P_D + 0.2P_L \tag{5.2}$$

where P_D and P_L are the image's darkest and lightest pixel values, respectively. This typically yielded a result similar to that shown in figure 5.22 (left) to isolate the black markers. The coordinates of the top left and bottom right markers' inside corners (red cross markers) were then found by evaluating the entire array of pixels to find the black pixels located closest to predetermined points 50 pixels away from the image's sides (blue circle markers).

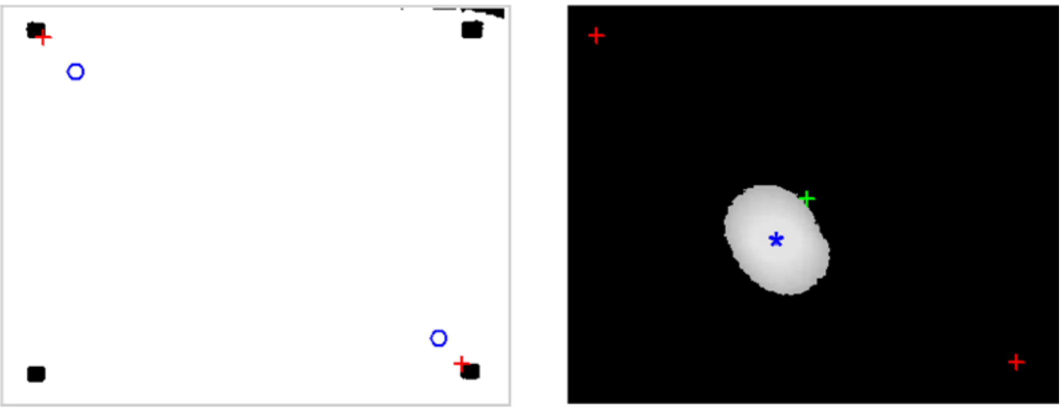

Figure 5.22: Finding reference marker coordinates (left); finding the heliostat image centroid (right).

Image centroid calculation

The image from Figure 5.20 (right) was converted to that of Figure 5.21 (right) by converting to black all pixels with brightness values below a threshold (T_{BW2}), calculated as follows:

$$T_{BW2} = \frac{P_{AVG} + P_L}{2} \tag{5.3}$$

where P_{AVG} and P_L are the image's average and lowest pixel brightness levels, respectively.

The reflected image centroid ($[C_x \quad C_y]$) was calculated by treating the problem as a center of mass calculation in two dimensions (Ruina and Pratrap, 2002:276) with each pixel representing a square element with mass equivalent to its brightness:

$$C_x = \frac{\sum x_i b_i}{b_{tot}} \quad \text{and} \quad C_y = \frac{\sum y_i b_i}{b_{tot}} \tag{5.4}$$

where b_i is the pixel intensity at position *i* along the relevant image axis and b_{tot} is the sum of all pixel brightness values.

5.6.4 Estimation of Heliostat Error Parameters

Mathematical optimization was used to estimate error model parameters which best fit a set of tracking offsets (obtained from calibration target measurements) for each heliostat. Both the error model (Chapter 4) and the optimization procedure was implemented in MATLAB®. The complete code is included in Appendix G. Figure 5.23 shows a diagram of the process.

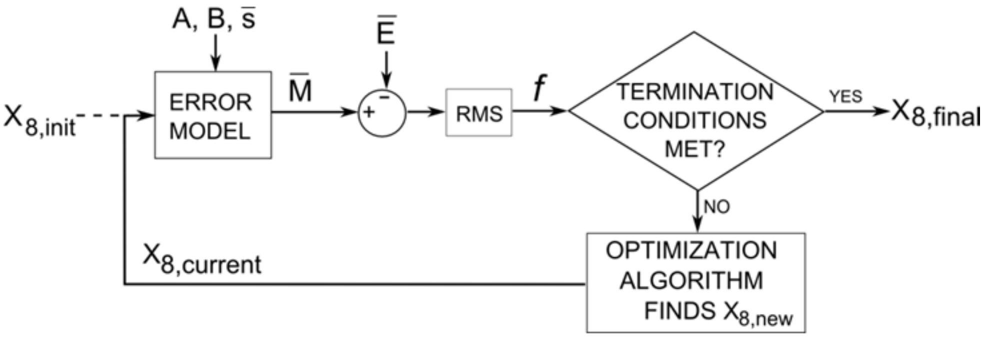

Figure 5.23: Estimation of error model coefficients by mathematical optimization.

The optimization procedure inputs the heliostat's location (*B*), aim point (*A*), current set of model coefficients ($X_{8,current}$) and a set of solar vectors ($\bar{s}$) corresponding to timestamps from measured tracking offsets ($\bar{E}$). The error model (derived in Chapter 4) produces a modelled set of error offsets ($\bar{M}$). The objective function (f) to be minimized is expressed as the root mean square (RMS) error between the measured error set and the model predicted error set:

$$f = \sqrt{\frac{1}{n}\sum_{i=1}^{n}(M_i - E_i)^2} \tag{5.5}$$

After each iteration, the set of error coefficients is updated by an optimization algorithm. The entire procedure repeats until certain termination conditions are met. In this case, the conditions were met after a predetermined number of iterations or when the objective function became sufficiently small.

The choice of optimization algorithm is critical to the success of the system. At first, a custom implementation of the Particle Swarm Algorithm (Rao, 2009) was attempted. This was later abandoned in favour of an unconstrained nonlinear minimization algorithm which forms part of MATLAB®'s Optimization Toolbox (`fminsearch`) and which uses the Nelder-Mead Simplex method.

5.7 Power Supply and Wiring

The system's power supply and network wiring configuration was kept as simple as possible. Two DC lines (24 V and 9 V) were run to all the heliostat local controllers. The 24 V line supplied power to the motor controllers while 9 V supplied each Arduino. An on-board regulator on each Arduino provided 5 V for the microcontroller and to power each LCU's local RS485 driver. All network communication was achieved using two-wire RS485 serial transceivers, so a serial two-wire cable was connected between each CCU and its cluster of heliostats.

5.8 Conclusion

A prototype heliostat array was successfully implemented to validate the method described in Chapter 3. Initial validation of individual subsystems and components were completed as part of each development phase.

Next, Chapter 6 will present and discuss results obtained with the integrated prototype system.

CHAPTER 6

Results

As part of this study, tests were performed using the prototype system described in Chapter 5 to measure individual heliostat tracking accuracy and to evaluate overall system functionality. This chapter describes the experimental setup and some practical considerations before presenting and discussing operational results.

6.1 Experimental Setup

The heliostat array prototype system described in Chapter 5 was assembled and deployed on the solar roof laboratory at the Department of Mechanical and Mechatronic Engineering at Stellenbosch University. Figure 6.1 shows a plan view of the laboratory housing the experimental setup.

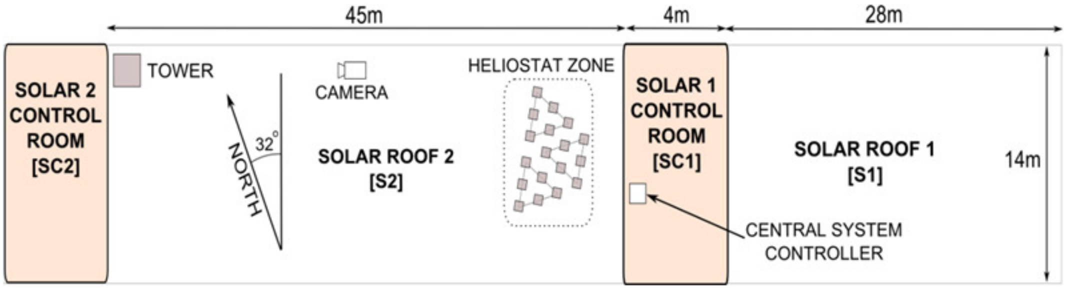

Figure 6.1: Plan view of the solar roof laboratory.

Calibration measurements and validation of tracking accuracy was done using two 4 m^2 optical targets and a stationary digital camera. The targets were mounted on an 18 m high lattice tower located in the north-western corner of Solar Roof 2. The slant range from the topmost optical target to the centre of the heliostat zone was approximately 40 m. The orientation of the roof and availability of free space dictated that all heliostats be deployed in an area located southeast of the tower.

6.2 Practical Challenges and Solutions

A number of problems were encountered during the course of building, integrating and testing the prototype system. This section briefly covers some of these problems and their solutions in the hope that future researchers may learn from this.

Lens flare

When non-image forming light enters a camera lens and reflects off internal surfaces, bright spots and loss of contrast may occur on the intended image (as per Figure 6.2). This happened to the camera at times when the solar vector was nearly in line with the camera-to-calibration target vector, thus appearing in or near the edge of the image frame. The resulting artifacts and loss of contrast threw off the image processing sequence and caused inaccurate calculation of the actual image centroid

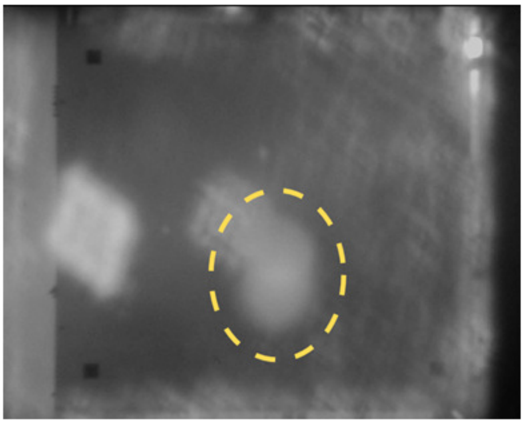

Figure 6.2: Lens flare in a calibration image. The yellow ellipse shows the actual heliostat image.

Lens flare was largely eliminated by adding a shading plate with a carefully aligned rectangular slot in front of the camera lens to block non-image forming light.

Loss of volatile memory during power failures

At times when the system inadvertently lost power, the heliostat local controllers units (LCUs) lost their current motor step counts. These heliostats then needed to be recalibrated. This issue was solved by adding a power buffer capacitor and input voltage monitoring circuit (schematic shown in Appendix C) to allow enough time for a power failure to be detected and handled before shutting down. At detecting a dip in the input voltage, the LCU would immediately stop all tasks and store the current step counts to non-volatile memory (EEPROM[17]). When power was restored, the LCU would retrieve the last step counts from memory as part of its normal startup procedure.

Overheating of motor driver modules

Stepper motor microstepping was used to increase the heliostats' angular resolution (§5.1.2). Microstepping requires that continuous current be applied to a motor's windings even when its rotor is stationary. Increased parasitic power losses and overheating problems were anticipated from the start and steps were taken to

---

[17] Electrically erasable programmable read-only memory.

compensate for this. The motor driver modules were attached directly to the LCU's aluminium enclosure sidewalls using thermally conductive epoxy to allow the enclosures to act as heat sinks. The enclosures were also shaded from direct sunlight by well ventilated covers made of white (reflective) plastic sheeting. However, long term high operating temperatures still led to the eventual failure of five motor driver boards before full time microstepping was abandoned. Figure 6.3 shows a failed motor driver module.

Figure 6.3: Failed motor driver module.

The overheating problem was solved by using full stepping during normal operation and disabling the drivers in between steps to realize a low overall duty cycle. Each heliostat LCU then switched its motor drivers to microstepping mode for high angular resolution only when on-target calibration measurements were performed.

Backlash

The first version of small square heliostats' azimuth axis pre-loading mechanism was too weak to prevent backlash on moderately windy days. Backlash was reduced by using thicker elastic cords (to produce a higher pre-loading moment) and adding low friction pulleys (to reduce variability in the pre-loading force due to stiction) in the final prototype heliostats.

6.3 Heliostat Calibration and Tracking Results

This section presents on target tracking results for one of the prototype heliostats with a nominal (roughly surveyed) position 30.8 m south, 19.2 m east and 1.2 m up relative to the base of the tower, resulting in a slant range of approximately 36.3 m.

Figure 6.4 shows a full day's tracking results (measured at half-hourly intervals) on the calibration target before and after error correction coefficients were applied in the heliostat local controller unit.

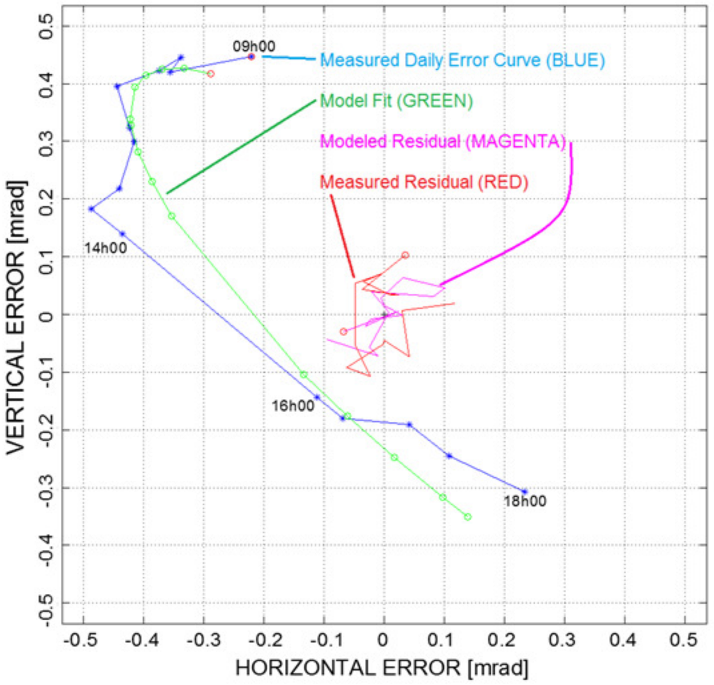

Figure 6.4: On-target tracking error curves: measured on 2012-09-02 (blue); model-fitted (green), predicted residual (magenta) and measured residual on 2012-09-06 (red).

The jagged blue line represents the measured daily tracking error on 2 September 2012 – note the lack of usable measurement points between 14:00 and 16:00 due to lens flare. The smooth green line represents the best predicted model fit (for the heliostat model of §4.2); the magenta line shows the model-predicted residual errors and the red line shows measured residual errors on 6 September 2012. Table 6.1 shows the set of error coefficients predicted by the coefficient estimation procedure (as modelled by the green line in Figure 6.4).

Table 6.1: Optimization estimated heliostat error model coefficients for 2 September 2012.

Location translation [m]			Pedestal tilt [mrad]		Axes Non-Orthogonality [mrad]	Bias Angles [mrad]	
Δ_Z	Δ_E	Δ_N	γ_N	γ_E	ψ_{no}	γ_b	α_b
0.11	1.02	-0.53	-13.27	-4.56	-1.92	-3.79	1.12

The following observations can be made about the estimated error model coefficients in relation to the experimental test setup:

- The solar roof surface has a slight slope to allow water to run off toward the sides (top and bottom edges of Figure 6.1). This may account for the south-south-western pedestal tilt.

- During installation, each heliostat's elevation reference was carefully set using a spirit level while the azimuth reference was set using a shadow-and-plumb-line method at solar noon to determine North. It is reasonable to deduce that the elevation reference implementation was more accurate (due to its simplicity) than that of the azimuth, as expressed by the values of α_b and γ_b.

The error coefficients from Table 6.1 were used by the heliostat local controller to transform in real time the ideal heliostat normal vector calculated at each control interval to compensate for the heliostat's error-adjusted local reference frame. Figure 6.5 shows a full day's model corrected tracking performance measured at one minute intervals on 6 September 2012.

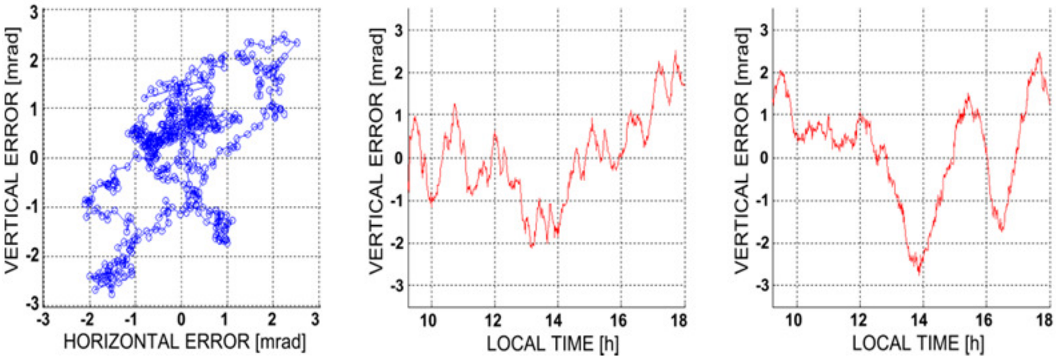

Figure 6.5: A high resolution full day's corrected tracking performance showing XY (left), X only (middle) and Y only (right).

From these tracking measurements, the daily RMS tracking error on the calibration target was calculated at 1.94 mrad. This equates to a normal vector RMS error of 0.97 mrad (since the reflected image error is twice the normal vector error). To put this figure into perspective, it means that for a full day's open-loop tracking, the heliostat's reflected image centroid stayed on average within 70.1 mm of its intended aim point on a target plane located 37.3 m away. This is a remarkable outcome when one considers the loose mechanical- and installation tolerances of the prototype heliostats.

The obvious next step was to see if the above tracking performance could be repeated. Figure 6.6 shows the horizontal and vertical tracking errors of three full days' open loop tracking for the same heliostat.

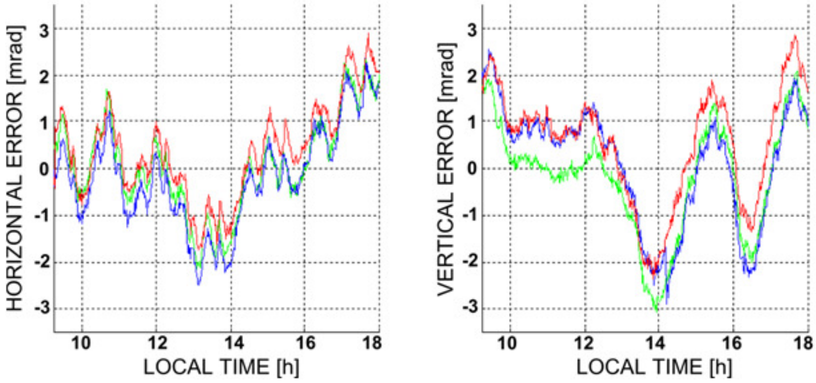

Figure 6.6: Heliostat tracking performance for 6-8 September, 2012; X-error (left) and Y-error (right).

There clearly existed a strong similarity between the tracking errors over these three days, suggesting that the residual errors were deterministic and that further model based corrections should be possible. Furthermore, the noticeable periodicity in the vertical error component (Figure 6.6, right) provided clues as to the remaining uncorrected error source, to be discussed in the next section.

6.4 Proposed Drivetrain Error Corrections

Upon closer inspection, it was found that each full cycle in the residual vertical error curve corresponded to an interval of approximately 12° in the heliostat's elevation axis, as per Figure 6.6.

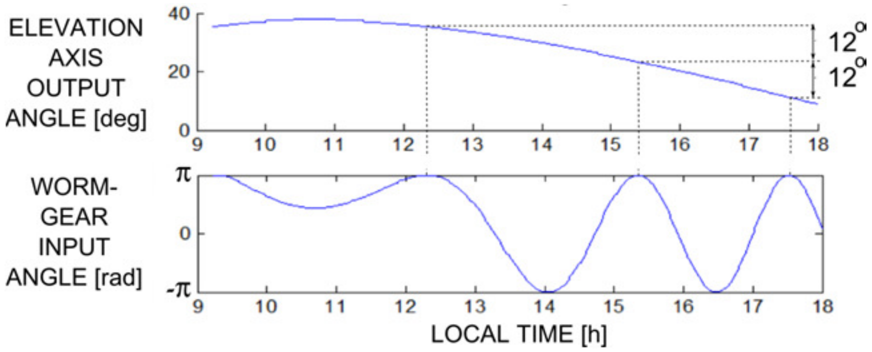

Figure 6.6: Comparison of the worm-gear induced periodic deviation versus heliostat elevation angle.

Since the heliostat mechanism used a single 30 : 1 worm gear stage, this pointed to a periodic error introduced in the worm gear's shaft rotation[18]. Some plausible physical explanations for such periodic errors include (but are not limited to):

---

[18] A 12° output shaft rotation relates to 12° x 30 = 360° input (worm gear) shaft rotation.

- A non-perpendicular worm gear end surface relative to its axis of rotation. If such a surface was to seat against an uneven or non-perpendicular bush surface, it would cause a periodic axial movement of the worm gear and a corresponding deviation on the output shaft.
- A worm gear having an off-centre bore would cause a sinusoidal variation in the gear meshing distance, again leading to a periodic perturbation on the output shaft.
- An oval worm gear would cause a periodic angle deviation with twice the worm shaft's rotational frequency.

A generic worm-gear induced sinusoidal perturbation on either the azimuth- or elevation output shafts can be modelled as follows:

$$\Delta_w = A_e \sin(r_e\theta + \psi_w) \tag{6.1}$$

where A_e is the elevation axis deviation amplitude, r_e is the elevation worm gear ratio, θ is the nominal output shaft angle and ψ_{we} is a constant phase offset.

Next, Equation 6.1 was introduced into the error model (§4.2.2, Step 2). The optimization algorithm (§5.6.4) was used to calculate worm error parameters to match the residual error curve. The resulting modelled vertical error and the residual elevation error (from Figure 6.5) are compared in Figure 6.8. There clearly exists a strong similarity between the modelled and the measured residual error.

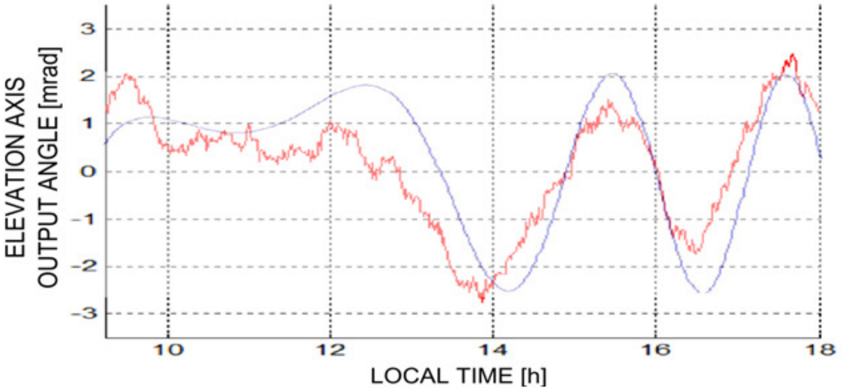

Figure 6.7: Comparison of the residual vertical tracking error (red) vs the modeled error introduced by a periodic worm gear error component (blue).

A model based solution is proposed which represents a mechanism specific error correction well suited to low cost drivetrain components. This method could potentially reduce heliostat cost significantly, since the drivetrain is the largest cost component (Kolb *et al.*, 2011). This method also represents a novel heliostat error source not previously accounted for in literature as far as the author is aware (Baheti & Scott, 1980; Stone, 1986; Khalsa *et al.*, 2011).

6.5 Integrated System Operation

Additional outcomes are discussed which validate the project's secondary objectives.

Reliability and safety

It was important for the system to operate reliably since it was deployed on an exposed rooftop in direct line of sight of office windows in surrounding buildings. Ho *et al.* (2011) show that heliostats pose a significant threat of permanent retina damage in the event of direct exposure at the optimal focal distance. A combination of the following safety measures ensured that surrounding buildings were never inadvertently exposed:

- When approaching the tower mounted target from a stowed position, each heliostat moved azimuth first, elevation last. This meant that reflected solar images travelled along the ground until the final upward approach from the base to the top of the tower. This sequence was reversed when stowing.
- Integrity checking of all data packets prevented corrupt or broken messages from potentially confusing tracking calculations or aim point commands.
- A watchdog timer in the microcontroller of each heliostat LCU allowed recovery from stalled states (for example endless loops). Similarly, heartbeat timers in both the CCUs and LCUs protected the system against loss of control due to software stalling or communication failure.

System setup, emergency stow and initial target approach

The heliostat LCUs automatically loaded the last stored values of location, aim point, motor positions and error correction coefficients while the GUI allowed for reconfiguration of all parameters by the operator. During testing, the operator could trigger the system to remove all heliostat images from the receiver in under 10 seconds and move all heliostats to their stowed positions (heliostat normal vector at horizontal, facing North) in under two minutes. Finally, a target search method was demonstrated whereby an individual heliostat was commanded to adjust its aim point in an outward spiral until its reflected image intersected with the calibration target. The search algorithm is described in Appendix E.2.

6.6 Conclusion

The accurate tracking results shown in Section 6.3 validates the integrated system; it proves the correct functioning of the solar position algorithm, the heliostat error model, the communication network and the overall processing and error correction strategy. The various problems encountered during the practical implementation provided several important lessons. Project conclusions follow in Chapter 7.

CHAPTER 7

Conclusion

This thesis focused on developing a heliostat field control method and system architecture within the context of a 5 MW_e SUNSPOT pilot plant. This chapter summarizes the project's main findings and contributions. Conclusions are drawn about the meaning of the research and recommendations are made for future work.

7.1. Summary of Work

High level sizing calculations showed that a proposed 5 MW_e central receiver system (CRS) pilot plant with seven hours of thermal storage would require up to 10 000 heliostats. Highly accurate two-axis tracking (typically <1mrad RMS angular error) is needed to minimize spillage loss and to ensure reliable plant operation.

A mechanism-specific heliostat movement model was developed which takes into account major sources of tracking errors. The model uses the heliostat's location and aim point; the sun's angle and a heliostat-specific set of error parameters to calculate the error offset of the heliostat's projected solar image onto a calibration target plane.

A control strategy was developed which combines open loop tracking (using a solar algorithm) with an error correction method based on the heliostat movement model. Mathematical optimization was used to fit model coefficients to a set of real-world tracking error measurements for each heliostat in the system.

A system architecture was proposed in which processing tasks are distributed into three tiers. Modularity and scalability was achieved by grouping heliostats into self-sufficient clusters which handle all real-time processing related to tracking. This means that additional heliostat clusters can be added without increasing the real-time processing load across the rest of the system.

A prototype heliostat array was constructed which functioned as a scaled down subsection of the proposed 5 MW_e pilot plant control system. The prototype system successfully demonstrated the proposed network architecture, processing strategy and overall control method. On target tracking tests were performed which demonstrated sub-milliradian daily RMS tracking errors over three consecutive days. The system further demonstrated integrated functionality with an operator interface for manual override and status monitoring of all heliostats. Additionally, the target approach, target search and emergency stow objectives were successfully met.

7.2 Conclusions

All the objectives of this thesis have been successfully met and exceeded in some instances. The control method presented here benefits from simplicity and low cost associated with open loop control while meeting the performance requirements. It has been demonstrated that sub-milliradian tracking results are achievable even with low tolerance heliostat mechanisms and imprecise installation, thereby potentially allowing for long term cost reduction.

The prototype system met the tracking accuracy objective of 1 mrad RMS as set out in Chapter 1, thereby validating the control method. This proves that a strong physical basis exists for reducing heliostat tracking errors by characterization of deterministic errors using a movement model. This approach further led to a possibly novel proposal to correct errors stemming from drivetrain gearing imperfections.

The three-tiered control architecture performed without fault. Testing was limited due to the scope of deployment, but nothing was observed to discredit its scaling potential. Distributed processing allowed the use of simple, low cost microcontrollers in the heliostat local controller units (LCUs). This may be an important driver for cost reduction since the ratio of LCUs to heliostats is inherently one-to-one.

The initial use of full time microstepping in the prototype system led to overheating and eventual failure of several motor driver modules. This highlighted the need for careful thermal design of electronic circuits (and minimization of parasitic losses) to survive the high ambient temperatures typically associated with CSP plants.

The constraints of developing a system for rooftop deployment led to an interesting support structure solution which turned out to be novel and which may even produce a patent, as will be discussed in the next section.

7.3 Summary of Contributions

This was the first project relating to heliostat control in STERG. To the level of individual components and methods, the system comprising hardware and software was developed originally for this project. The resulting system satisfied the project objectives, but will also serve as a platform for future research. To this end, considerable effort was invested in designing the heliostat mechanisms and other physical components to survive long term outdoor deployment. Flexibility and ease of future adaptation featured strongly in the selection of hardware modules and software environments. The choice of Arduino microcontroller boards for the heliostat LCUs illustrates this point.

Additional contributions can be summarized as follows:

- A peer reviewed research paper was presented at SolarPACES, the premier annual conference for CSP worldwide, with publication of the proceedings due in January 2014 (Malan & Gauché, 2013b).
- A possibly novel source of heliostat tracking errors (which occur due to drivetrain gearing imperfections) was identified and an error model component was proposed to correct for it.
- The control method and system architecture developed during this thesis is at the time of writing being used in Helio40, a Sasol[19] funded 40 m^2 heliostat array facility, to be commissioned at the solar roof laboratory by early 2014.
- Stellenbosch University acknowledged the intellectual property value of the heliostat support structure and applied for a patent to protect the concept (Malan & Gauché, 2012a). At the time of writing, the international Patent Cooperation Treaty (PCT) process for this was underway.

7.4 Recommendations for Further Research

The broad scope of this study means that many topics exist for further study. This section recommends areas which, in the author's opinion, could lead to significant improvements in the system's performance:

- Investigation of the newly identified drivetrain specific error sources including further modelling and experimental validation of the proposed correction method discussed in §6.3.
- A sensitivity analysis to better understand the heliostat error model's parameter dependencies and to improve the accuracy with which calibration coefficients can be estimated. Zhang *et al.* (2012) describes statistical methods to analyse parameter uncertainties for the error model of Khalsa *et al.* (2011).
- Implementation of a correction strategy for errors occurring in the beam characterization system such as camera lens distortions, as discussed by Van der Westhuizen (2011:35).
- Investigation of wireless power and communication strategies, as motivated in a recent SolarPACES paper on the topic (Kubisch *et al.*, 2011). Work on this has already begun; the first generation of such a wireless topology will be used in the Helio40 system previously mentioned in Section 7.3.

---

[19] Sasol is a major South African energy and chemicals company, best known for producing oil and other petroleum-related products from coal using the Fischer-Tropsch process.

Appendices

A. Model Validation Results

Initial validation of the heliostat error model was done by modelling four error scenarios from Stone & Jones (1999). Visual comparisons were then made between the plots of tracking offsets predicted by the model of §4.2 and the published plots. Finally, the calculated daily RMS error was compared to the published values.

Case1: Pedestal Tilt North

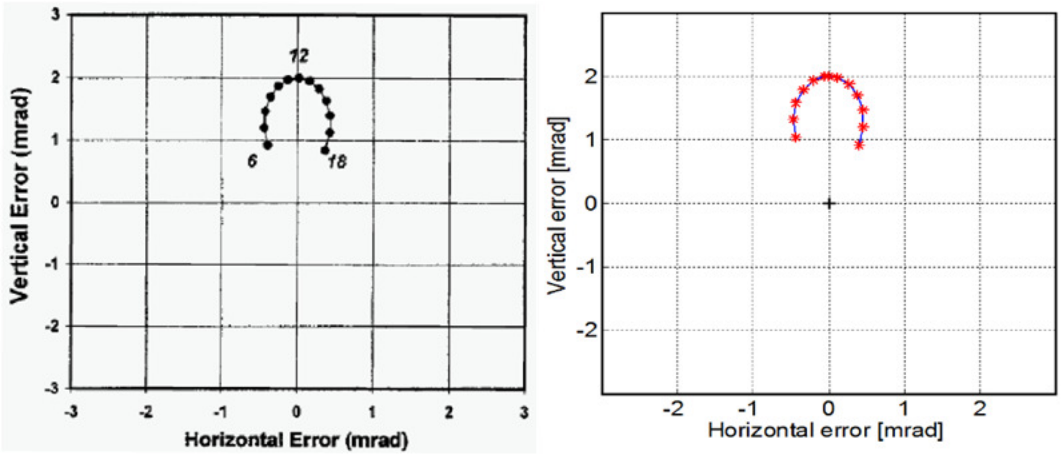

Figure A.1: Pedestal tilt error: 1 mrad North (Stone & Jones, 1999) versus modelled error.

Case2: Pedestal Tilt East

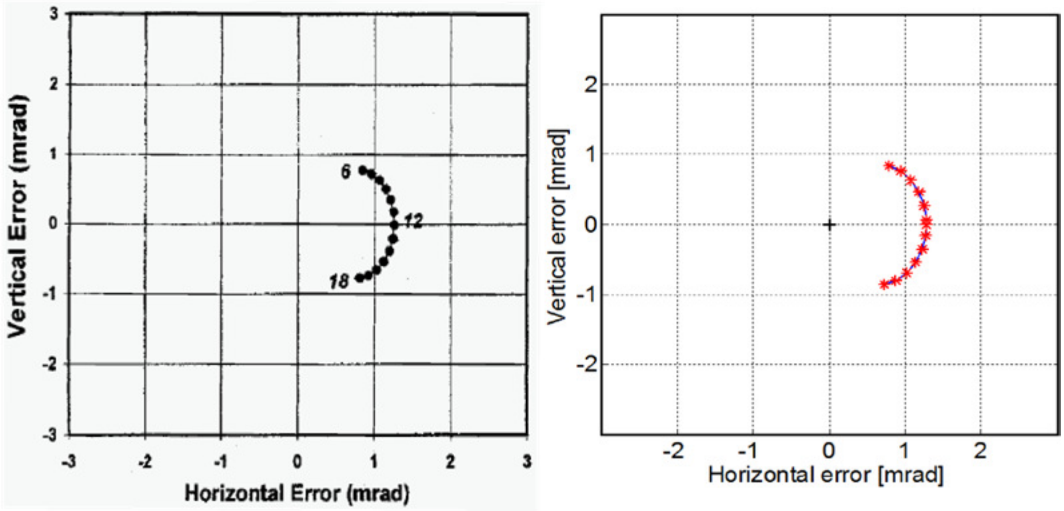

Figure A.2: Pedestal tilt error: 1 mrad East (Stone & Jones, 1999) versus modelled error.

Case3: Pedestal Tilt Southwest

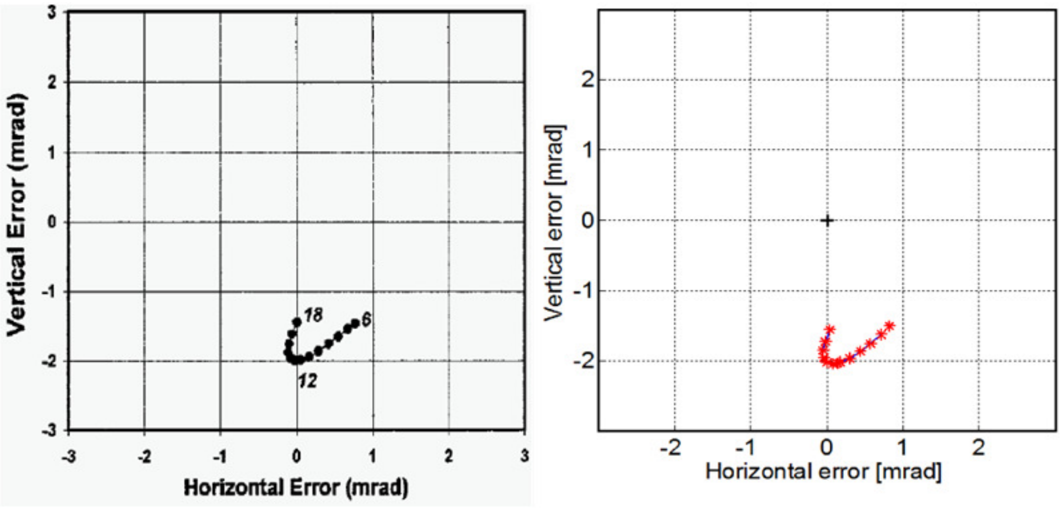

Figure A.3: Pedestal tilt error: 1 mrad Southeast (Stone & Jones, 1999) versus modelled error.

Case 4: Combined Pedestal tilt North and Elevation Bias Down

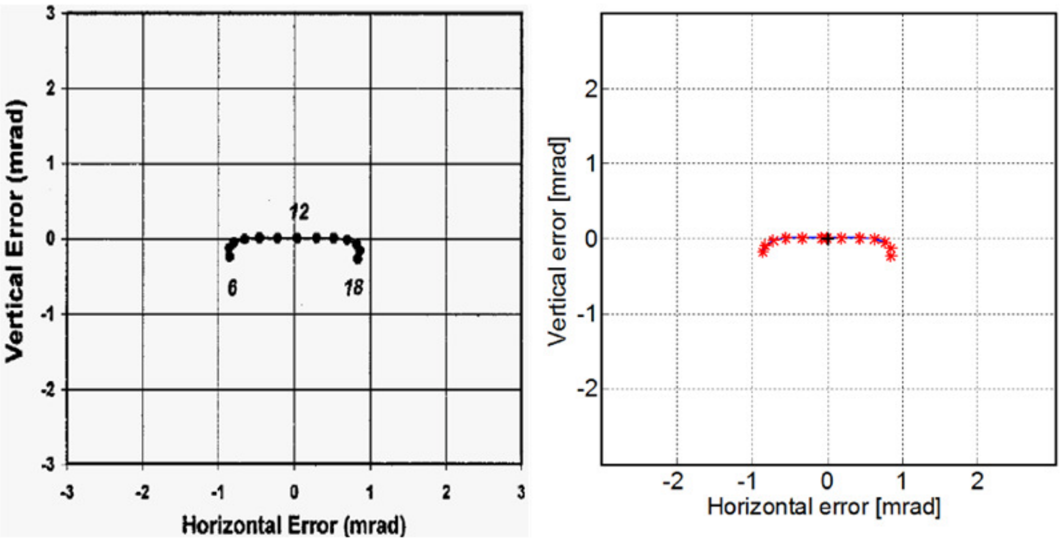

Figure A.4: Combined Pedestal tilt error 1 mrad North and Elevation offset 1mrad upwards (Stone & Jones, 1999) versus modelled error.

Comparison of RMS errors

Table A.1 shows a comparison of the calculated daily RMS errors for the modelled tracking offsets versus the published figures in Stone & Jones (1999).

Table A.1: Comparison of calculated versus published values of daily RMS tracking errors.

Validation Case	Modelled value of E_{RMS} [mrad]	Published value of E_{RMS} [mrad]
Pedestal tilt 1 mrad North	1.64	1.61
Pedestal tilt 1 mrad East	1.24	1.23
Pedestal tilt 1 mrad Southwest	1.86	1.81
Pedestal tilt 1 mrad North and elevation bias 1 mrad down.	0.63	0.64

B. Mechanical Drawings

The Second Generation Heliostat's mechanical drawings are included here. All parts were made from laser cut and bent mild steel sheets.

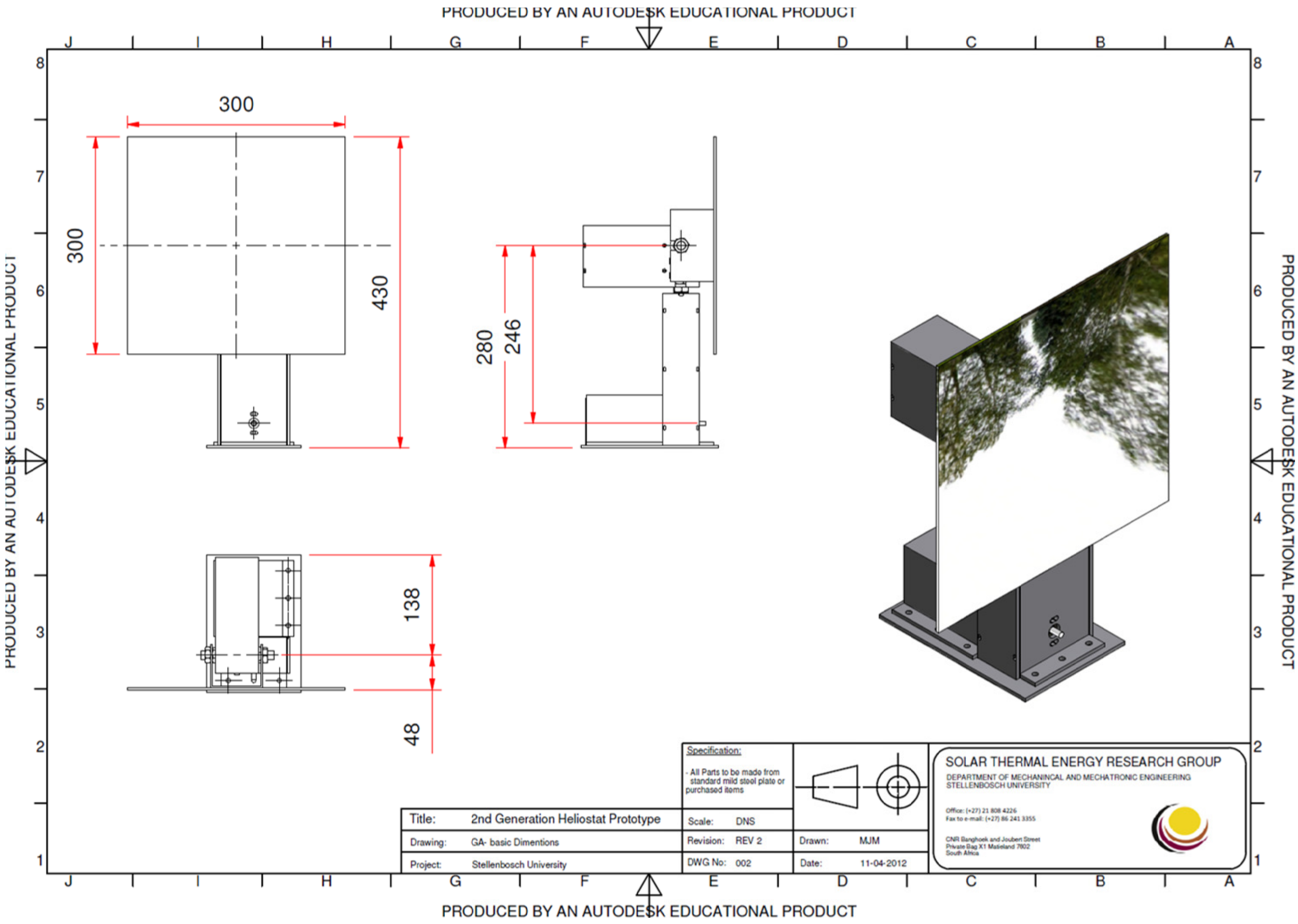
PRODUCED BY AN AUTODESK EDUCATIONAL PRODUCT
300
300
430
280
246
138
48
Title: 2nd Generation Heliostat Prototype
Drawing: GA- basic Dimentions
Project: Stellenbosch University
Specification:
- All Parts to be made from standard mild steel plate or purchased items
Scale: DNS
Revision: REV 2
DWG No: 002
Drawn: MJM
Date: 11-04-2012
SOLAR THERMAL ENERGY RESEARCH GROUP
DEPARTMENT OF MECHANINCAL AND MECHATRONIC ENGINEERING
STELLENBOSCH UNIVERSITY
Office: (+27) 21 808 4226
Fax to e-mail: (+27) 86 241 3355
CNR Banghoek and Joubert Street
Private Bag X1 Matieland 7602
South Africa
A
B
C
D
E
F
G
H
I
J
1
2
3
4
5
6
7
8

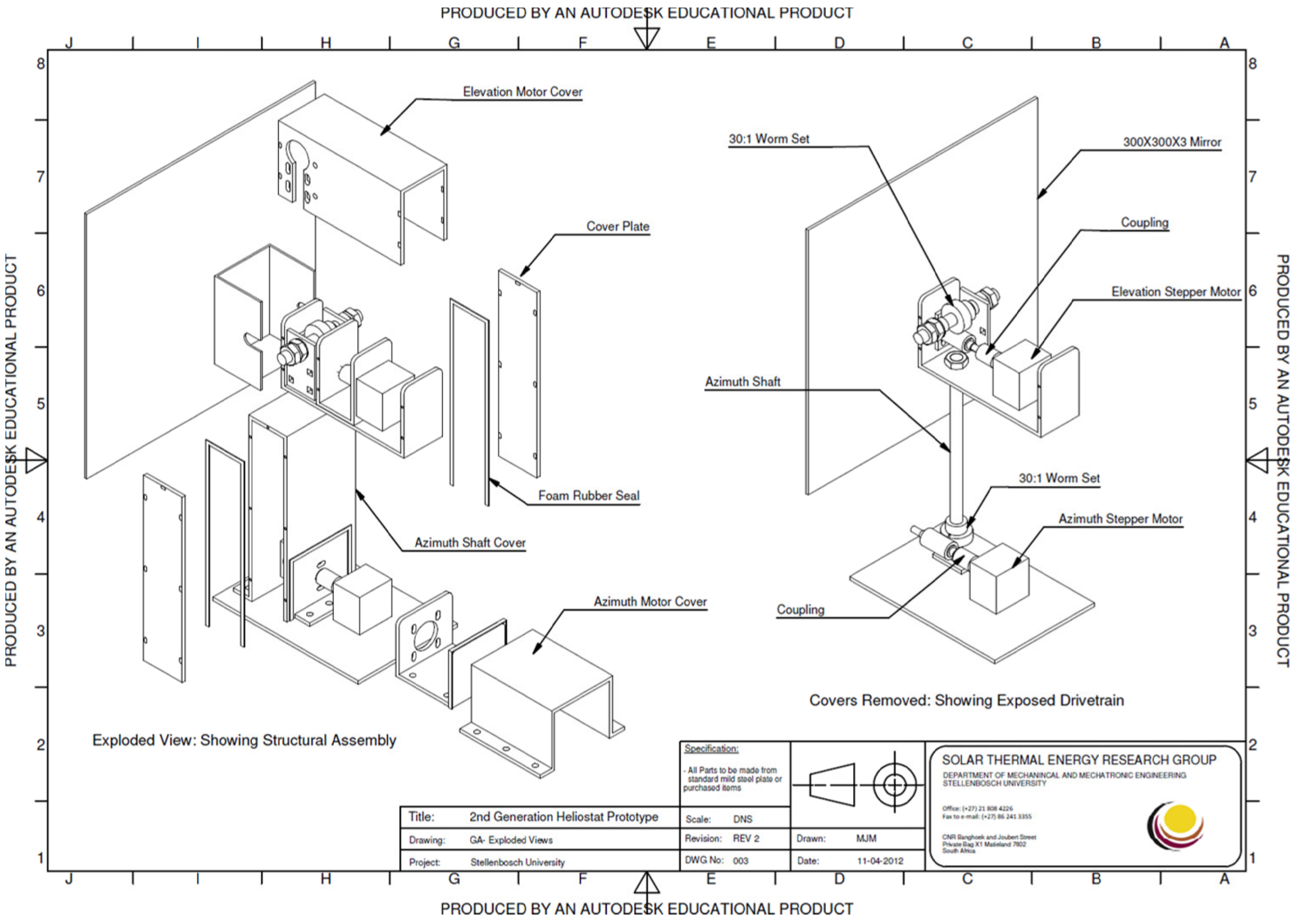
PRODUCED BY AN AUTODESK EDUCATIONAL PRODUCT
Elevation Motor Cover
Cover Plate
Foam Rubber Seal
Azimuth Shaft Cover
Azimuth Motor Cover
Exploded View: Showing Structural Assembly
30:1 Worm Set
300X300X3 Mirror
Coupling
Elevation Stepper Motor
Azimuth Shaft
30:1 Worm Set
Azimuth Stepper Motor
Coupling
Covers Removed: Showing Exposed Drivetrain
Specification:
- All Parts to be made from standard mild steel plate or purchased items
Title: 2nd Generation Heliostat Prototype
Drawing: GA- Exploded Views
Project: Stellenbosch University
Scale: DNS
Revision: REV 2
DWG No: 003
Drawn: MJM
Date: 11-04-2012
SOLAR THERMAL ENERGY RESEARCH GROUP
DEPARTMENT OF MECHANINCAL AND MECHATRONIC ENGINEERING
STELLENBOSCH UNIVERSITY
Office: (+27) 21 808 4226
Fax to e-mail: (+27) 86 241 3355
CNR Banghoek and Joubert Street
Private Bag X1 Matieland 7602
South Africa
A B C D E F G H I J
1 2 3 4 5 6 7 8

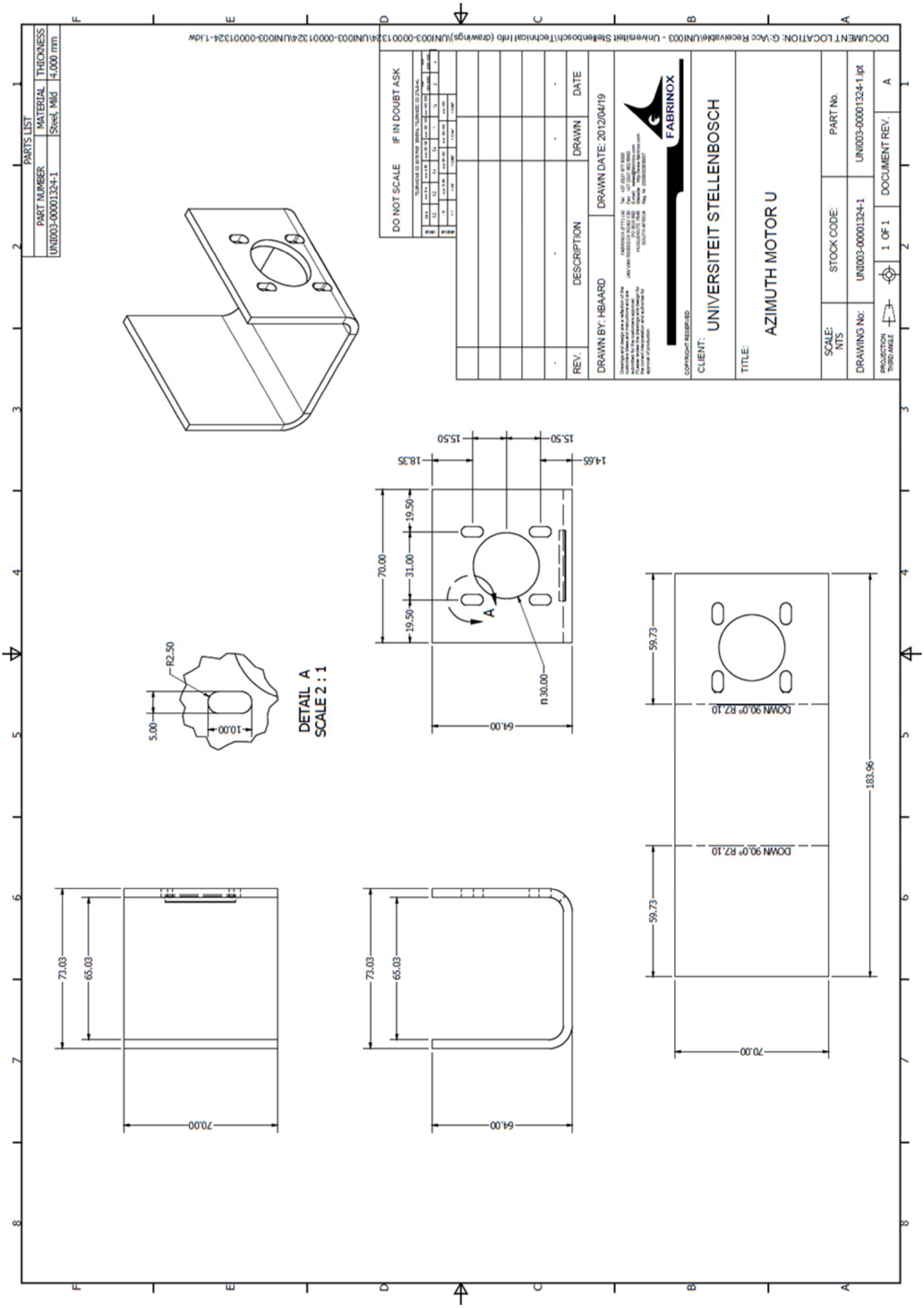
DOCUMENT LOCATION: G:\Acc Receivable\UNI003 - Universiteit Stellenbosch\Technical Info (drawings)\UNI003-00001324\UNI003-00001324\UNI003-00001324-1.idw
PARTS LIST
PART NUMBER
MATERIAL
THICKNESS
UNI003-00001324-1
Steel, Mild
4.000 mm
DO NOT SCALE
IF IN DOUBT ASK
REV.
DESCRIPTION
DRAWN
DATE
DRAWN BY: HBAARD
DRAWN DATE: 2012/04/19
FABRINOX
COPYRIGHT RESERVED
CLIENT:
UNIVERSITEIT STELLENBOSCH
TITLE:
AZIMUTH MOTOR U
SCALE: NTS
STOCK CODE:
PART No.
DRAWING No:
UNI003-00001324-1
UNI003-00001324-1.ipt
PROJECTION THIRD ANGLE
1 OF 1
DOCUMENT REV.
A
15.50
15.50
18.35
14.65
19.50
31.00
19.50
70.00
A
n30.00
64.00
R2.50
5.00
10.00
DETAIL A
SCALE 2 : 1
59.73
DOWN 90.0° R7.10
183.96
DOWN 90.0° R7.10
59.73
70.00
73.03
65.03
70.00
73.03
65.03
64.00
A
B
C
D
E
F
1
2
3
4
5
6
7
8

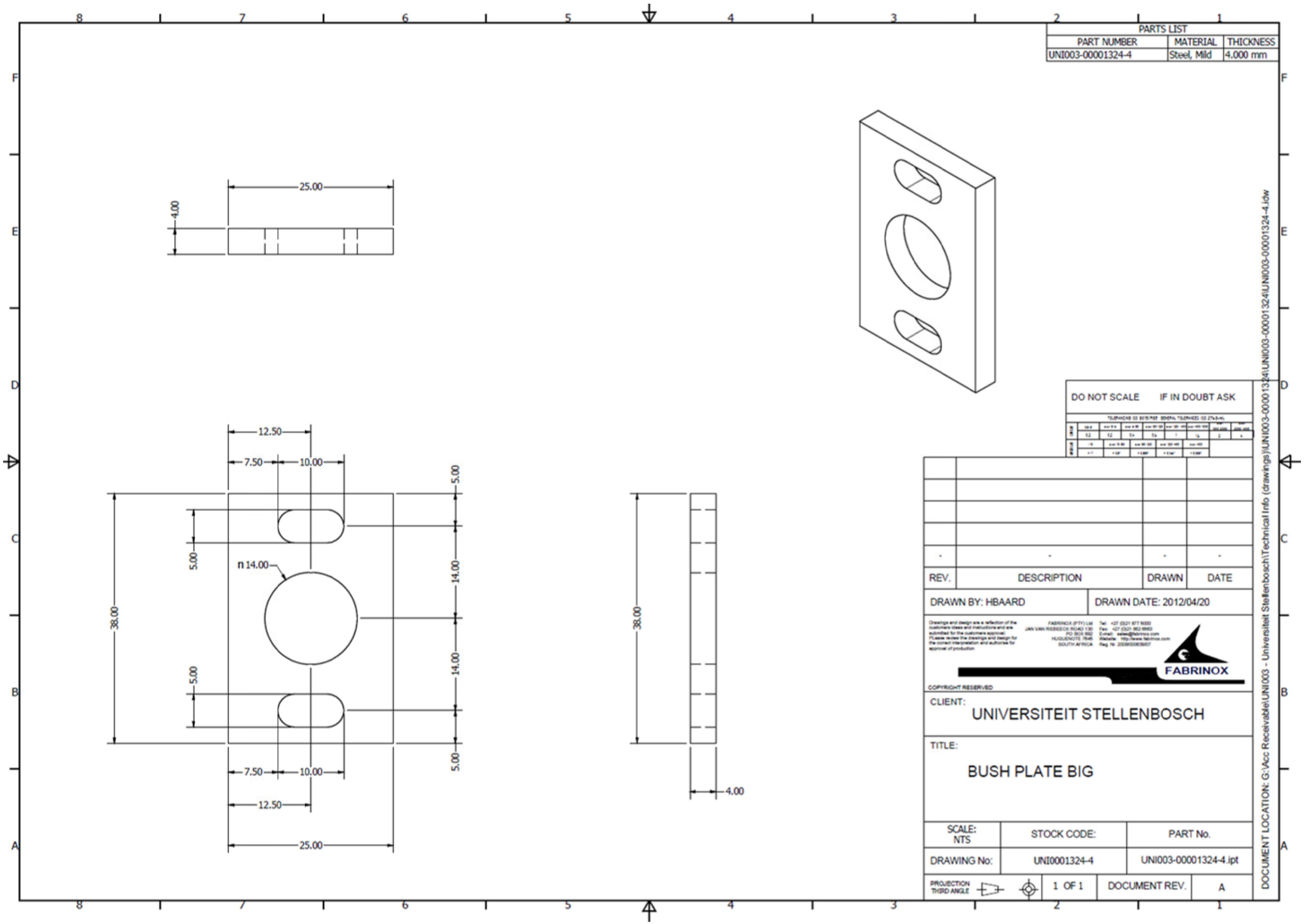
PARTS LIST
PART NUMBER
MATERIAL
THICKNESS
UNI003-00001324-4
Steel, Mild
4.000 mm
25.00
4.00
12.50
7.50
10.00
5.00
n 14.00
14.00
38.00
DO NOT SCALE
IF IN DOUBT ASK
REV.
DESCRIPTION
DRAWN
DATE
DRAWN BY: HBAARD
DRAWN DATE: 2012/04/20
FABRINOX
COPYRIGHT RESERVED
CLIENT:
UNIVERSITEIT STELLENBOSCH
TITLE:
BUSH PLATE BIG
SCALE:
NTS
STOCK CODE:
PART No.
DRAWING No:
UNI0001324-4
UNI003-00001324-4.ipt
PROJECTION THIRD ANGLE
1 OF 1
DOCUMENT REV.
A
DOCUMENT LOCATION: G:\Acc Receivable\UNI003 - Universiteit Stellenbosch\Technical Info (drawings)\UNI003-00001324\UNI003-00001324\UNI003-00001324-4.idw

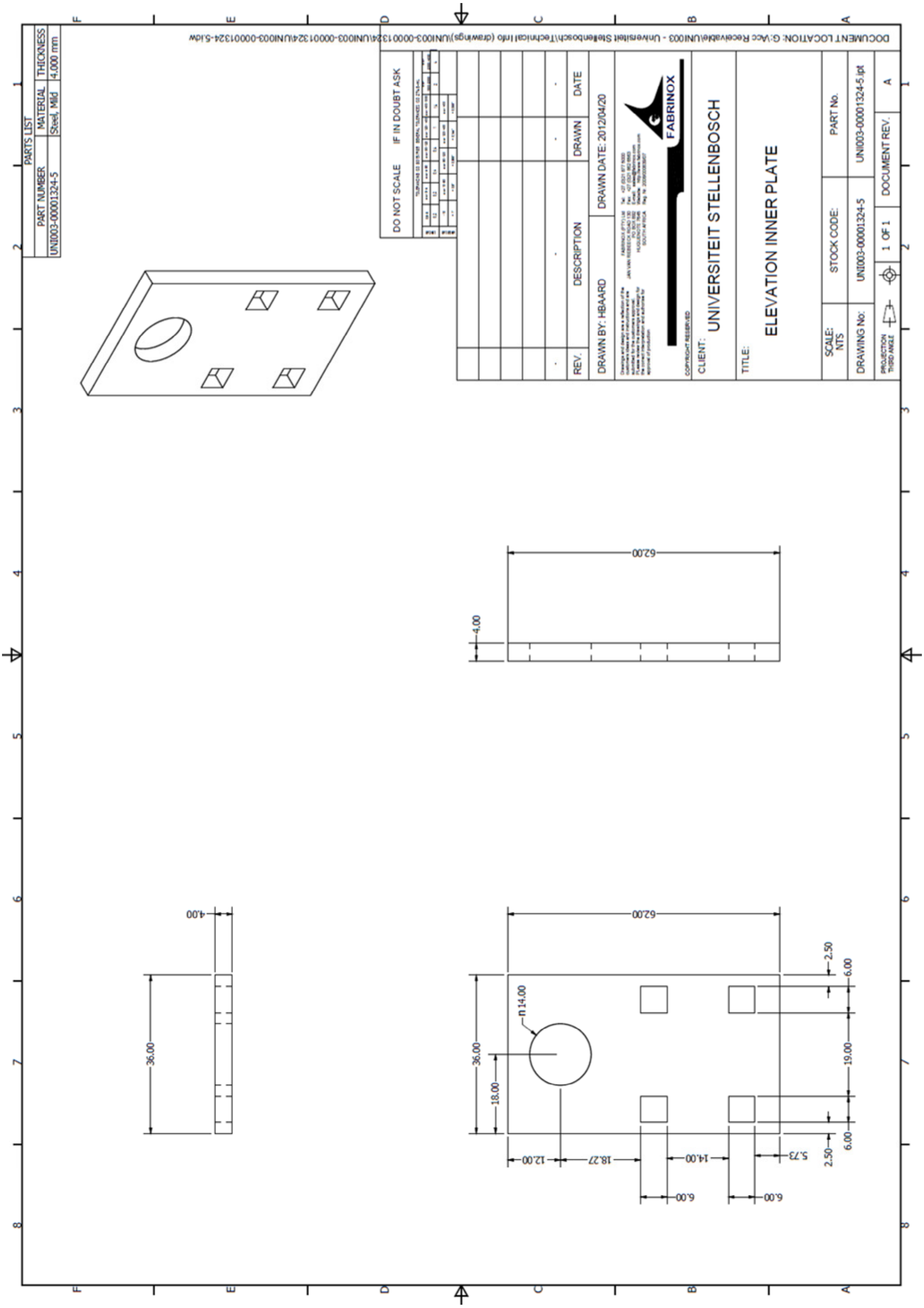
PARTS LIST
PART NUMBER
MATERIAL
THICKNESS
UNI003-00001324-5
Steel, Mild
4.000 mm
DOCUMENT LOCATION: G:\Acc Receivable\UNI003 - Universiteit Stellenbosch\Technical Info (drawings)\UNI003-00001324\UNI003-00001324\UNI003-00001324-5.idw
DO NOT SCALE IF IN DOUBT ASK
REV.
DESCRIPTION
DRAWN
DATE
DRAWN BY: HBAARD
DRAWN DATE: 2012/04/20
FABRINOX
COPYRIGHT RESERVED
CLIENT:
UNIVERSITEIT STELLENBOSCH
TITLE:
ELEVATION INNER PLATE
SCALE: NTS
STOCK CODE:
PART No.
DRAWING No:
UNI003-00001324-5
UNI003-00001324-5.ipt
PROJECTION THIRD ANGLE
1 OF 1
DOCUMENT REV.
A
62.00
4.00
36.00
18.00
n 14.00
12.00
18.27
14.00
5.73
6.00
19.00
2.50
A
B
C
D
E
F
1
2
3
4
5
6
7
8

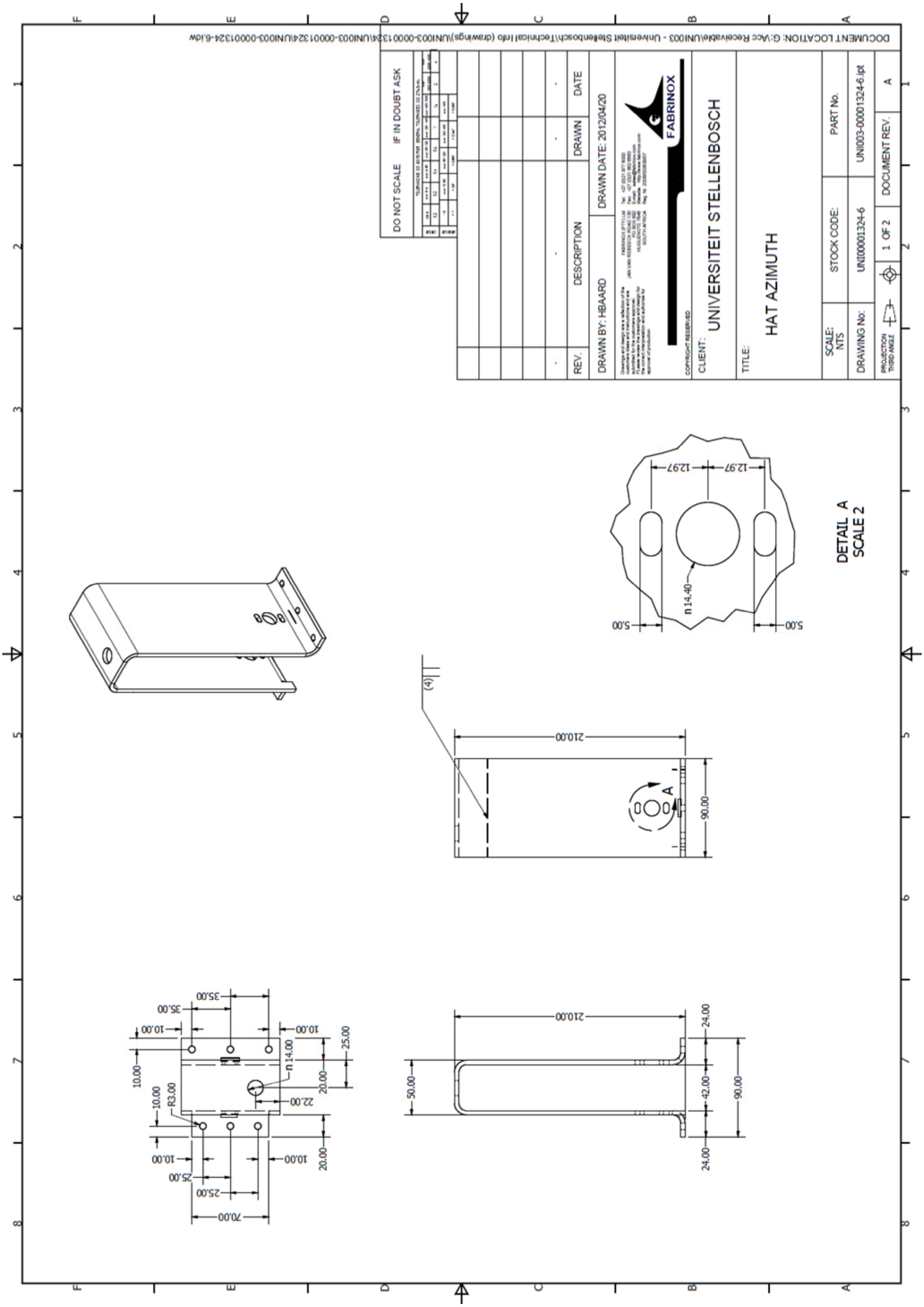
DOCUMENT LOCATION: G:\Acc Receivable\UNI003 - Universiteit Stellenbosch\Technical Info (drawings)\UNI003-00001324\UNI003-00001324\UNI003-00001324-6.idw
DO NOT SCALE
IF IN DOUBT ASK
REV.
DESCRIPTION
DRAWN
DATE
DRAWN BY: HBAARD
DRAWN DATE: 2012/04/20
FABRINOX
COPYRIGHT RESERVED
CLIENT:
UNIVERSITEIT STELLENBOSCH
TITLE:
HAT AZIMUTH
SCALE:
NTS
STOCK CODE:
PART No.
DRAWING No:
UNI00001324-6
UNI003-00001324-6.ipt
PROJECTION THIRD ANGLE
1 OF 2
DOCUMENT REV.
A
DETAIL A
SCALE 2
12.97
12.97
n14.40
5.00
5.00
(4)
210.00
90.00
A
210.00
50.00
24.00
42.00
90.00
24.00
35.00
35.00
10.00
10.00
25.00
14.00
20.00
22.00
10.00
10.00
R3.00
10.00
10.00
25.00
25.00
20.00
70.00
A
B
C
D
E
F
1
2
3
4
5
6
7
8

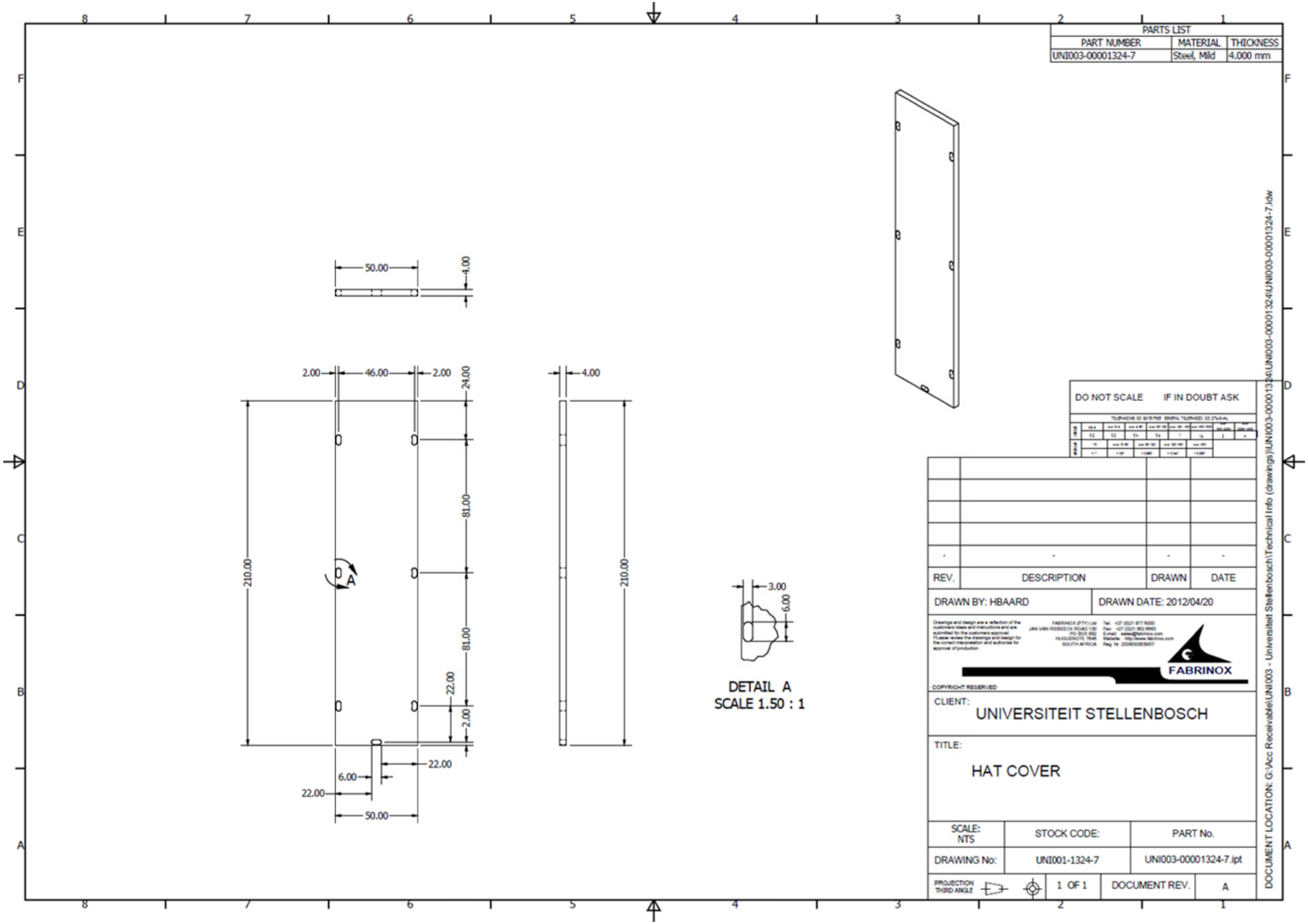
PARTS LIST
PART NUMBER
MATERIAL
THICKNESS
UNI003-00001324-7
Steel, Mild
4.000 mm
50.00
4.00
2.00
46.00
2.00
24.00
4.00
210.00
81.00
81.00
22.00
2.00
22.00
6.00
22.00
50.00
210.00
A
3.00
6.00
DETAIL A
SCALE 1.50 : 1
DO NOT SCALE
IF IN DOUBT ASK
REV.
DESCRIPTION
DRAWN
DATE
DRAWN BY: HBAARD
DRAWN DATE: 2012/04/20
FABRINOX
COPYRIGHT RESERVED
CLIENT:
UNIVERSITEIT STELLENBOSCH
TITLE:
HAT COVER
SCALE: NTS
STOCK CODE:
PART No.
DRAWING No:
UNI001-1324-7
UNI003-00001324-7.ipt
PROJECTION THIRD ANGLE
1 OF 1
DOCUMENT REV.
A
DOCUMENT LOCATION: G:\Acc Receivable\UNI003 - Universiteit Stellenbosch\Technical Info (drawings)\UNI003-00001324\UNI003-00001324\UNI003-00001324-7.idw

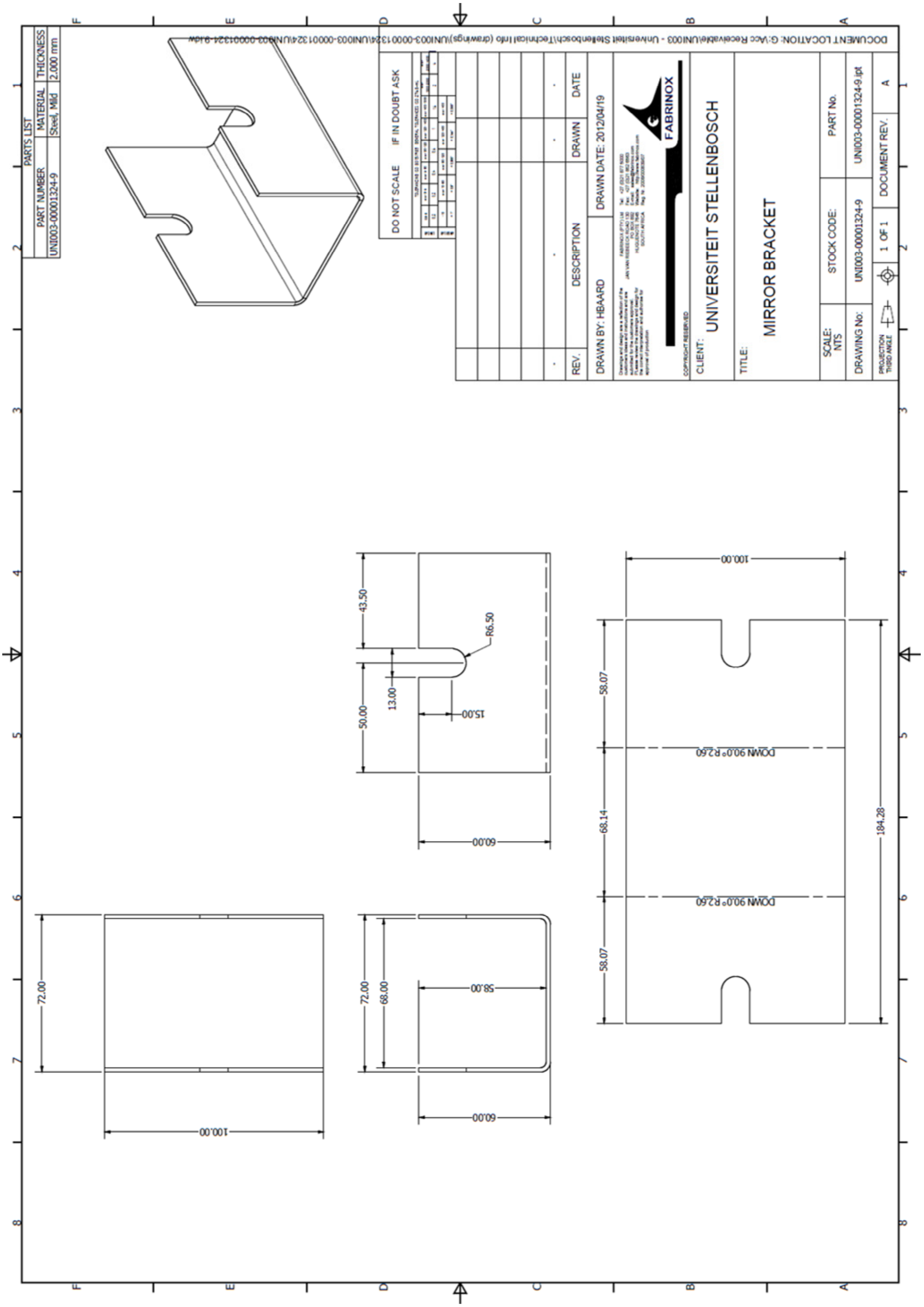
DOCUMENT LOCATION: G:\Acc Receivable\UNI003 - Universiteit Stellenbosch\Technical Info (drawings)\UNI003-00001324\UNI003-00001324\UNI003-00001324-9.idw
PARTS LIST
PART NUMBER
MATERIAL
THICKNESS
UNI003-00001324-9
Steel, Mild
2.000 mm
DO NOT SCALE
IF IN DOUBT ASK
REV.
DESCRIPTION
DRAWN
DATE
DRAWN BY: HBAARD
DRAWN DATE: 2012/04/19
FABRINOX
COPYRIGHT RESERVED
CLIENT:
UNIVERSITEIT STELLENBOSCH
TITLE:
MIRROR BRACKET
SCALE: NTS
STOCK CODE:
PART No.
DRAWING No:
UNI003-00001324-9
UNI003-00001324-9.ipt
PROJECTION THIRD ANGLE
1 OF 1
DOCUMENT REV.
A
43.50
R6.50
13.00
15.00
50.00
60.00
100.00
58.07
68.14
58.07
184.28
DOWN 90.0° R2.60
DOWN 90.0° R2.60
72.00
72.00
68.00
58.00
60.00
100.00
A
B
C
D
E
F
1
2
3
4
5
6
7
8

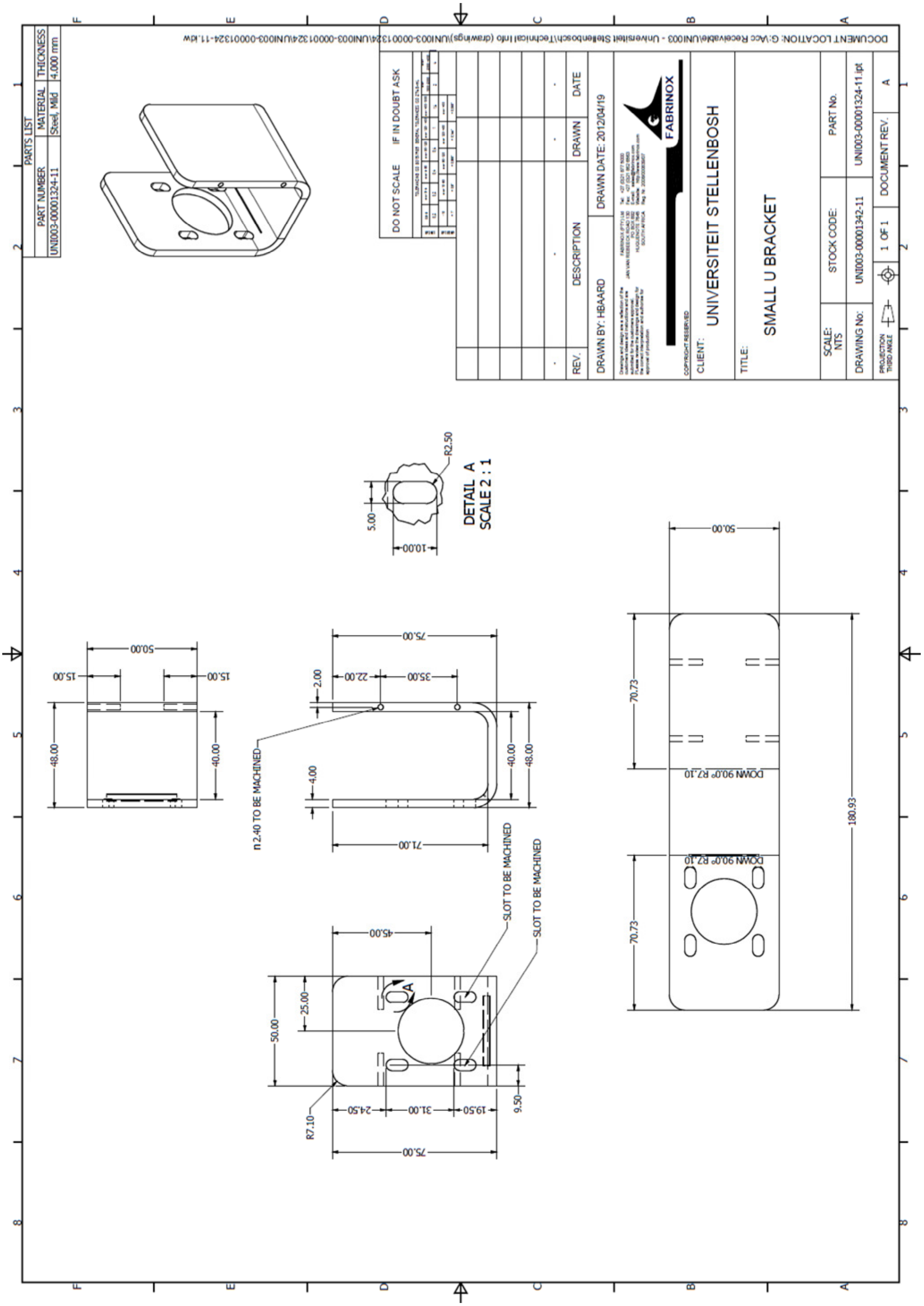
PARTS LIST
PART NUMBER
MATERIAL
THICKNESS
UNI003-00001324-11
Steel, Mild
4.000 mm
DOCUMENT LOCATION: G:\Acc Receivable\UNI003 - Universiteit Stellenbosch\Technical Info (drawings)\UNI003-00001324\UNI003-00001324\UNI003-00001324-11.idw
DO NOT SCALE
IF IN DOUBT ASK
REV.
DESCRIPTION
DRAWN
DATE
DRAWN BY: HBAARD
DRAWN DATE: 2012/04/19
FABRINOX
COPYRIGHT RESERVED
CLIENT:
UNIVERSITEIT STELLENBOSH
TITLE:
SMALL U BRACKET
SCALE: NTS
STOCK CODE:
PART No.
DRAWING No:
UNI003-00001342-11
UNI003-00001324-11.ipt
DOCUMENT REV.
A
1 OF 1
PROJECTION THIRD ANGLE
DETAIL A
SCALE 2 : 1
R2.50
5.00
10.00
50.00
15.00
15.00
48.00
40.00
75.00
2.00
22.00
35.00
n 2.40 TO BE MACHINED
4.00
40.00
48.00
71.00
45.00
SLOT TO BE MACHINED
SLOT TO BE MACHINED
A
50.00
25.00
R7.10
24.50
31.00
19.50
9.50
75.00
50.00
70.73
DOWN 90.0° R7.10
DOWN 90.0° R7.10
180.93
70.73

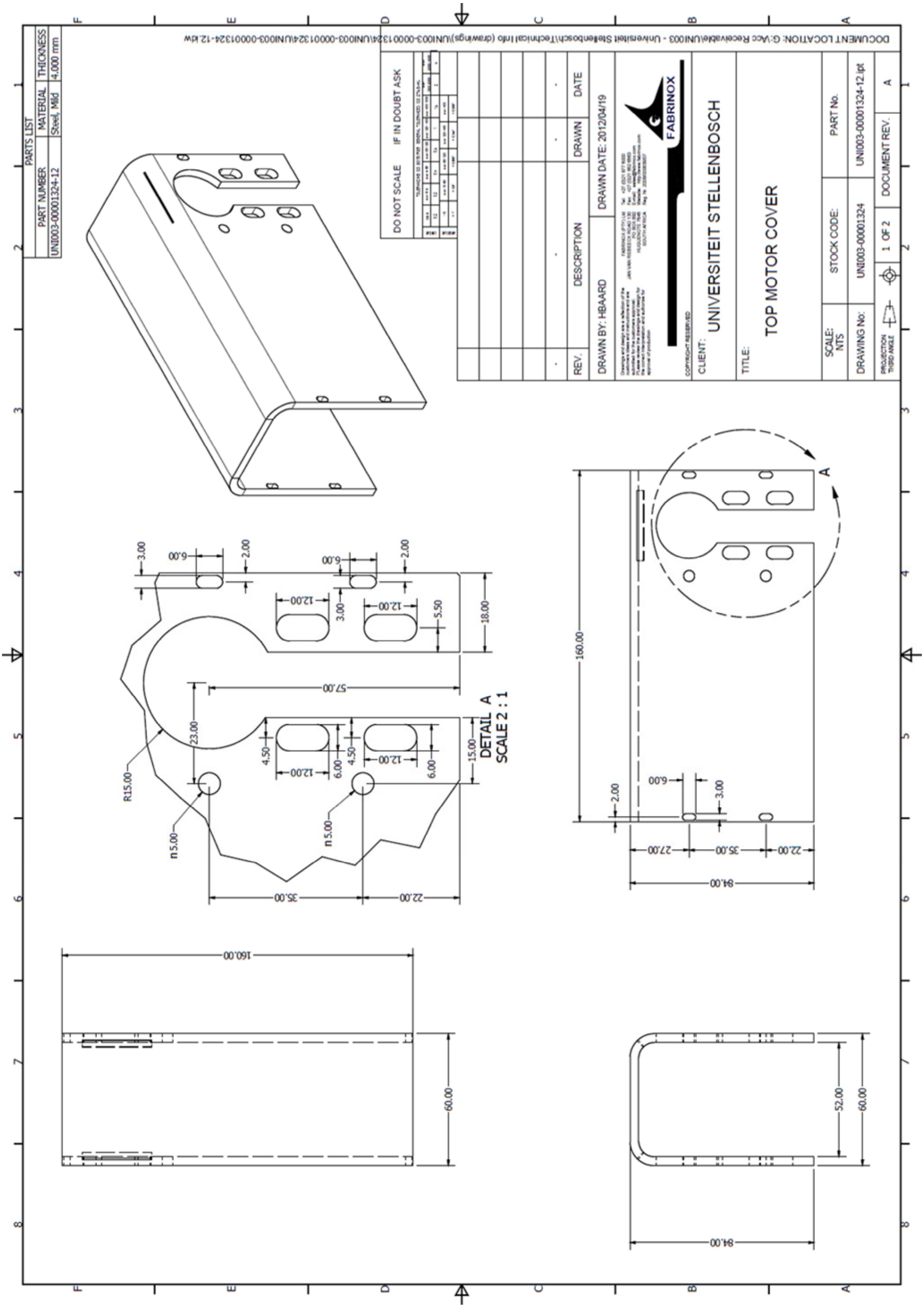
PARTS LIST
PART NUMBER
MATERIAL
THICKNESS
UNI003-00001324-12
Steel, Mild
4.000 mm
DOCUMENT LOCATION: G:\Acc Receivable\UNI003 - Universiteit Stellenbosch\Technical Info (drawings)\UNI003-00001324\UNI003-00001324\UNI003-00001324-12.idw
DO NOT SCALE
IF IN DOUBT ASK
REV.
DESCRIPTION
DRAWN
DATE
DRAWN BY: HBAARD
DRAWN DATE: 2012/04/19
FABRINOX
COPYRIGHT RESERVED
CLIENT:
UNIVERSITEIT STELLENBOSCH
TITLE:
TOP MOTOR COVER
SCALE: NTS
STOCK CODE:
PART No.
DRAWING No:
UNI003-00001324
UNI003-00001324-12.ipt
PROJECTION THIRD ANGLE
1 OF 2
DOCUMENT REV.
A
DETAIL A
SCALE 2 : 1
A
R15.00
n5.00
n5.00
6.00
3.00
2.00
6.00
2.00
12.00
12.00
3.00
5.50
18.00
57.00
23.00
4.50
4.50
6.00
12.00
12.00
6.00
15.00
35.00
22.00
160.00
6.00
2.00
3.00
27.00
35.00
22.00
84.00
160.00
60.00
52.00
60.00
84.00
A
B
C
D
E
F
1
2
3
4
5
6
7
8

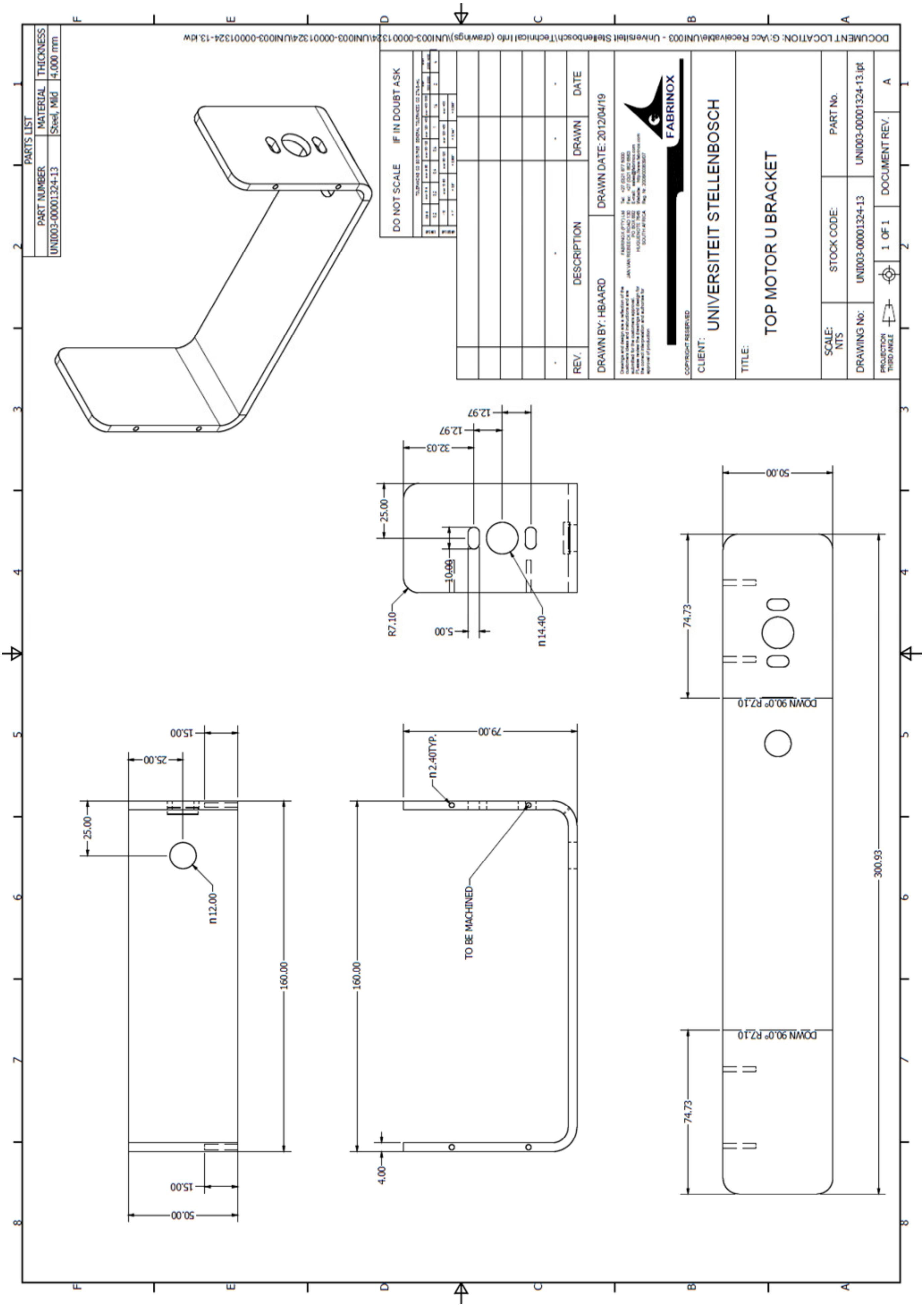
DOCUMENT LOCATION: G:\Acc Receivable\UNI003 - Universiteit Stellenbosch\Technical Info (drawings)\UNI003-00001324\UNI003-00001324\UNI003-00001324-13.idw
PARTS LIST
PART NUMBER
UNI003-00001324-13
MATERIAL
Steel, Mild
THICKNESS
4.000 mm
DO NOT SCALE
IF IN DOUBT ASK
REV.
DESCRIPTION
DRAWN
DATE
DRAWN BY: HBAARD
DRAWN DATE: 2012/04/19
FABRINOX
COPYRIGHT RESERVED
CLIENT:
UNIVERSITEIT STELLENBOSCH
TITLE:
TOP MOTOR U BRACKET
SCALE:
NTS
STOCK CODE:
PART No.
DRAWING No:
UNI003-00001324-13
UNI003-00001324-13.ipt
PROJECTION THIRD ANGLE
1 OF 1
DOCUMENT REV.
A
12.97
12.97
32.03
25.00
10.00
5.00
R7.10
n14.40
50.00
74.73
DOWN 90.0° R7.10
300.93
DOWN 90.0° R7.10
74.73
15.00
25.00
25.00
n12.00
160.00
15.00
50.00
79.00
n2.40TYP.
TO BE MACHINED
160.00
4.00
A
B
C
D
E
F
1
2
3
4
5
6
7
8

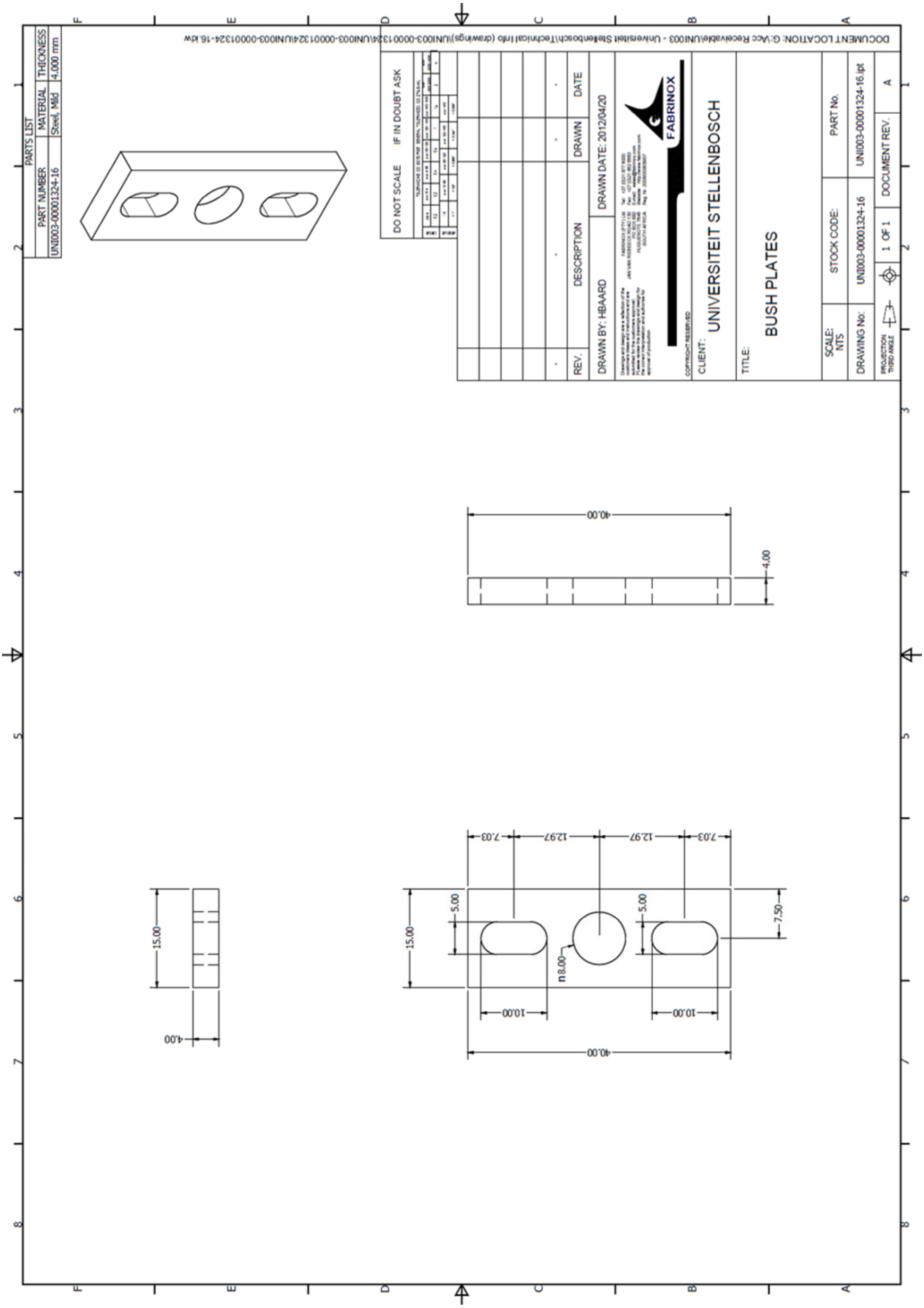
DOCUMENT LOCATION: G:\Acc Receivable\UNI003 - Universiteit Stellenbosch\Technical Info (drawings)\UNI003-00001324\UNI003-00001324\UNI003-00001324-16.idw
PARTS LIST
PART NUMBER
MATERIAL
THICKNESS
UNI003-00001324-16
Steel, Mild
4.000 mm
DO NOT SCALE
IF IN DOUBT ASK
REV.
DESCRIPTION
DRAWN
DATE
DRAWN BY: HBAARD
DRAWN DATE: 2012/04/20
FABRINOX
COPYRIGHT RESERVED
CLIENT:
UNIVERSITEIT STELLENBOSCH
TITLE:
BUSH PLATES
SCALE: NTS
STOCK CODE:
PART No.
DRAWING No:
UNI003-00001324-16
UNI003-00001324-16.ipt
DOCUMENT REV.
A
1 OF 1
PROJECTION THIRD ANGLE
40.00
4.00
7.03
12.97
12.97
7.03
5.00
5.00
7.50
15.00
15.00
n8.00
10.00
10.00
40.00
4.00
A
B
C
D
E
F
1
2
3
4
5
6
7
8

C. Electronic Circuits

C.1. Heliostat Local Controller Input Power Buffer, Voltage Monitoring and RS485 Transceiver

The circuit diagram for the LCU input power buffer-, voltage monitoring- RS485 transceiver is shown in Figure C.1. An academic licenced copy of Novarm Diptrace v2.3.0.3 was used to produce the diagram.

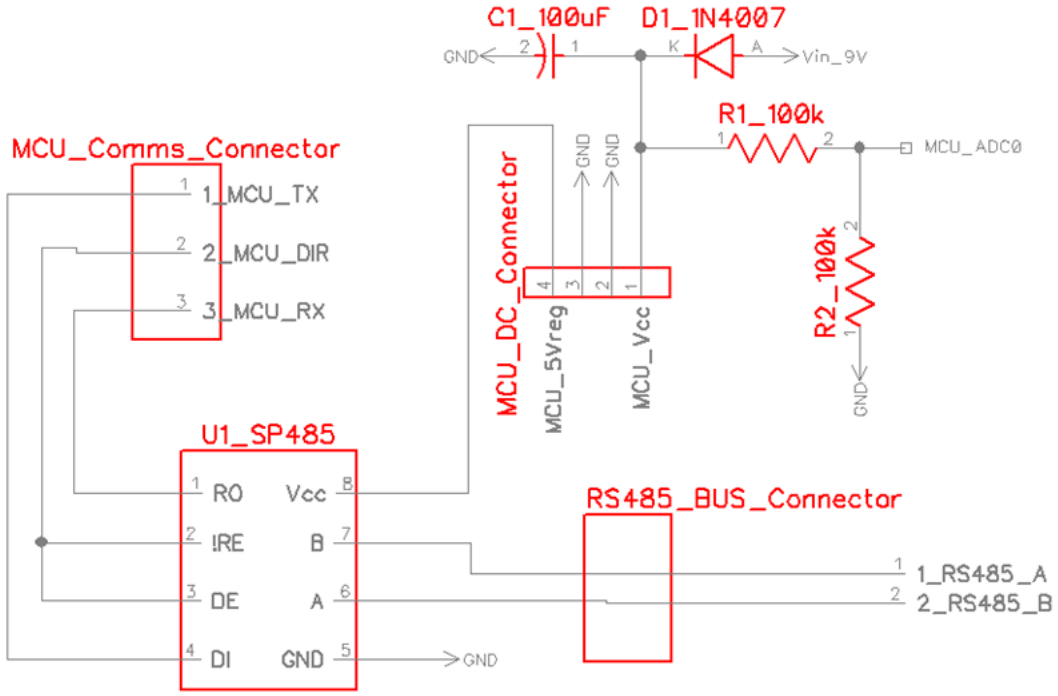

Figure C.1: Local controller unit power buffer and RS485 transceiver module

D. Communication Protocol

The following table lists the packet-based protocol used by the prototype system for all communication between the central system controller, cluster controllers and heliostat local controllers. The table is ordered according to message type using hexadecimal notation.

Table D.1: Prototype system communication protocol

Message Type number / name	**Description and comments.**
0x01 Query Stepcounts **0x02** Update Stepcounts	Q: D1[1] = LC_nr. D1[2-3]=Current Az-steps, D2[2-3]=Current El-steps. (use ADRfrom to know which LC stepcount must be updated in memory). U: D1[1]=LC_adr to updt, D1[2-3]=NewAz-steps, D2[2-3]=NewEl-steps
0x03 Q_Position1 **0x04** U_Position	1-2:N (2B), 3-4:E(2B), 5:Z(1B), [divide by 100] 6:LCindex(1B) 2^16=65536 → 0-655m N / E or 0 → 2.55m Z [2decimal precision]
0x09 Q_StatusFlags **0x10** U_StatusFlags	Q_ Health/status of Helio. Ask for STATUS FLAGS of last Movement test, last Accelerometer characterization readings, etc. (Results of movement test OR changes in acc-readings over time could raise flag at Terminal about mechanical structure, etc. (BUT, this would be detected from Calib adjustments also). U_ means RESET ALL FLAGS.
0x11 Q_GPStime (?Query or Offer?)	Query GPS Time from a particular CC (Periodically cycle through CCs to make sure GPS time OK at all CCs). Date: Date(3B), Time(3B). [Year since 2000 (1B), Month (1B), Day (1B), Hour(1B), Min(1B), Sec(1B)].
0x21 Q_Acc Proc. **0x22** S_Start_Acc_P	Start Accelerometer Procedure (characterization of Azim axis).

	When last has Acc Procedure been run? Send back timestamp.
0x23 Q_Move_diag **0x24** S_Move_diag	Q_ = Ask for timestamp of last movement diagnostic procedure. S_ = Command LC to do Movement diagnostic. (Does helio return to same azim / elev position after it's been moved around?)
0x55 GTx Solar Angles (CC to LC)	Data1 (3B): Solar Azim with 3dec precision. Data2 (3B): Solar Elev with 3dec precision.
0xA0 Set SysState=0	STOW. GPSLISTEN=0, Input A,B arrays.
0xA1 Set SysState=1	INIT / Approach Target. GPSLISTEN=0, TRACK = 0;
0xA2 Set SysState=2	IDLE. GPSLISTEN=1, TRACK=0;
0xA3 Set SysState=3	TRACK. GPSLISTEN=1, TRACK=1;
0xA8 RoughStep	Set mode to ROUGHSTEP
0xA9 FineStep	Set mode to FINESTEP
0xC0 Query Aim Position **0xC1** Update Aim Position (used for Intermittent repositioning to keep image on target throughout a day).	0:LCindex, 1-2: N(+-327.67) 3: E(+-1.27), 4-5: N(+-327.67) "LCindex" is index nr of LCs in CC. For example, if CC has 10 LCs: {0x01,0x02,0x03,0x04,0x05,0x06,0x11,0x12,013,0x14} then Index=0 refers to 0x01, index=8 refers to 0x13.
0xC2 Query RotMatrix_i	0: LCindex 1: Matrix parts. 0=RM1,RM2; 1=RM3,RM4; 2=RM5,RM6, 3=RM7,RM8, 4=RM9. 2-3: (0-2 value of matrix part) 4-5: (0-2 value of matrix part).
0xC3 Update RotMatrix_i	0: LCindex 1: Matrix parts. 0=RM1,RM2; 1=RM3,RM4; 2=RM5,RM6, 3=RM7,RM8, 4=RM9. 2-3: (0-2 value of matrix part) 4-5: (0-2 value of matrix part). EACH Matrix part has 01/32768*pi~<0.1mrad resolution, i.e MAX ERROR OF ~0.05mrad (max rounding error = half of resolution).

0xC4 Query Elev/Azim Bias	0: LCindex 1: 00 2-3: EL 4-5: AZ ([0..65536]-32768)/32768*pi which has <0.1mrad resolution
0xC5 Update Elev/Azim Bias	0: LCindex 1: Az/El (0=el, 1=az) 2-3: ([0..65536]-32768)/32768*pi which has <0.05mrad resolution
0xD0 Move UP/DOWN:	0: dir (0=Down, 1=UP), 1-2: count. 5:LCindex (LSB)
0xD1 Move E/W:	0: dir(0=West, 1=East) , 1-2: count. 5:LCindex (LSB).
0xD2 ZERO COUNTS	ZERO COUNTS: 0: dir, 1-2: count. 5: LCindex (LSB).
0xD3 STOW H_i	Stow Helio[i]
0xD4 LOCK POSITION	5: LCindex (LSB). Sets “LOCKNEXT” flag in LC. This causes next calculated value of HelioPOSITION to be stored (Stepcounts set to this)
0xD5 DEFOCUS LCi	5: LCindex (LSB) Commands LC to go to add OFFSET to Tower Pos vector
0xD6 REFOCUS LCi	5: LCindex (LSB) Commands LC to ZERO OFFSET of Tower Pos (return to actual target)
0xD7 LOCK AIM of LCi	5: LCindex (LSB) Commands LC to lock onto current position. It sets LOCKAIMFLAG=1 in LC(i).
0xD8 SEARCH for Target.	5: LCindex (LSB) Activates “Movement Detect” procedure in CC and starts “SEARCH” procedure in CC which adjusts LCi target vector until the camera detects movement.
0xD9 (from PC to CC)	STOW ALL (staggered in time). Commands ALL LC’s in cluster to defocus.

E. Software Flow Diagrams

Detailed flow diagrams of various software components of the prototype system are included here.

E.1. Cluster Controller Software Flow Diagram

The CCU acts as a communication hub between the central system controller and the heliostat local controllers. CCU software was written in the Wiring Language forms part of the Leaflabs Maple integrated development environment. Figure E.1 shows a detailed software flow diagram for it. The complete software code is contained in Appendix G.

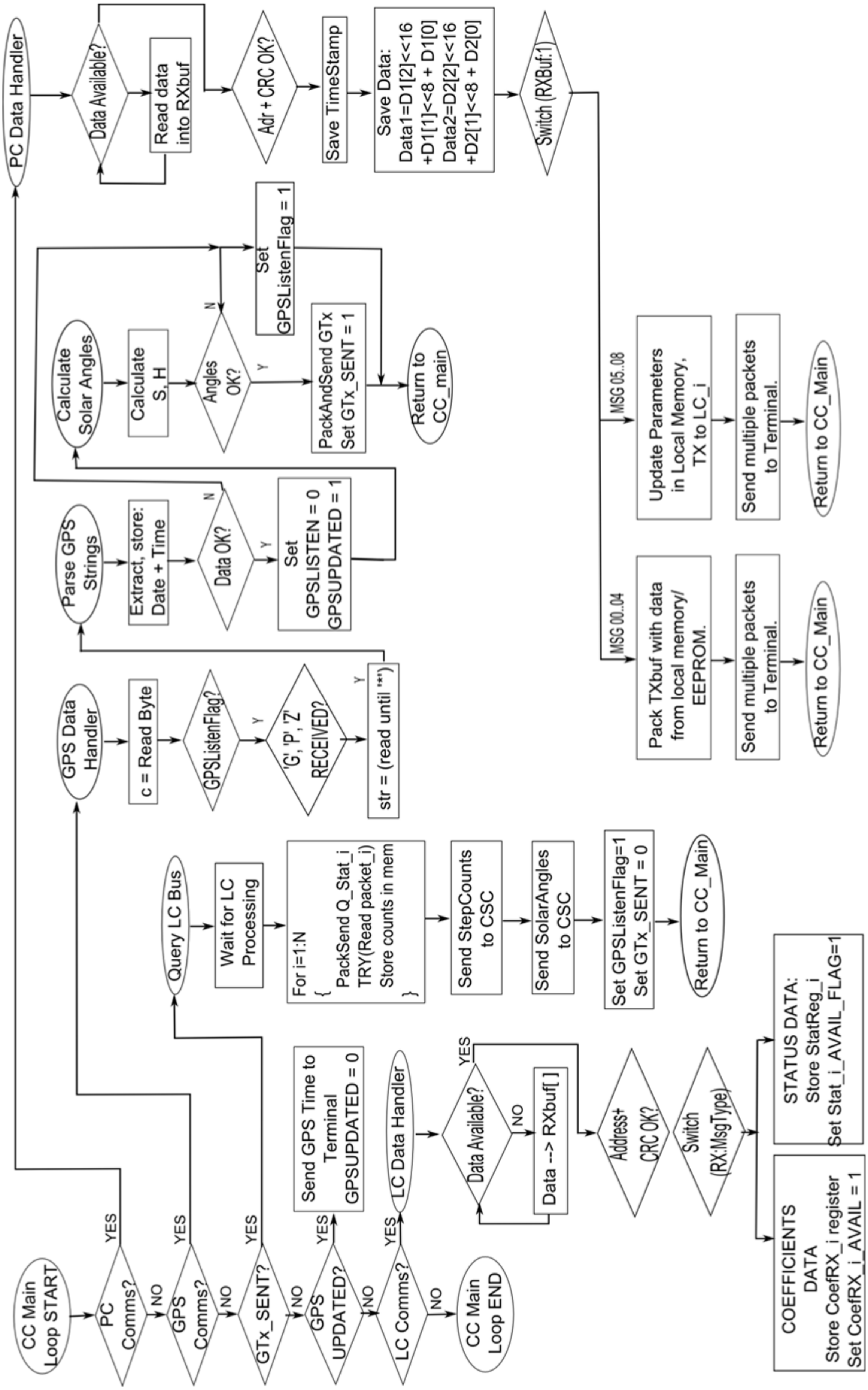

Figure E.1: Cluster controller software flow diagram.

E.2. Target Search Algorithm

The heliostats employed an outward spiral type search pattern when the calibration target could not be ‘found’ using normal open loop tracking. This typically occurred when a heliostat needed to be calibrated for the first time. Figure B.1 illustrates the target search algorithm. Block sizes (illustrated in the left part of Figure B.1) were set equal to half the calibration target side length to ensure sufficiently high resolution of the search grid.

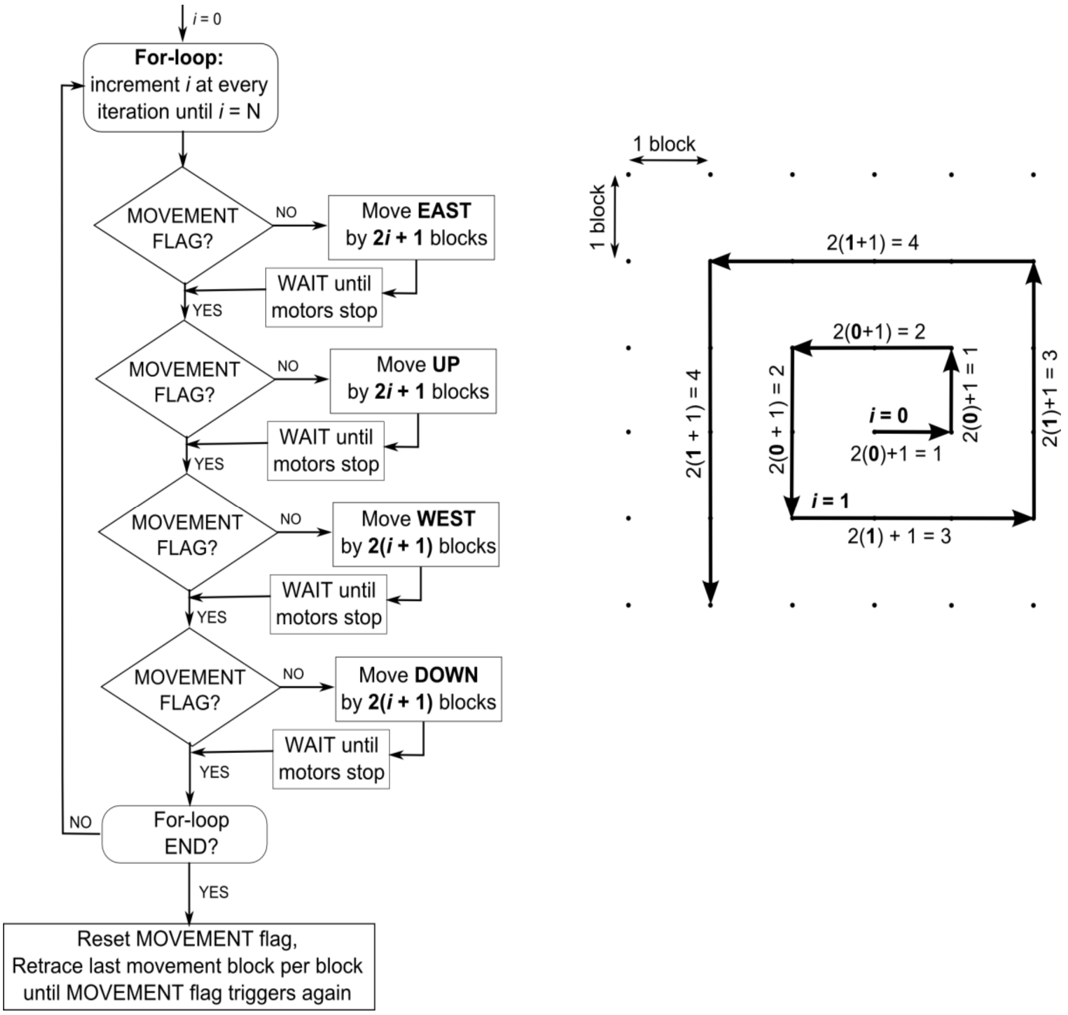

Figure E.2: Target search algorithm block diagram

E.3. Calibration Processing Flow Diagram

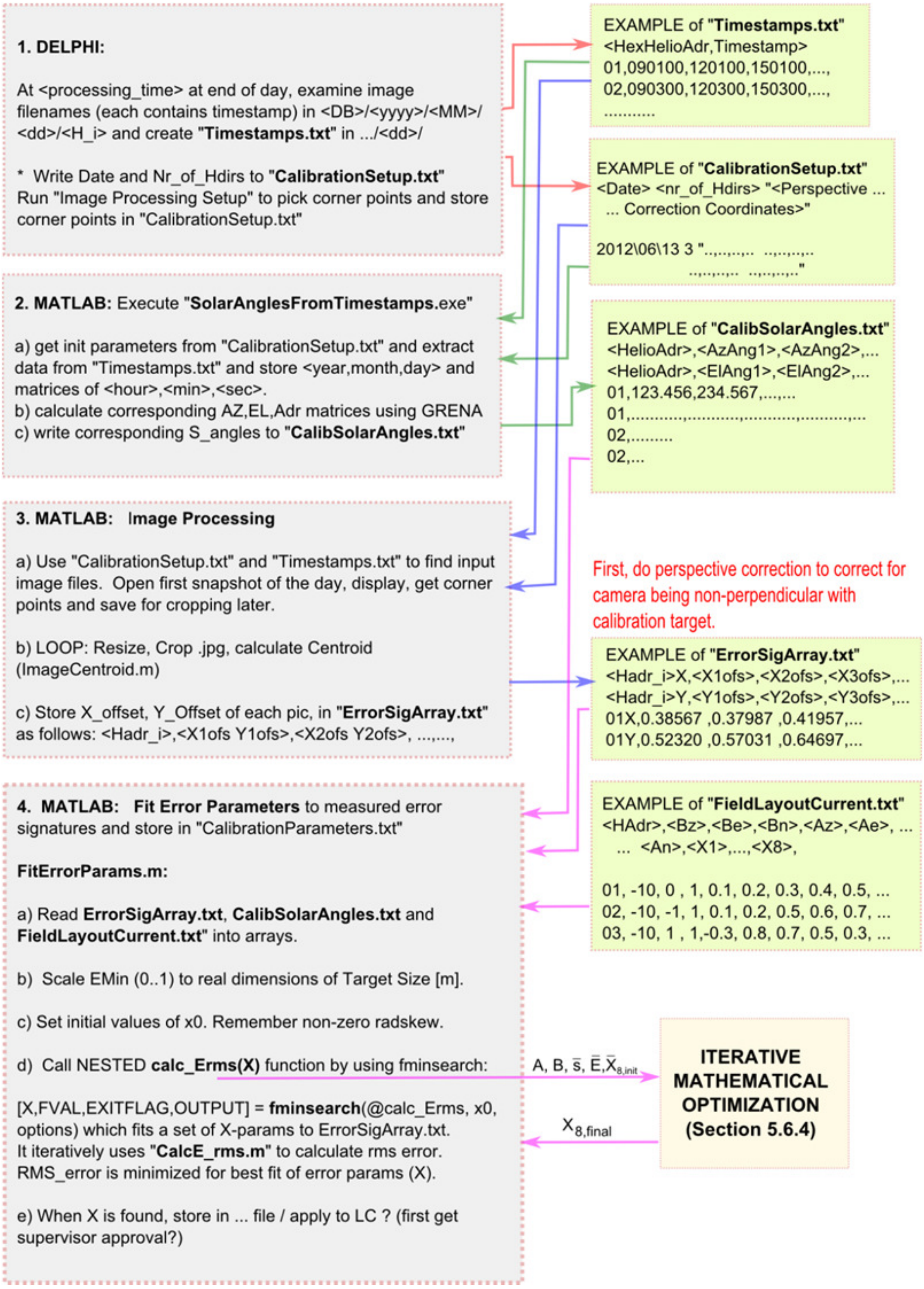

1. DELPHI:

At <processing_time> at end of day, examine image filenames (each contains timestamp) in <DB>/<yyyy>/<MM>/<dd>/<H_i> and create "**Timestamps.txt**" in .../<dd>/

* Write Date and Nr_of_Hdirs to "**CalibrationSetup.txt**" Run "Image Processing Setup" to pick corner points and store corner points in "CalibrationSetup.txt"

EXAMPLE of "**Timestamps.txt**"
<HexHelioAdr,Timestamp>
01,090100,120100,150100,...,
02,090300,120300,150300,...,
....

EXAMPLE of "**CalibrationSetup.txt**"
<Date> <nr_of_Hdirs> "<Perspective ...
... Correction Coordinates>"

2012\06\13 3 "..,..,..,.. ..,..,..,..
..,..,..,.. ..,..,..,.."

2. MATLAB: Execute "**SolarAnglesFromTimestamps**.exe"

a) get init parameters from "CalibrationSetup.txt" and extract data from "Timestamps.txt" and store <year,month,day> and matrices of <hour>,<min>,<sec>.
b) calculate corresponding AZ,EL,Adr matrices using GRENA
c) write corresponding S_angles to "**CalibSolarAngles.txt**"

EXAMPLE of "**CalibSolarAngles.txt**"
<HelioAdr>,<AzAng1>,<AzAng2>,...
<HelioAdr>,<ElAng1>,<ElAng2>,...
01,123.456,234.567,...,...
01,..........,..........,..........,..........,...
02,.........
02,...

3. MATLAB: Image Processing

a) Use "CalibrationSetup.txt" and "Timestamps.txt" to find input image files. Open first snapshot of the day, display, get corner points and save for cropping later.

b) LOOP: Resize, Crop .jpg, calculate Centroid (ImageCentroid.m)

c) Store X_offset, Y_Offset of each pic, in "**ErrorSigArray.txt**" as follows: <Hadr_i>,<X1ofs Y1ofs>,<X2ofs Y2ofs>, ...,...,

First, do perspective correction to correct for camera being non-perpendicular with calibration target.

EXAMPLE of "**ErrorSigArray.txt**"
<Hadr_i>X,<X1ofs>,<X2ofs>,<X3ofs>,...
<Hadr_i>Y,<Y1ofs>,<Y2ofs>,<Y3ofs>,...
01X,0.38567 ,0.37987 ,0.41957,...
01Y,0.52320 ,0.57031 ,0.64697,...

4. MATLAB: Fit Error Parameters to measured error signatures and store in "CalibrationParameters.txt"

FitErrorParams.m:

a) Read **ErrorSigArray.txt**, **CalibSolarAngles.txt** and **FieldLayoutCurrent.txt**" into arrays.

b) Scale EMin (0..1) to real dimensions of Target Size [m].

c) Set initial values of x0. Remember non-zero radskew.

d) Call NESTED **calc_Erms(X)** function by using fminsearch:

[X,FVAL,EXITFLAG,OUTPUT] = **fminsearch**(@calc_Erms, x0, options) which fits a set of X-params to ErrorSigArray.txt. It iteratively uses "**CalcE_rms.m**" to calculate rms error. RMS_error is minimized for best fit of error params (X).

e) When X is found, store in ... file / apply to LC ? (first get supervisor approval?)

EXAMPLE of "**FieldLayoutCurrent.txt**"
<HAdr>,<Bz>,<Be>,<Bn>,<Az>,<Ae>, ...
... <An>,<X1>,...,<X8>,

01, -10, 0 , 1, 0.1, 0.2, 0.3, 0.4, 0.5, ...
02, -10, -1, 1, 0.1, 0.2, 0.5, 0.6, 0.7, ...
03, -10, 1 , 1,-0.3, 0.8, 0.7, 0.5, 0.3, ...

Figure E.3: Detailed calibration processing flow diagram

F. Prototype system parts list and datasheet listing on CD

Table F.1: Prototype system parts list

Item	Manufacturer / Model nr.	Datasheet filename on CD
	LATEST HELIOSTAT MECHANISM	
Elevation axis motor	Wantai Motors / 57BYGH420	01_Stepper_57BYGH420.pdf
Azimuth axis motor	Wantai Motors / 42BYGHM809	02_Stepper_42BYGHM809.pdf
	HELIOSTAT LOCAL CONTROLLER UNIT	
Microcontroller	Arduino / Uno R3	03_Arduino_Uno.pdf
Stepper motor driver	Schmalz Haus LLC / Big Easy Driver	04_Stepper_Driver_BED.pdf
RS485 line transceiver	SGS Thompson / SP485ECP-L	05_RS485TRX_SP485.pdf
	CLUSTER CONTROLLER UNIT	
Microcontroller	Leaflabs / Maple Board r5	06_LeaflabsMaple_R5.pdf
GPS Receiver	uBlox / LEA-4P	07_GPS_uBlox_LEA-4P.pdf
RS485 line transceiver	Same as LCU	Same as LCU
	CALIBRATION TARGET CAMERA	
Network Camera	PLANET / ICA-HM126	08_Camera_Planet_ICA-HM126.pdf
Camera Lens	TMT / LZ05 [6 – 60 mm DC-auto iris vari-focal CS lens]	09_Camera_Lens_TMT-LZ05.pdf
Camera Enclosure	Ganz / Verso HSG 24V RAL9002	10_Camera_Enclosure_Ganz.pdf

G. CD Contents

Appendix G can be found on the included CD. It contains the following items:

1. The software code for the central system controller, including:
    a. The graphical user interface standalone executable application and the complete program code written in Borland Delphi.
    b. All Matlab procedures.

2. The complete software code for the cluster controller written in the Wiring Language for the Leaflabs Maple board.

3. The complete software code for the local controller written in the Wiring Language for Arduino.

4. The assembly instructions for the latest version of heliostat mechanism.

The folder structure is shown in Figure G.1.

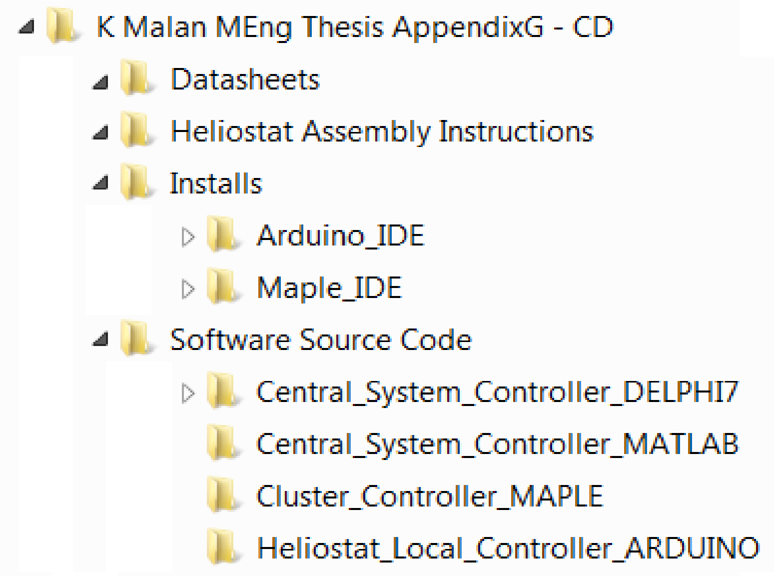

- K Malan MEng Thesis AppendixG - CD
    - Datasheets
    - Heliostat Assembly Instructions
    - Installs
        - Arduino_IDE
        - Maple_IDE
    - Software Source Code
        - Central_System_Controller_DELPHI7
        - Central_System_Controller_MATLAB
        - Cluster_Controller_MAPLE
        - Heliostat_Local_Controller_ARDUINO

Figure G.1: Folder structure of CD contents.

List of References

Abdulrahim, A., Diso, T., Oumarou, M. 2011. Development of a Solar Tracking Bi-focal Collector. *Continental Journal of Renewable Energy (2): 19 – 33, 2011. ISSN: 2251 – 0494.*

Acarnley, P. P. 2002. *Stepping Motors: A Guide to Theory and Practice, 4th ed.* The Institution of Engineering and Technology. London.

Alcauza, J. 2013. Spain Kills Feed-in Tariff for Renewable Energy. *CSP World.* [Online]. Available: http://www.csp-world.com/news/20130713/001121/spain-kills-feed-tariff-renewable-energy. [2013, October 25].

Aubrecht, J. 2005. Energy: Physical, Environmental and Social Impact, 3rd ed. Pearson. ISBN 978-0130932228.

Baheti, R. S., Scott, P. F. 1980. Design of Self-calibrating Controllers for Heliostats in a Solar Power Plant. *IEEE Transactions on Automatic Control, Vol. AC-25, #6, 1980-Dec.*

Berenguel, M., Rubio, F. R., Valverde, A., Lara, P. J., Arahal, M. R., Camacho, E. F., Lopez, M., 2004. An Artificial vision-based control system for automatic heliostat positioning offset correction in a central receiver solar power plant. *Solar Energy Vol 76 (2004), pp563-575.*

Betke, K., 2001. *The NMEA 0183 Protocol.* http://www.tronico.fi/OH6NT/docs/NMEA0183.pdf (retrieved 2011/10/17).

Blackmon, J. B., Caraway, M. J., Iwaki, A., I. 1986. *Solar One Beam Characterization System.* McDonnel Douglas Company / Sandia Contract 84-8173.

Blanc, P., Wald, L. 2011. A Library for Computing the Relative Position of the Sun and the Earth. Project ENDORSE.

Blanco-Muriel, M., Alarcon-Padilla, D., Lopez-Moratalla, T., Lara-Coira, M. 2000. *Computing the Solar Vector.* Solar Energy Vol. 70, No.5, pp431-444.

Bobinecz, M., 2012. Ivanpah Solar Electric Generating Facility: Engineering and Construction Contracting Conference. BrightSource Energy.

Brand, B., Stambouli, A. B., Zejli, D. 2012. The Value of Dispatchability of CSP Plants in the Electricity Systems of Morocco and Algeria. Energy Policy 47. (2012) 321-331.

Camacho, E. F., Berenguel, M., Alvarado, I., Limon, D. 2010. Control of Solar Power Systems: A Survey. *Proceedings of the 9th International Symposium on Dynamics and Control of Process Systems (DYCOPS) 2010.*

Camacho, E. F., Berenguel, M., Rubio, F. R., Martìnez, D. 2012. *Advances in Industrial Control: Control of Solar Energy Systems.* Springer.

Cebecauer, T., Skoczek, A., Betak, J., Suri, M. 2011. Site Assessment of Solar Resource: Upington Solar Park. Geomodel Solar s.r.o. Bratislava.

Clifford MJ, Eastwood D. *Design of a novel passive solar tracker*. Solar Energy 2004;77:269–80

Coalinga. [S.a.]. [Online]. Available: http://www.brightsourceenergy.com/coalinga. [2013, January 20].

Convery, M. 2010. System and Method for Aligning Heliostats of a Solar Power Tower. US Patent Application 2010/0252024 A1.

Convery, M. 2011. *Closed-loop Control for Power Tower Heliostats*. High and Low Concentrator Systems for Solar Electric Applications VI. Proceedings of SPIE, Volume 8108.

Cooper, P. I. 1969. The Absorption of Radiation in Solar Stills. *Solar Energy*, vol 12, pp. 333-346.

Crescent Dunes.[S.a.]. [Online]. Available: http://www.solarreserve.com/what-we-do/csp-projects/crescent-dunes/. [2013, November 10]

CSP World. [S.a.]. *South Africa has allocated 200 MW of CSP in third round of REIPPP*. [Online]. http://www.csp-world.com/news/20130620/001089/south-africa-allocated-200-mw-csp-third-round-reippp.dpuf. [2013, October 28].

Cyclades Corporation, 2004. *Cyclades-TS User Guide Version TS 1.4.0.*

De Rosa, A. V., 2005. *Fundamentals of renewable energy processes.* Academic Press, Inc., Stanford University.

Department of Trade and Industry of the Republic of South Africa. *Solar and Wind Sector Development Strategy: Solar Energy Technology Roadmap 18 June 2012.*

Duffie, J. A. & Beckman, W., A. 1980. Solar Engineering of Thermal Processes, First Edition. John Wiley and Sons.

Dyer, A. 2011. Ivanpah – A Case Study. Brightsource Energy. [Online]. Available:

Energy Information Administration (EIA). 2011. International Energy Outlook 2011.

Eriksson, F., 1998. Stepper Motor Basics. *Industrial Circuits Application Note.*

Fichtner GmbH. 2010. Assessment of Technology Options for Development of Concentrating Solar Power in South Africa for The World Bank. Johannesburg.

Freedman, D., Pisani, R., Purves, R. 2007. *Statistics, 4th ed.* W W Norton & Co. New York.

Gallego, B., Cohen, G., Mancini, T., Wilkins, T., Morse, F., Kearney, D. 2012. The History of American CSP: A Timeline. *CSP Today USA 2012 Conference & Exhibition*.

Gandolfo, G., Wendlandt, T. 2009. What is Stallguard™ and how to use it. *Trinamic Motion Control webinar.*

Gauché, P., Von Backström, T. W., Brent, A. C. 2013. A Concentrating Solar Power Value Proposition for South Africa. *Journal of Energy in Southern Africa vol.24 no.1* Cape Town.

Gauché, P., Von Backström, T. W., De Wet, A., Hlwempu, N. 2011. A Heliostat. South African Provisional Patent Application. Reference No. P2303ZA00/RvN.

Grena, R. 2007. *An Algorithm for the Computation of the Solar Position*. Solar Energy 82 462–470. ScienceDirect.

Ho, C. K., Ghanbari, C. M., Diver, R. B. 2011. Methodology to Assess Potential Glint and Glare Hazards from Conentrating Solar Power Plants: Analytical Models and Experimental Validation. *Journal of Solar Energy Engineering,* vol. 133 / 031021, pp. 1-9.

Horak, R., 2007. *Telecommunications and Data Communications Handbook.* Wiley and Sons. New Jersey.

How Trackers Work. [S.a.]. [Online]. Available: http://www.zomeworks.com/photovoltaic-tracking-racks/how-trackers-work/. [2012, July 29].

International Astronomical Union. [S.a.]. Standards of Fundamental Astronomy. [Online]. Available: http://maia.usno.navy.mil/NSFA/IAU2009_consts.html [2011, November 9).

International Energy Agency. 2010. Technology Roadmap: Concentrating Solar Power.

International Renewable Energy Agency. 2012. *Renewable Energy Technologies: Cost Analysis of Concentrating Solar Power.* IRENA Working Paper.

Jones, S., Kolb, G., Pacheco, J., Reilly, H. 1999. *Solar Two Central Receiver Consultancy Report.* California Energy Commission.

Jones, S., Stone, K. 1999. Analysis of Strategies to Improve Heliostat Tracking at Solar Two. SAND99-0092C.

Khalsa, S. S., Ho, C. K., Andraka, C. E. 2011. An Automated Method to Correct Heliostat Tracking Errors. In: *SolarPACES2011.* Granada.

Kolb, G. J., Jones, S. A., Donnelly, M. W., Gorman, D., Thomas, R., Davenport, R., Lumia, R. 2007. Heliostat Cost Reduction Study. Sandia National Laboratories, Albuquerque. [SAND2007-3293].

Kolb, G. J., Ho, C. K., Mancini, T. R., Gary, J. A. 2011. Power Tower Technology Roadmap and Cost Reduction Plan. Sandia National Laboratories. [SAND2011-2419].

Konstantin, P., Kretschmann, J. 2010. Assessment of Technology Options for Development of Concentrating Solar Power in South Africa for the World Bank. Fichtner GmbH & Co. – Presentation Slideshow. Johannesburg.

Kribus, A., Yogev, A., Sytnik, A. 2003. Continuous Tracking of Heliostats. International Solar Energy Conference Proceedings. ISEC2003-44018.

Kribus, A., Vishnevetsky, I., Yogev, A., Rubinov, T. 2004. Closed Loop Control of Heliostats. *Energy 29 (2004) 905–913.* Elsevier.

Kröger, D. 2012. Sunspot – the Stellenbosch University Solar Power Thermodynamic Cycle. Technical Report. Stellenbosch University.

Kubisch, S., Randt, M., Buck, R., Pfahl, A., Unterschütz, S. 2011. *Wireless Heliostat and Control System for Large Self-Powered Heliostat Fields.* SolarPACES 2011.

Kuphaldt, T. R. 2007. *Lessons in Electric Circuits, Volume IV – Digital, 4th ed.* Available: http://openbookproject.net/electricCircuits/. [2012, August 12].

Lamm, L. O. 1981. A New Analytic Expression for the Equation of Time. *Solar Energy,* vol. 26, pp. 465.

Landman, W. A. 2013. *Performance of the Reflective Surface Profile of a Heliostat.* Master's thesis, Mechanical Engineering, Stellenbosch University.

Lata, J., Alcalde, S., Fernandez, D., Lekube, X., Agarraberes, I., Martinez, E., Olano, J., Eguidazu, I. 2011. Commissioning and operation of commercial surrounding heliostat field for maximum but safe production. SolarPACES 2011.

Lee, C. Y., Chou, P. C., Chiang, C. M., Lin, C. F. 2009. Sun Tracking Systems: A Review*. Sensors. ISSN 1424-8220.*

Malan, K. J., Gauché, P. 2013a. A Support Structure for Multiple Heliostats. Patent Cooperation Treaty - International Patent Application no. PCT/2013/059931.

Malan, K. J., Gauché, P. 2013b. Model Based Open Loop Correction of Heliostat Tracking Errors. In: *SolarPACES 2013.* Las Vegas.

Mancini, T. R., Heller, P., Jones, S., Romero, M. 2000. *Catalog of Solar Heliostats.* SolarPACES Technical Report III – 1/00.

Maple, The. [S.a.]. [Online]. Available: http://leaflabs.com/devices/maple/. [2013, August 14].

Meeus, J. 1998. *Astronomical Algorithms, 2nd ed.* Willmann-Bell, Richmond.

Michalsky, J. J. 1988. The Astronomical Almanac's Algorithm for Approximate Solar Position (1950-2050). *Solar Energy,* vol. 40, no. 3, pp. 227-235.

Modbus.org. 2012. *MODBUS Application Protocol Specification v1.1b3.* http://www.modbus.org/docs/Modbus_Application_Protocol_V1_1b3.pdf. Accessed 15 March 2012.

Mousazadeh, H., Keyhani, A., Javadi, A., Mobli, H., Abrinia, K., Sharifi, A. A Review of Principle and Sun-tracking Methods for Maximizing Solar Systems Output. Renewable and Sustainable Energy Reviews 13 (2009) 1800-1818. Elsevier.

Murray, R., Li, Z., Sastry, S. 1994. *A Mathematical Introduction to Robotic Manipulation.* ISBN 978084937819. CRC Press.

National Energy Agency 2013. *The Fukushima Daiichi Nuclear Power Plant Accident: OECD/NEA Nuclear Safety Response and Lessons Learnt.* NEA #7161.

NREL. [S.a.]a. *Gemasolar Thermosolar Plant.* [Online]. Available: http://www.nrel.gov/csp/solarpaces/project_detail.cfm/projectID=62. [2013, October 29].

NREL. [S.a.]b. *Ivanpah Solar Electric Generating System.* [Online]. Available: http://www.nrel.gov/csp/solarpaces/project_detail.cfm/projectID=40. [2013, September 21].

Nutation. [S.a.]. [Online]. Available: http://nutation.org. [2013, October 23].

Ortega, J., Burgaleta, J., Téllez, F. 2008. Central Receiver System Solar Power Plant Using Molten Salt as Heat Transfer Fluid*. Journal of Solar Energy Engineering*, May 2008, Vol130 / 024501-1.

Palmer, M. 2011. *GE Invests in Integrated Solar Combined Cycle Technology.* Utilities-me.com. [Online]. www. Utilities-me.com/article-1357-ge-invests-in-integrated-solar-combined-cycle-tech/#.UpwSWeKNCRM. [2012, August 11].

Pardue, J. 2005. *C Programming for Microcontrollers*. Smiley Micros. Knoxville.

Peterka, J. A., Derickson, R. G., 1992. Wind load design methods for ground-based heliostats and parabolic dish collectors. Sandia National Laboratories. SAND92-7009.

Pfahl, A., Buck, R., Rehschuh, K. 2009. Method for controlling the alignment of a heliostat with respect to a receiver, heliostat device and solar power plant. US Patent Application 2009/0249787 A1.

Pitman, C. L., Vant-Hull, L. L. 1978. Errors in Locating the Sun and their Effect on Solar Intensity Predictions. In: *Meeting of the American Section of the International Solar Energy Society,* Denver, 28 Aug 1978, pp. 701-706.

Quero, J. M., Aracil, C., Franquelo, L. G., Ricart, J., Ortega P. R., Dominquez, M., Castaner, L. M., Osuna, R. 2007. Tracking Control System Using an Incident Radiation Angle Microsensor. *IEEE Transactions on Industrial Electronics. Vol. 54-2.* April 2007.

Rademaekers, K., Zaki, S. S., Smith, M. 2011. Sustainable Industry: Going for Growth & Resource Efficiency. European Commission of Enterprise and Industry.

Rao, S. S. 2009. *Engineering Optimization: Theory and Practice, 4th ed.* Wiley and Sons. New Jersey.

Reda, I., Andreas, A. 2008. Solar Position Algorithm for Solar Radiation Applications. NREL/TP-560-34302.

Reznik, D., Azarchs, A., Csaszar, A., Hartshorn, M. 2012. Calibration and tracking control of heliostats in a central tower receiver solar power plant. US Patent 8 192 027 B2.

Roos, T., Zwane, N., Kruger, E., Cathro, R., Perumal, S. 2007. A 25m^2 Target-aligned Heliostat with Closed-Loop Control. SES Solar World Congress 2007. Beijing, China. 18-21 September 2007, 8p.

Rubio, F., Ortega, M., Gordillo, F., Lopez-Martinez, M. 2007. Application of new control strategy for sun tracking.

Ruina, A., Pratrap, R., 2002. Introduction to Statics and Dynamics. Oxford University Press.

Sargent & Lundy LLC Consulting Group. 2003. Assessment of Parabolic Trough and Power Tower Solar Technology Cost and Performance Forecasts. NREL/SR-550-34440.

Schwarzbach, J., Kroyzer, G. 2010. *Heliostat Calibration.* US Patent Application Publication No: US 2010/0139644 A1.

Sherif, R. 2010. Concentrating Solar Power Technologies. In: *iNEMI Alternative Energy Workshop Proceedings*. San Jose, US. 20-21 October 2010.

Spencer, J. W. 1971. Fourier Series Representation of the Position of the Sun. *Search*, vol. 2, no. 5.

ST Microelectronics, 2011. RM0008 Reference Manual: STM32F101xx, STM32F102xx, STM32F103xx, STM32F105xx and STM32F107xx advanced ARM-based 32-bit MCUs.

Stine, W. B., Geyer, M. 2001. Power from the Sun. [Online]. Available: www.powerfromthesun.net. [2011, November 21]

Stone, K. W. 1986. Automatic Heliostat Track Alignment Method. US Patent 4,564,275. McDonnell Douglas Corporation.

Stone, K. W., Jones, S. A. 1999. *Analysis of Solar Two Heliostat Tracking Error Sources.* Sandia National Laboratories. SAND99-0239.

Stone, K. W., Kiefer, J. A. 1998. Open Loop Track Alignment Methodology. American Solar Energy Society Conference Proceedings. Albuquerque, New Mexico.

Stone, K. W., Lopez, C. W. 1995. Evaluation of the Solar One Track Alignment Methodology. *Solar Engineering*, vol. 1, pp. 521-526.

Stone, K. W., Sutherland, J. P. 1997. Solar Two Heliostat Tracking Performance. *Solar Engineering*: *Proceedings of the International Solar Energy Conference.* Washington, D.C.

Strachan, J. W. 1993. Revisiting the BCS, a Measurement System for Characterizing the Optics of Solar Collectors. Sandia National Laboratories. Albuquerque.

Swift, L. W. 1976. Algorithm for Solar Radiation on Mountain Slopes. *Water Resources Research,* vol. 12, pp. 108-112.

Treurnicht, J. 2013. Personal communication between Treurnicht, J. and Malan, K.

Truchero, A. F., Andreu, J., Garcia, J. B., 2010. *One Year Operation Experience on 143MW of Ground Mounted PV Systems.* 25th European Photovoltaic Solar Energy Conference. Valencia, Spain.

Tukiainen, M., 2013. Cape Town, South Africa – Sun Path Diagram. Gaisma [online]. Available: http://www.gaisma.com/en/location/cape-town.html [16 July 2013]

United States Department of Energy. 2011a. *DOE Pursues SunShot Initiative to Achieve Cost Competitive Solar Energy by 2020* [Online]. Available: http://www1.eere.energy.gov/solar/sunshot/news_detail.html?news_id=16701. [2011, December 15].

United States Department of Energy. 2012b. SunShot Initiative. *Heliostat System with Wireless Closed-loop* Control http://www.nrel.gov/docs/fy12osti/55464.pdf - retrieved 2012-10-20.

Van der Westhuizen, G. 2011. *Design, Implementation & Analysis of a Low-Cost, Portable, Medical Measurement System through Computer Vision.* Masters Thesis, Stellenbosch University.

Walraven, R. 1978. Calculating the Position of the Sun. *Solar Energy,* vol. 20, pp. 393-397.

Weisstein, E. W., 2013. *Circle-Circle Intersection.* Mathworld – A Wolfram Web Resource. http://mathworld.wolfram.com/Circle-CircleIntersection.html

Williams, R., N., 1993. A Painless Guide to CRC Error Detection Algorithms. Rocksoft™ Pty. Ltd.

Wimberley, J. 2011. *Power from the Midnight Sun.* [Online]. Available: http://www.samefacts.com/2011/09/health-and-medicine/medicare-health-and-medicine/power-from-the-midnight-sun/. [2012, August, 13].

WiringProject. [S.a.]. [Online]. Available: https://github.com/WiringProject/Wiring/. [2013, November 11].

Yogev, A., Krupin, V. 1999. Control of a Heliostat Field in a Solar Energy Plant. US Patent 5862799.

Zhang, Z. J., Pye, J. D., Ho, C. K. 2012. Estimation of Uncertainty in Automated Heliostat Alignement. Australian Solar Council – *Solar 2012 Conference Proceedings, 6-7 December 2012.* Melbourne.